ABSTRACT

Title of Thesis: An Experimental Investigation of a Micro Air Vehicle-Scale Cycloidal Rotor in Forward Flight

Tejaswi Jarugumilli, Master of Science, 2013

Thesis directed by: Professor Inderjit Chopra
Department of Aerospace Engineering

Micro air vehicles (MAVs) are small-scale, autonomous vehicles which are envisioned to perform a wide range of critical missions in the future. The relatively small size of MAVs presents a significantly different set of challenges from the point of view of aerodynamic, structural, and power/propulsion system design in comparison to full-scale aircraft. Therefore, scaling down conventional aircraft and helicopter designs may not necessarily yield an efficient MAV. The current research is focused on an unconventional concept, known as the cycloidal rotor, which has been proposed as an efficient, hover-capable solution at the MAV-scale.

The cycloidal rotor concept is nearly a century old, and its feasibility for unmanned/micro air vehicle applications was recently established. However, the availability of experimental data and analytical tools is scarce, especially in forward flight. There have not been many systematic experimental studies conducted in forward flight. Furthermore, developing analytical tools to predict forward flight performance can prove a difficult challenge at small scales, due to the limited un-

derstanding of low Reynolds number aerodynamics.

The objective of the current research, therefore, is two-fold: 1) to examine the forward flight capability of the cycloidal rotor concept, and 2) to develop a basic understanding of the operating principles in forward flight. Two distinct approaches were undertaken to fulfill this objective. First, systematic experimental studies were conducted in a wind tunnel to examine the time-averaged forces of the cyclorotor. The effects of blade pitching kinematics and rotor geometry on the time-averaged lift, propulsive force and power were examined at different forward speeds. Next, the results were interpolated to determine the trimmed, level flight performance requirements based on an existing twin-rotor cyclocopter MAV. The power consumption, lift-to-drag ratio and control input requirements of the cyclorotor were determined as a function of forward speed.

The second approach was to conduct flow field studies, which included 2-dimensional flow visualization and time-resolved, planar particle image velocmetry (PIV) measurements. The aim of the flow field studies was to develop an understanding of the flow physics behind force production of the cyclorotor. Both time-averaged and phase-averaged flow fields were examined. Time-averaged flow field measurements provided insights into the mean velocity distributions along the rotor azimuth. Phase-averaged flow field measurements provided insights into the role of unsteady aerodynamics, such as blade-vortex interactions, on the local force production of the blades. The flow field results were correlated to predictions from previous computational fluid dynamics (CFD) studies to help explain the distribution of forces along the rotor azimuth.

An Experimental Investigation of a Micro Air Vehicle-Scale Cycloidal Rotor in Forward Flight

by

Tejaswi Jarugumilli

Thesis submitted to the Faculty of the Graduate School of the
University of Maryland, College Park in partial fulfillment
of the requirements for the degree of
Master of Science
2013

Advisory Committee:
Professor Inderjit Chopra, Chair/Advisor
Dr. Moble Benedict, Research Scientist/Co-Advisor
Professor James Baeder
Professor Norman Wereley

Dedication

To my family

Acknowledgments

I want to begin by thanking my advisor, Dr. Inderjit Chopra. Over the past six years, Dr. Chopra has provided me with unwavering support and has created an atmosphere which any student or researcher would strive to work in. His efforts have had a tremendous impact on my academic career and outlook as a future aeronautical engineer. His drive for excellence and passion for engineering are reflective in his students, and I will always be grateful for the opportunities he has provided me at UMD.

My undergraduate and graduate experiences would not have been the same had I not met Dr. Moble Benedict. I first met Moble as a freshman undergraduate student. Since then, Moble has become my mentor and co-advisor, and working alongside him has been a gratifying experience. His innovative problem solving skills, resourcefulness and ability to constantly think outside-the-box have significantly shaped my thinking and perspectives on many things. I have yet to meet a more passionate and hardworking individual than Moble, and the skills and knowledge I have gained from working with him are sure to accompany me in whatever endeavor I may undertake in the future.

I would like to thank Dr. James Baeder and Dr. Norman Wereley for their valuable time and effort in serving on my thesis committee, and also for being great teachers in my courses. I am grateful to Professor Alan Winkelmann for allowing me to use the wind tunnel facility at UMD. Finally, I want to sincerely thank Dr. V.T. Nagaraj, one of the most knowledgeable individuals I have met, whose door has always been open for my questions and concerns.

I have to thank all of my friends, colleagues and professors at the Rotorcraft Center whom I had the pleasure to meet during these past few years. I want to particularly thank Andrew Lind for his help with the flow field studies in the current work, and for being a great friend. I want to also thank Dr. Vinod Lakshminarayan for his help with the CFD simulations in this work. It is difficult to list the names of all individuals I have encountered, but know that many of you have influenced my life in more ways than you know.

Many aspects of my graduate school would not have been possible without the incredibly efficient management of the Aerospace Administrative Office. I want to particularly thank Otto Fandino, LaVita Williams, Laura Thorsen, Kevin Lewy, Tom Hurst, Erika Aparaka, Debora Chandler and Becky Sarni for all their hard work. I want to also extend my thanks to Howie Grossenbacher and Mike Perna from the Aerospace Machine Shop, both of whom have made numerous parts which have been elemental to this research.

I owe my deepest gratitude to my family – my mother and my sister. Their enduring support, encouragement and guidance have been the source of all my accomplishments, and helped me through the smooth and turbulent periods of my life. I will forever be indebted to them for the opportunities they have afforded me towards pursuing my own dreams.

This research would not have been possible without the support of the U.S. Army's Micro Autonomous Systems and Technology – Collaborative Technology Alliance (MAST-CTA) program.

Table of Contents

List of Tables

List of Figures

List of Abbreviations

b	blade span
c	blade chord length
R	rotor radius
N_b	number of blades
U_∞	freestream velocity
u	horizontal component of velocity
v	vertical component of velocity
X, Y, Z	rotor coordinate system
α	angle of attack
α_i	virtual incidence angle
θ	blade pitch angle
θ_A	amplitude of blade pitch
θ_M	mean pitch amplitude
μ	advance ratio, $U_\infty/\Omega R$
σ	rotor solidity
ϕ	phasing of blade pitch
Ω	rotational speed of the rotor
ψ	azimuthal position of blade

CFD	Computational Fluid Dynamics
DAQ	Data Acquisition
DARPA	Defense Advanced Research Projects Agency
MAV	Micro Air Vehicle
PIV	Particle Image Velocimetry

Chapter 1: Introduction and Literature Review

1.1 Micro Air Vehicles

A micro air vehicle (MAV) is characterized as a small-scale, autonomous flying vehicle. The emergence of the micro air vehicle can be traced back to the early 1990s, and can be seen as a culmination of: 1) an increasing need for smaller unmanned aerial vehicles (UAVs) and 2) advancements in miniaturized electrical and mechanical systems. Some of the key attributes of MAVs include portability, rapid deployment, low radar cross-section, low noise and low production cost. These characteristics can enable MAVs to conduct a variety of missions in a more cost-effective and low-risk manner in comparison to UAVs and full-scale aircraft. Some potential MAV missions include surveillance and reconnaissance in the battlefield, biochemical sensing, fire and rescue operations, border surveillance and traffic monitoring.

In the United States, a key organization responsible for fostering a sustained research and development effort in MAVs was the Defense Advanced Research Projects Agency (DARPA). After several feasibility studies between 1991 and 1996, DARPA set forth several design objectives for MAVs in 1997 [1]. The performance goals for the target MAV were set based on an "over-the-hill" reconnaissance mission and included an endurance of up to 60 min, a range of 10 km and a maximum speed be-

tween 10 to 20 m/s. The target MAV was a vehicle with a maximum characteristic length of 15.24 cm (6 in) and a mass of less than 100 g, with a payload capacity of 20 g [2]. In the following decade, numerous universities and companies have produced a wide range of MAV designs aimed to meet DARPA's design objectives [3]. Over the years, the term 'MAV' has broadened to include vehicles with dimensions in the range of 15 cm to 1 m and a mass between 20 g to 1000 g [3], although the target MAV set by DARPA is still being pursued today.

1.2 Technical Challenges

The drive to maximize performance and minimize the size of MAVs presents a unique set of challenges in regard to the aerodynamic, structural and propulsion aspects of design [5]. As indicated in Fig. 1.1, MAVs fall in an operating range with at least an order of magnitude smaller in length and two orders of magnitude lighter in weight compared to full-scale aircraft [3]. At these small scales, the governing aerodynamics is significantly different than at larger scales. One way to quantify these scaling effects is to consider a non-dimensional parameter called the Reynolds number (Re), which is proportional to the product of the size and velocity of the object that is moving relative to the fluid:

$$Re = \frac{\rho v l}{\mu} \tag{1.1}$$

The Reynolds number is effectively a ratio of the inertial force to the viscous force in the flow. In regard to the airfoil section of any lifting surface (i.e. wing or

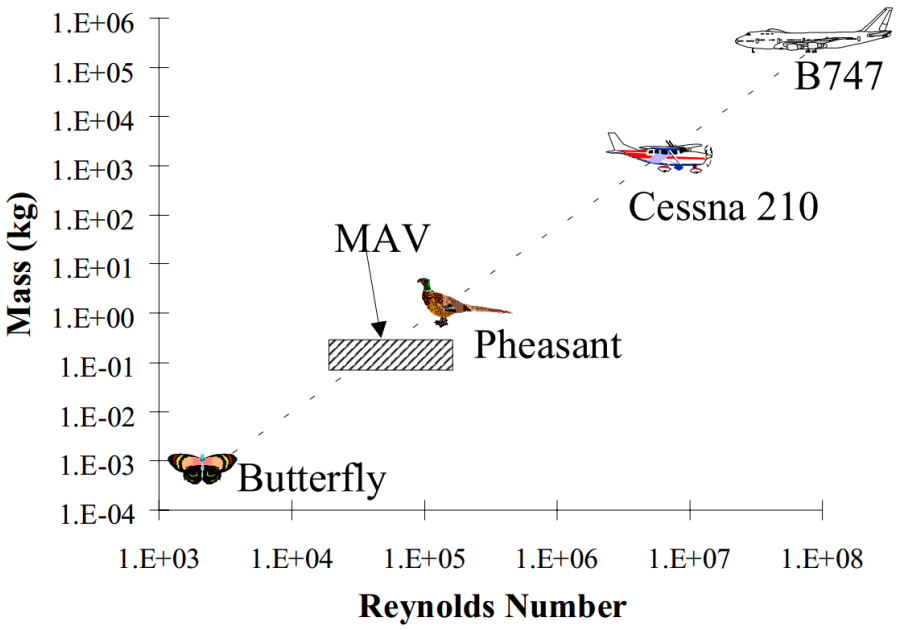

Figure 1.1: Reynolds number range for flight vehicles [4].

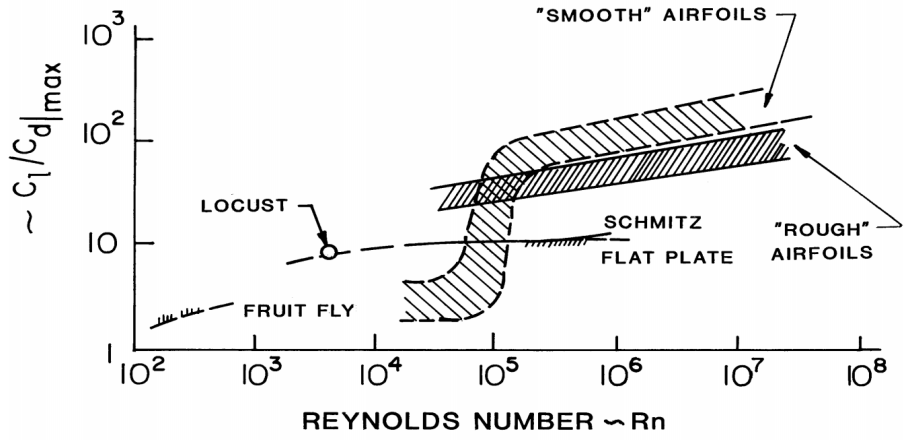

Figure 1.2: Airfoil maximum lift-to-drag ratio versus Reynolds number [6].

rotor), transition and separation of the flow plays a critical role in the development of the boundary layer, which in turn, affects the aerodynamic performance of the airfoil [4]. Furthermore, transition and separation are a strong function of the Reynolds number.

At high Reynolds numbers (Re$> 10^6$), inertial forces are dominant and the flow is generally characterized by turbulent boundary layers, and the laminar and transitional regions have relatively little effect on the forces exerted on the lifting surface. Airfoil performance at high Reynolds numbers is generally high, and the maximum lift-to-drag ratios achieved are generally greater than 10 (Fig. 1.2). At low Reynolds numbers (Re$< 10^5$), however, viscous forces are dominant and the flow is mostly characterized by laminar flow. There is a decreased ability of the fluid to withstand adverse pressure gradients, and it can therefore separate more easily from the surface of the airfoil. Thus, the transition from laminar to turbulent flow is difficult to achieve. Flow separation and reattachment can occur within a very small distance along the chord-line of the airfoil, leading to the formation of a laminar separation bubble (LSB), which decreases the lifting capability of the airfoil and increases the drag [7]. The maximum lift-to-drag ratios of airfoils degrade at lower Reynolds numbers, as indicated in Fig. 1.2. Although certain airfoil shapes (e.g. thin/flat-plate and insect wing-based airfoils) can lead to improved aerodynamic performance at low Reynolds numbers, the resulting lift-to-drag ratios are still substantially lower compared to airfoils at higher Reynolds numbers.

MAVs typically operate in the chord Reynolds number range of 30,000 to 100,000 and therefore are affected by the unfavorable aerodynamic characteristics

discussed above. Furthermore, low Reynolds number aerodynamics is a relatively new area of research primarily spurred by interest in MAVs [7]. An understanding of the fundamental flow physics in this sensitive Reynolds number regime is far from complete, and the limited experimental data and analytical tools available to accurately model the aerodynamic environment presents a difficult challenge for the MAV designer.

In addition to the aerodynamic challenges, MAVs pose a unique set of structural and propulsion design challenges. The drive to make MAVs smaller, lighter and with longer endurance places significant design constraints on power storage, propulsion system design and efficient structural design. The efficiency of a power/propulsion system degrades with decreasing size, and a typical MAV power plant system comprises of approximately 60% of the gross take-off weight (GTOW) [3]. Further technological advances in batteries and electric motors, and perhaps in alternative forms such as micro fuel cells and micro-engines [8], are needed before systems of higher power-to-weight ratios can be realized. Another key factor that leads to high empty weight fractions in MAVs is the structure itself. Advances in lightweight, flexible and adaptive wing structures that can offer high strength-to-weight ratios are needed to increase the structural efficiency of a MAV system.

1.3 Existing Micro Air Vehicles

Over the past decade, numerous MAVs have been successfully developed and flight tested. Several of the MAVs are presented in Fig. 1.3 in terms of their mass and

endurance characteristics. The MAVs generally fall into three categories which include: 1) fixed-wing, 2) rotary-wing and 3) bio-inspired or bio-mimetic platforms. The current section provides a brief discussion of each category.

1.3.1 Fixed-Wing Micro Air Vehicle Platforms

Of the existing MAVs, fixed-wing MAVs are the most technologically mature. They offer the best relative performance in terms of empty weight, payload and endurance characteristics [3]. One particular example is the AeroVironment Wasp III, which has a mass of approximately 430 g and an endurance of up to 45 min [9].

Fixed-wing MAVs are often designed to conduct missions that require long range and endurance, and high cruise speeds. They are less mechanically complex compared to rotary-wing and flapping-wing configurations, as they use separate systems for generating lift, propulsive and control forces. However, conventional fixed-wing MAVs rely on relatively high forward speeds to generate lift. Therefore, a significant disadvantage of fixed-wing MAVs is their inability to hover or fly at low speeds, preventing operations in indoor and highly confined urban environments.

1.3.2 Rotary-Wing Micro Air Vehicles

Unlike fixed-wing MAVs, rotary-wing MAVs offer the ability to hover and fly at extremely low-speeds. Over the past few years, several rotary-wing MAVs have been developed, some of which are shown in Fig. 1.3. One particular example is the PD-100 Black Hornet MAV, which has a mass of 16 g and a forward flight endurance

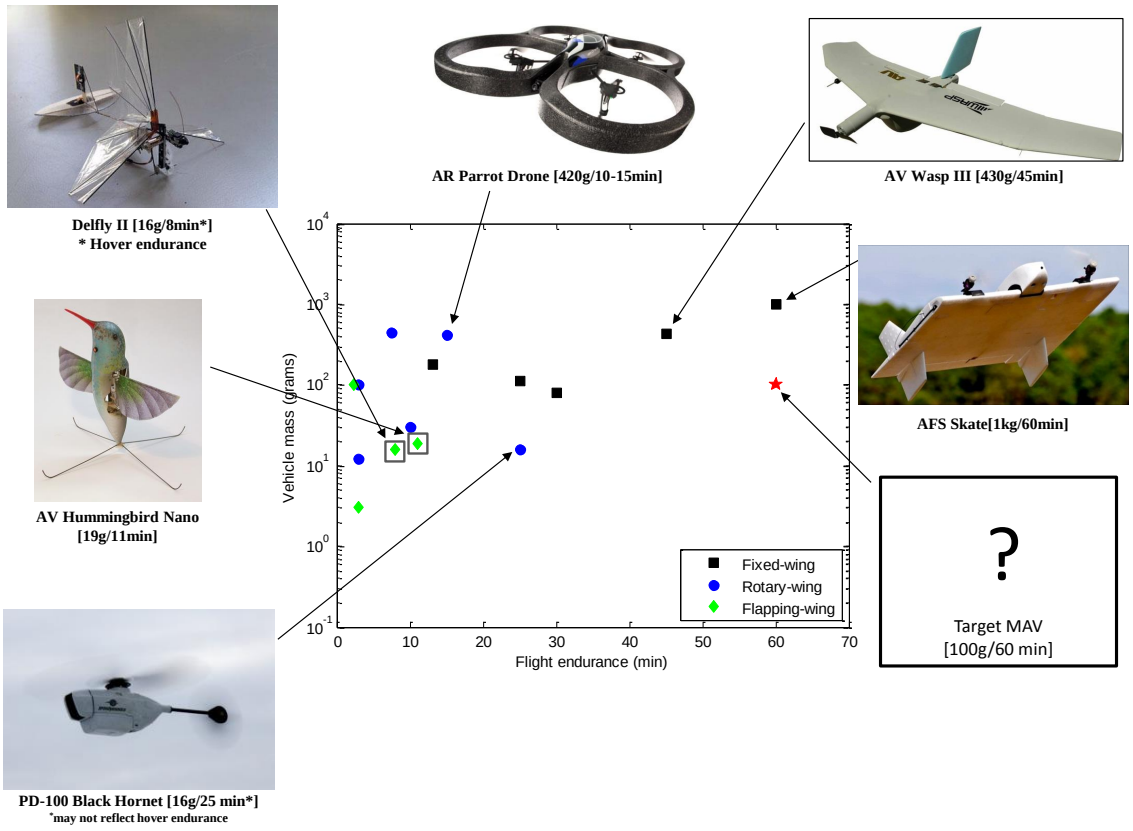

Figure 1.3: Weight and endurance characteristics of several fixed-wing, rotary-wing and flapping-wing MAVs developed over the past decade.

Figure 1.4: Proxdynamics PD-100 Black Hornet MAV [10].

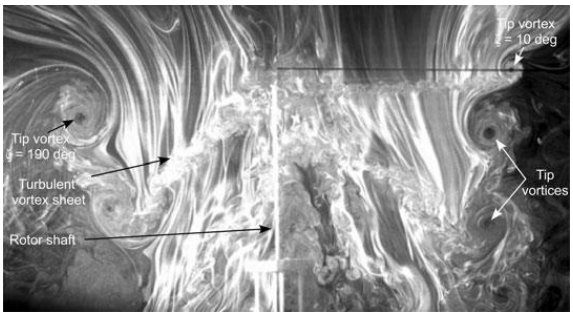

Figure 1.5: Flow visualization image of a micro-rotor [12].

up to 25 min [10]. Overall the mass and endurance characteristics of rotary-wing MAVs are relatively lower than those of fixed-wing MAVs, as shown in Fig. 1.3.

Currently, the prevailing choice for hover-capable platforms is the conventional edgewise rotor [3, 5]. However, conventional rotors are known to experience degraded aerodynamic efficiencies at low Reynolds numbers (10,000 to 50,000) [11, 12]. The degraded aerodynamic performance can be attributed to the large values of profile drag associated with thick boundary layer formations on the blades, the relatively large induced losses, as well higher rotational and turbulent losses in the wakes downstream of the rotating blades [12]. A flow visualization image showing the highly turbulent wake of a micro-rotor is presented in Fig. 1.5. The maximum figure of merit (FM) achieved for a conventional MAV rotor is approximately 0.65 [5]. In comparison, efficient full-scale rotors can achieve FM values in the range of 0.75 to 0.82 [11].

1.3.3 Biologically-Inspired Micro Air Vehicles

In light of the technical challenged faced at low Reynolds numbers, scaling down conventional fixed-wing and rotary-wing designs may not be the best approach toward developing an efficient micro air vehicle. Alternative solutions or 'out-of-the-box' solutions must be sought. One such alternative solution is the flapping-wing based MAV. Currently, flapping-wing MAVs fall into two sub-categories, which include avian-based (or bird-like) and insect-based platforms. The operational kinematics of the two platforms is fundamentally different, and aims to serve different purposes. Avian-based wings operate primarily in the vertical plane, and can offer efficient flight at high speeds (similar to fixed-wing MAVs). In contrast, insect-based wings operate in the horizontal plane, and utilize a reciprocating wing motion, which features both translation and rotational motion [13]. The most significant difference between avian-based and insect-based flapping is the ability to hover. Most insects are capable of hovering, whereas this capability is restricted to only a few specifies of birds (e.g. hummingbird).

There have been very few successful developments of flapping-wing MAVs over the past decade, especially hover-capable flapping wing MAVs. The most recent example of a successful development is the AeroVironment Hummingbird Nano (Fig. 1.6) [16]. The key technical challenges associated with developing efficient flapping-wing MAVs include both aerodynamic and structural aspects. Insect-wing based MAVs have gained a considerable amount of attention in recent years, particularly due to their potential to generate high levels of lift through unsteady

Figure 1.6: Aerovironment Hummingbird Nano [16].

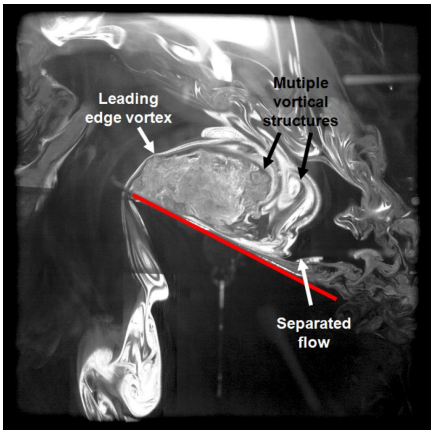

Figure 1.7: 2-D flow visualization image of a flapping-wing [15].

aerodynamic mechanisms [13, 14–15]. For example, the improved aerodynamic performance of insects is attributed in part to the generation and maintenance of a stable region of vorticity known as the leading edge vortex [14]. A 2-D experimental flow visualization image showing the development of a LEV on a flapping-wing is presented in Fig. 1.7. A key challenge in flapping-wing based MAV is developing a mechanism to emulate the complex kinematics of the wings of insects and birds. Furthermore, the lack of analytical tools to accurately predict the unsteady aerodynamics makes the challenge even more difficult. Thus, flapping-wing MAVs are still far from competing with existing fixed-wing and rotary-wing configurations at present.

1.4 Cycloidal Rotor Concept

The current research is focused on another alternative hover-capable concept, known as the cycloidal rotor. The cycloidal rotor (or cyclorotor) is a rotary-wing concept

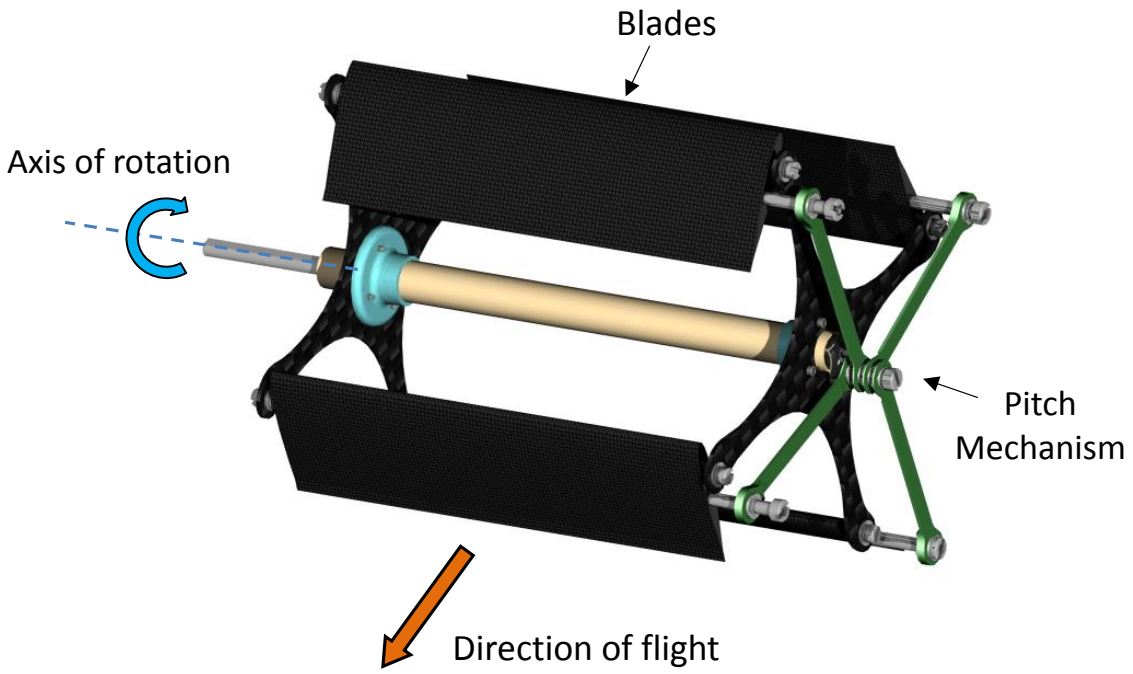

Figure 1.8: Cycloidal rotor concept.

recently proposed as an efficient alternative to the conventional rotor at MAV scales. The cyclorotor (Fig. 1.8) consists of a set of blades that follow a circular trajectory about a horizontal axis of rotation, with the blade span parallel to this axis and perpendicular to the direction of flight. As each blade translates along the circular path, a passive pitching mechanism cyclically allows the blade pitch angle to vary harmonically along the circular trajectory. These pitching kinematics allow the cyclorotor to produce a net non-zero aerodynamic force. The magnitude and direction of the net force vector can be controlled by varying the amplitude and phasing of the blade pitching kinematics.

The key advantages of utilizing a cyclorotor system are its higher aerodynamic efficiency and potential for low noise and increased maneuverability. Unlike a conventional edgewise rotor, where aerodynamic conditions vary significantly along the blade span, all span-wise blade elements of a cyclorotor operate under similar aerodynamic conditions (i.e. flow velocities, Reynolds numbers, and angles of incidence), which can allow every section of the cyclorotor blades to operate at maximum aerodynamic efficiency. Previous studies have shown that a cyclorotor can achieve higher values of power loading (thrust/power) compared to a conventional rotor of the same scale [17]. Furthermore, the relatively uniform span-wise distributions of aerodynamic forces can allow the cyclorotor to operate at a lower tip speed compared to a conventional rotor for a given thrust value, potentially leading to reduced noise signature. A third advantage of the cyclorotor is its unique thrust vectoring capability. The resultant force vector of the rotor can be instantaneously set to any direction perpendicular to the axis of rotation, providing full 360° control authority. Thus, a cyclorotor-based (cyclocopter) MAV may provide relatively better maneuverability compared to a conventional rotor-based MAV, making it ideal for operations in highly confined and gusty environments.

1.5 Previous Work on Cycloidal Rotors

The cyclorotor concept has been explored for aviation applications since the early 20th century. However, many early cyclorotor developments were not well documented, and there has been significant amount of discontinuity in research over the

years [20]. The current section aims to outline the progress of cyclorotor research from the early 1900s to the present.

1.5.1 Early Developments (1909–1948)

The earliest known cyclorotor developments are claimed to have occurred between the years 1909-1914 [18, 19]. E.P. Sverchkov, a military engineer from St. Petersburg, Russia, developed an aircraft called "Samoliot" (or "wheel ornithopter") circa 1909. The aircraft, shown in Fig. 1.9a, is said to have an empty weight of 200 kg and was unsuccessfully tested. Although this concept had the characteristics of the modern cyclogyro, its operating principles could not be verified precisely. Another early development occurred between 1909-1914, when an unknown French cyclogyro aircraft was built and tested (Fig. 1.9b) [19]. Apart from a few movie clips showing the destructive failure of the rotors in tethered flight tests, there is a lack of supporting documents about the aircraft. Based on Fig. 1.9b , the vehicle appears to

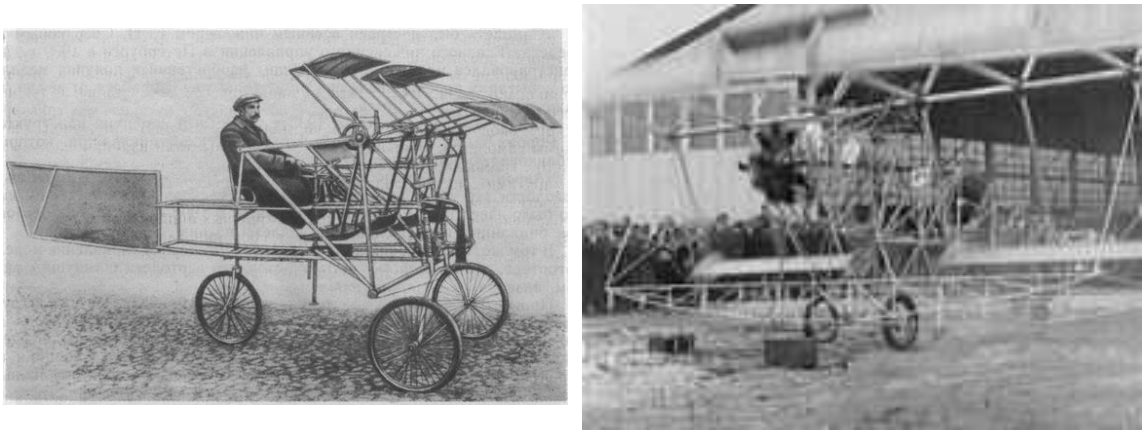

(a) Samoliot cartoon rendering.

(b) An unknown French cyclocopter.

Figure 1.9: Early developments of the cyclogyro (1909-1914) [18], [19].

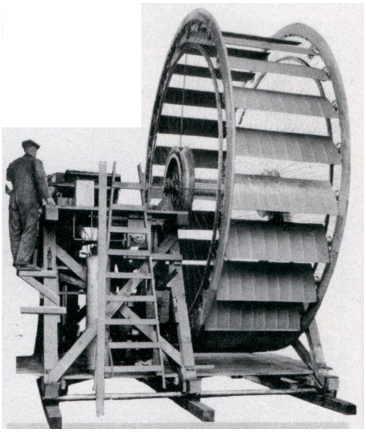

(a) Kirsten-Boeing propeller experimental setup.

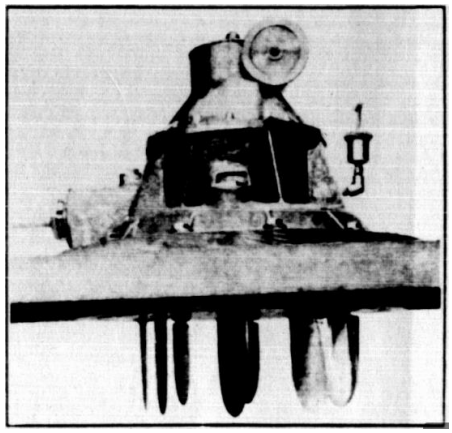

(b) Kirsten underwater propeller.

Figure 1.10: Cycloidal propellers developed by Kirsten [22].

have two main cyclorotors and a single tail cyclorotor.

Beginning in the mid-1920s, there was increased interest in the cyclorotor concept and several systematic studies began to take shape [21–29]. One of the pioneering researchers in cyclogyro technology was Frederick Kurt Kirsten, a Professor at the University of Washington (Seattle). Over a span of nearly 20 years, Kirsten pursued a sustained research effort of the cycloidal propeller for both aviation and marine applications. Kirsten collaborated with airplane manufacturer William E. Boeing, and together they started the "Kirsten Boeing Engineering Company" [31]. With the aid of Boeing, Kirsten successfully carried out numerous experiments on cycloidal propellers and eventually developed the "Kirsten-Boeing propeller" [22]. The propeller, shown on a test stand in Fig. 1.10a, had a diameter of 4.6 m and consisted of 24 blades; each blade had a span of 1.45 m and a chord length of 0.56 m. The propeller was tested up to a rotational speed of 225 rpm and produced a thrust of about 212 lbs.

Following these experiments, larger versions of the Kirsten-Boeing propeller were designed and planned to be installed on an airship. Kirsten believed the thrust-vectoring capability of the cycloidal rotor would provide a great advantage over the conventional screw propeller for airships. The cycloidal propeller could produce great "rudder-forces," and thus airship control would be independent of flight speed. Six large-scale cycloidal propellers were designed for the USS Shenandoah airship, with each propeller capable of producing 1800 lbs of thrust. However, before the Kirsten-Boeing propellers could be installed and tested, the Shenandoah crashed in 1925 [22]. This incident was a major setback for the development of the Kirsten-Boeing propeller, and the Kirsten-Boeing Engineering Company eventually failed.

In addition to aviation applications, Kirsten envisioned the cycloidal rotor for marine applications. The thrust-vectoring capability of the cycloidal rotor could provide the necessary propulsion and control forces for a boat, thereby eliminating the need for a rudder and providing increased maneuverability compared to a conventional screw propeller. In the 1930s, Kirsten modified his propeller design for underwater use, with new design constraints to keep water away from the driving mechanisms (Fig. 1.10). The experimental propeller was successfully tested on a boat, which covered a distance of about 4000 nautical miles and demonstrated its practical utility [22]. In 1931, another cycloidal rotor-based propeller was proposed by Austrian inventor Ernst Schneider [24, 25], and the propeller eventually came to be known as the "Voith-Schneider propeller (VSP)." A modern version of the VSP is shown in Fig. 1.11, and it remains the only successful commercial application of a cycloidal rotor to this day.

(a) Voith-Schneider propeller (VSP).

(b) Two VSPs installed on a ship.

Figure 1.11: Voith-Schneider propeller [23].

In July 1933, Swedish-French engineer Strandgren published the first theoretical study of a cycloidal rotor titled "The Theory of the Strandgren Cyclogyro" [26]. The publication included a very simplified quasi-steady aerodynamic analysis of a cyclogyro to help explain how lift and propulsion are achieved. The instantaneous blade forces were calculated in the directions normal and tangential to the blade trajectory, and then resolved to obtain the force components perpendicular and parallel to the freestream velocity. The forces of each blade were averaged over a complete revolution, and multiplied by the number of blades to obtain the net thrust and torque of the rotor. The induced velocity was calculated using the rotor projected area. Furthermore, the study attempted to establish the feasibility of the cyclogyro for aircraft use. It showed the potential for autorotation during the event of a power failure, and also the ability to control the magnitude and direction of thrust using the blade pitching kinematics, namely the pitch amplitude and phasing.

Following Strandgrens publication, John B. Wheatley at the National Advi-

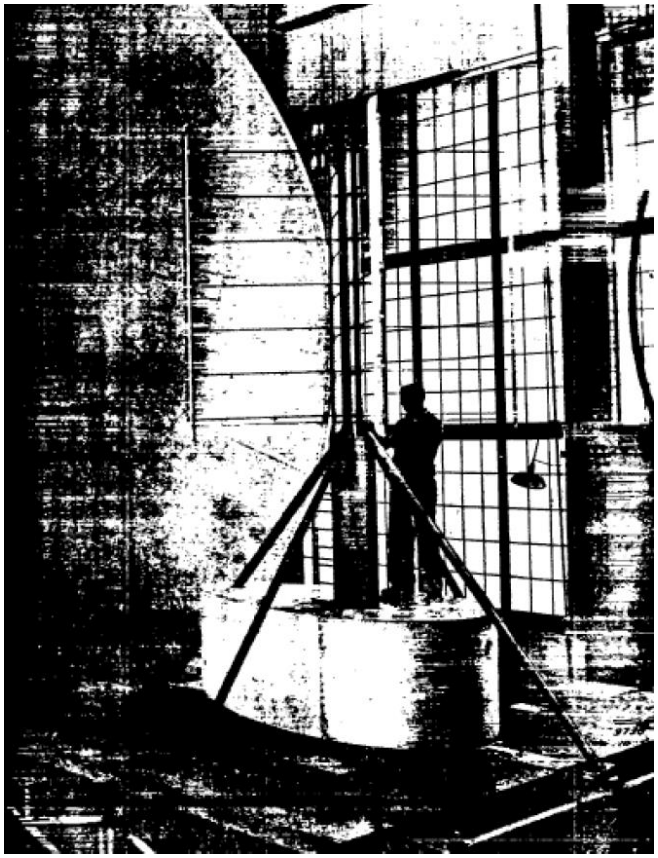

Figure 1.12: Wheatley's wind tunnel setup [28].

sory Committee for Aeronautics (NACA) published a simplified aerodynamic theory for the cyclogiro based on blade element momentum theory (BEMT) [27]. The aerodynamic model provided estimates of the time averaged rotor thrust and power as a function of forward speed. The blade velocities were obtained by a vector summation of the rotational component, forward speed and induced velocity. The vertical and horizontal components of induced velocity were assumed constant along the rotor azimuth. Some other key assumptions included uniform distribution of forces along the blade span, a constant drag coefficient (C_d), a linear variation of C_l with alpha, and neglecting the interference of the blades. Using the analysis, Wheatley

performed a case study to investigate feasibility of the cycloidal rotor concept for an aircraft with gross weight of 3000 lbs. The main conclusions of the study were: 1) the aerodynamic principles of the cyclogyro are sound, 2) hovering flight, vertical climb, and a reasonable forward speed may be obtained with a normal expenditure of power, and 3) autorotation in a gliding descent is possible in the event of a power-plant failure.

In 1935, Wheatley and Windler conducted experimental forward flight studies on a cyclorotor [28], and compared the results to theory. Due to the many simplifying assumptions in the aerodynamic model, a good qualitative agreement was found with the experimental results, but the relative magnitudes were significantly different. The wind tunnel tests were performed on a 4-bladed cyclorotor with a diameter and span of 2.4 m and blade chord length of 0.095 m. Rotor performance was studied for speeds up to 45 m/s (87 kt). The rotor power was found to increase at a faster rate with the propulsive force component than with the lift force component. Another interesting conclusion was that blade pitch amplitude affects both rotor propulsive force and power at high speeds, whereas the phasing of blade pitch primarily impacts the lift force component. Although the cyclorotor used in the current work is significantly smaller in comparison, similar trends were observed in the performance studies (Chapter 3).

Kirstens cycloplane concept was revisited in 1943 by Eastman and his colleagues at the University of Washington Aeronautical laboratory (UWAL) [29]. Wind tunnel tests on a relatively large-scale twin-cyclorotor model were conducted (Fig. 1.13). Each cyclorotor had a span and diameter of approximately 3 ft and

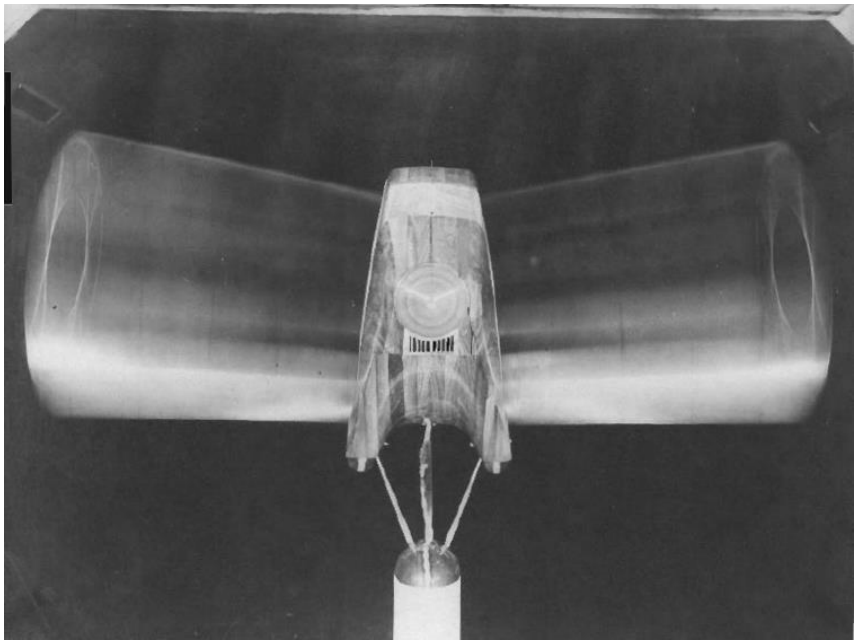

Figure 1.13: Twin-cyclorotor wind tunnel setup at UWAL [29].

consisted of three blades. Each blade had a tapered planform, with a root chord of 8 inches and tip chord of 4 inches; the high taper ratio was an important aspect of the cantilever design. The rotor was tested at various rotational speeds and forward speeds, and at different blade pitch amplitudes. The results showed that the propulsive efficiency of the rotor improves with increasing forward speed, since no additional surfaces are added for propulsion. Also, a high angle of climb/descent were shown to be possible with the thrust-vectoring capability of the rotors. In regard to control, the study showed that vehicle roll and yaw can be achieved by differential control between the blades on the left and right rotors. Furthermore, the driving torque applied to each rotor was balanced by virtue of the counter-rotating rotors. The study concluded that "the prospect of a rotating wing aircraft having good economy and high forward speeds appears extremely bright" [30].

Apart from a few patents [32–35], there is a significant lapse in cyclorotor research between the years 1946 to 1998. The lack of advanced structural materials, limited aerodynamic tools, and the success of the helicopter during these years led to decreased interest in the cyclorotor concept for aircraft applications. It should be noted, however, that research in wind turbine and marine propulsion applications for the cyclogiro continued during this time period.

1.5.2 Modern Developments (1998–2013)

Within the past two decades, developments in high-strength, lightweight materials (e.g. carbon composites), miniaturized electronic and mechanical systems and precision manufacturing processes such as computer numerical controlled (CNC) milling and 3-dimensional rapid prototyping have fostered a renewed interest in the cyclorotor concept. Whereas the early part of the 20th century pursued full-scale aircraft applications of the cyclorotor, the new progress in cyclorotor research has been focused toward UAV and MAV-scale applications.

The Bosch Aerospace Company finally revived interest in the cyclorotor concept in 1998, although this time it was for UAV-scale applications and not full-scale aircraft [36, 37]. In November 1997, the Department of Defense (DoD) released a Request for Proposal (RFP) which called for an "innovative propulsion system for an unmanned aerial vehicle," and Bosch Aerospace was awarded a contract for its cycloidal propeller proposal [36]. In the design of the cycloidal propeller, the target thrust and speed were determined based on the Navy's specifications for a UAV,

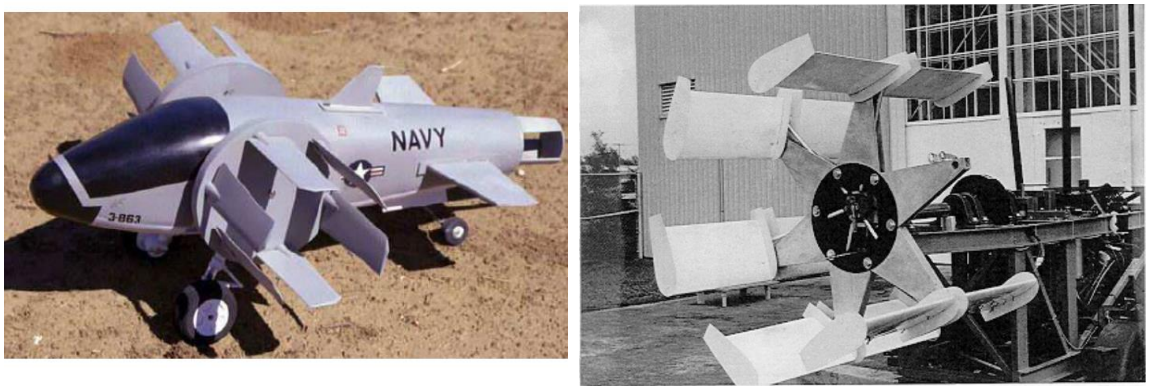

(a) Mockup of a cyclocopter UAV. (b) Bosch 6-bladed propeller.

Figure 1.14: Bosch Aerospace Cycloidal Propeller [36,37].

which included a gross weight of 600 lbs, a maximum speed of 120 kts, a range of 150 miles and a hover requirement at 4000 ft MSL at 95°F. The propeller diameter was limited to 4 ft due to operations on a ship deck environment. The cycloidal-based UAV would be similar to Kirstens two rotor design, although a small cyclo-tailrotor would be added for directional control (Fig. 1.14a). McNabb [38] at the Mississippi State University developed an aerodynamic model to predict the rotor dimensions required to meet the performance requirements. The final rotor design, shown in Fig. 1.14b, was a 6-bladed rotor, with a span of 2 ft, chord length of 1 ft and a diameter of 4 ft. The aerodynamic model predicted 350 lbs of lift at 650 rpm. One of the significant conclusions from this work was the relatively low noise signature of the rotor, compared to a conventional helicopter rotor. Furthermore, the experimental results showed high power loading values of up to 10.88 lbs/lb. Although an aircraft was not built, the study re-established the feasibility of the cycloidal rotor for aircraft applications, particularly at the UAV-scale.

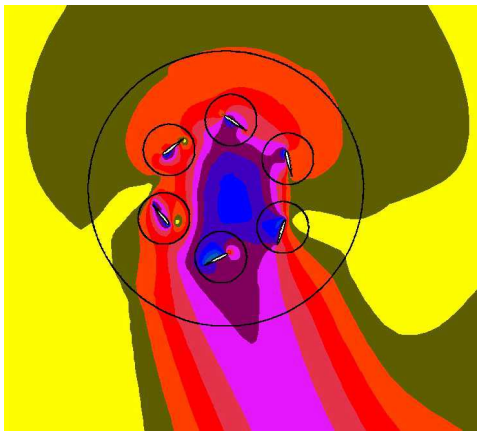

(a) CFD velocity contours.

(b) 43 kg twin-cyclocopter UAV.

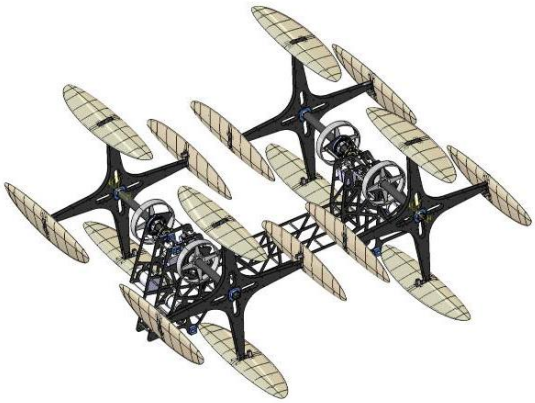

(c) CAD rendering of quad-cyclocopter.

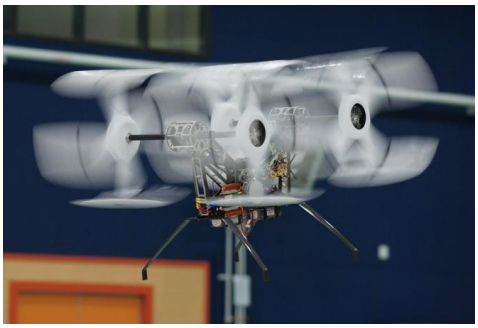

(d) Quad-cyclocopter in free-flight.

Figure 1.15: Cyclorotor research at the Seoul National University. [39–43].

A significant amount of cyclorotor research was conducted by Kim, et. al. at the Seoul National University in South Korea between since 2003 to present [39–43]. Both computational and experimental studies were conducted at the UAV-scale, and a hover-capable cyclorotor based aircraft was successfully built and flight tested in hover. A 2-dimensional CFD analysis was conducted using a commercial software, STAR-CD, and a moving mesh method was adopted to simulate the rotor blades with the periodic pitch angle variation [41]. A low Reynolds number turbulence model ($k - \epsilon$ model) was included in the analysis, and both structured and unstructured meshes were used to model the blade system. The imposed boundary conditions included the pressure, no-slip wall, and symmetry plane boundary conditions. The CFD predictions were compared to experimental measurements and provided good agreement for rotor thrust, but the power values were slightly under-predicted by the analysis.

The CFD analysis and experimental results were used to aid the design of a 48 kg twin-rotor cyclocopter UAV (Fig. 1.15b), which was successfully tested in tethered hover [40]. More recently, a smaller 12.8 kg quad-cyclorotor vehicle was built and successfully tested in free flight (Fig. 1.15d) [43]. Each rotor consisted of four elliptical blades, a span and diameter of approximately 0.5 m, a NACA0018 airfoil, and operated at a rotational speed of 1100 rpm. The vehicle was equipped with a commercial 'off-the-shelf' attitude heading reference system (AHRS) for providing attitude information to an on-board flight control system (FCS), and the pilot inputs were throttle, pitch, roll and yaw.

Most previous studies on cycloidal rotors were focused on full-scale or UAV-

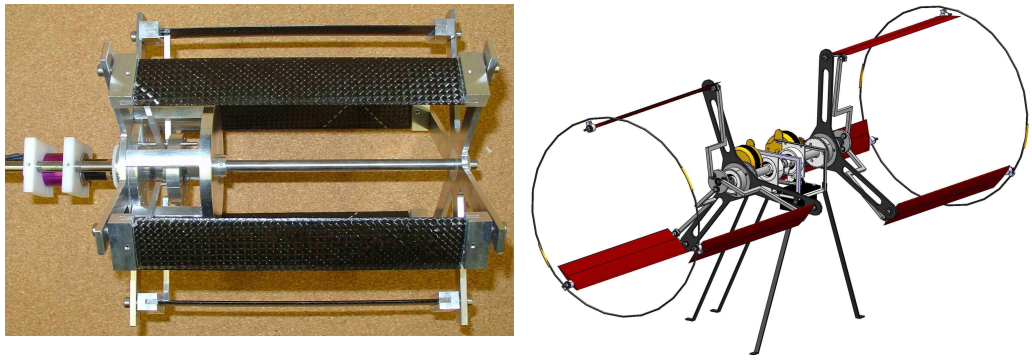

(a) Cyclorotor experimental setup. (b) Twin-cyclocopter MAV concept.

Figure 1.16: Cyclorotor work at UMD in 2007 [45].

scale aircraft applications. In 2006, Sirohi, Parsons and Chopra at the University of Maryland conducted a feasibility study for MAV-scale applications [44, 45]. Experimental studies were conducted on a small-scale cyclorotor with dimensions of approximately 15 cm in diameter and span. The rotor thrust and power were measured in hover, and the primary parameters varied included the rotational speed, blade pitch amplitude and number of blades. An analytical model was developed and compared with the experimental results. The lift and drag forces were calculated based on unsteady indicial aerodynamics assuming attached flow. The induced angle of attack resulting from the rotor downwash was calculated using a double-multiple-streamtube model. The model showed good agreement with experimental results for rotor thrust, but over-predicted the power values. One possible reason for the differences in power could have been in the cyclorotor design. The experimental rotor (Fig. 1.16a) was over designed and the tare power accounted for nearly 75% of the total power, which could have led to discrepancies in the measurements. Overall,

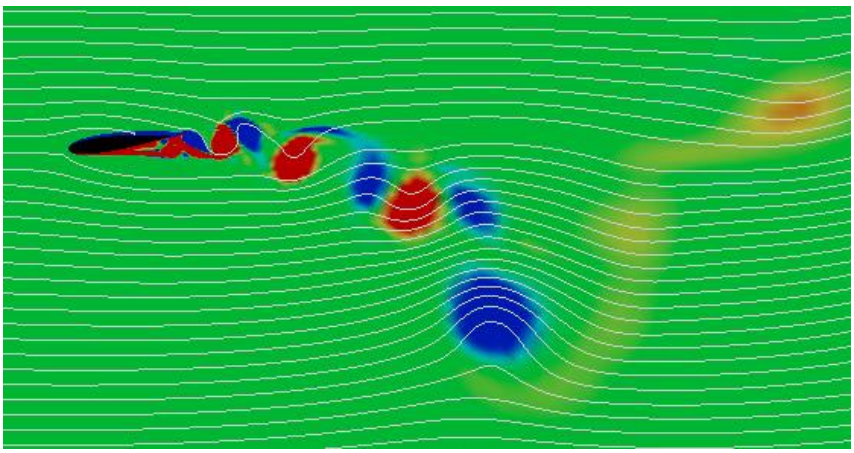

Figure 1.17: CFD vorticity contour plot [46].

the study concluded that the cyclorotor concept was feasible in the low Reynolds number regime in which MAVs operate.

In 2007, Siegel et. al [46] at the US Air Force Academy performed 2-D CFD analysis to investigate the capability the cyclorotor blades to use unsteady, dynamic lift to augment thrust production at MAV-scale Reynolds numbers. The simulations were conducted using commercial software (Cobalt flow solver). In the code, the full compressible Navier-Stokes equations are solved based on the Finite Volume Formulation, and the numerical method was formally second order accurate in both space and time. The chord Reynolds number was set to Re=10,000, the time step was set to Δt=0.1 and the Mach number was set to M=0.1 to ensure computational efficiency. A one-bladed cycloidal rotor was modeled as an airfoil with pitch and heave motion, and a circular motion superimposed.

A few case studies were performed to investigate the effect of airfoil section, grid resolution, forward speed, rotational speed, radius of the airfoil motion, pitch amplitude and phase angle. Some of the conclusions from the study were as follows. The difference in performance between a NACA0012 and NACA0015 section was negligible. Finer grid resolutions preserved vortices further away from the airfoil, but did not have a strong impact on the average forces or vortex shedding frequencies. The study also provided a few interesting insights into the flow physics of the cycloidal rotor. In the half of the circular trajectory where the blade moves downward, the blade is first accelerated with respect the freestream and then decelerated. This favors early dynamic stall vortex formation, leading to increased thrust production. The opposite effect is shown to occur during upward motion of the blade, where a weaker dynamic stall vortex formation leads to decreased thrust production.

Overall, the study was limited in scope as it only used a one-bladed cyclorotor in the simulations, and only included a few test cases. Some of the suggestions from the study included: 1) blade-vortex interactions could enhance the thrust producing capability of the cyclorotor, 2) both energy extraction and thrust production could be achievable depending on the pitching kinematics and 3) the cyclorotor may be a mechanically simpler solution to use unsteady mechanisms to improve thrust production compared to platforms such as the flapping-wing.

In 2010, Nakaie et. al. conducted experimental flow field measurements on a cycloidal propeller [47]. Phase-averaged particle image velocimetry (PIV) techniques were used to obtain the flow field measurements (Fig. 1.18). Timing and control of the PIV system was achieved using a rotary encoder, a pulse counter and a

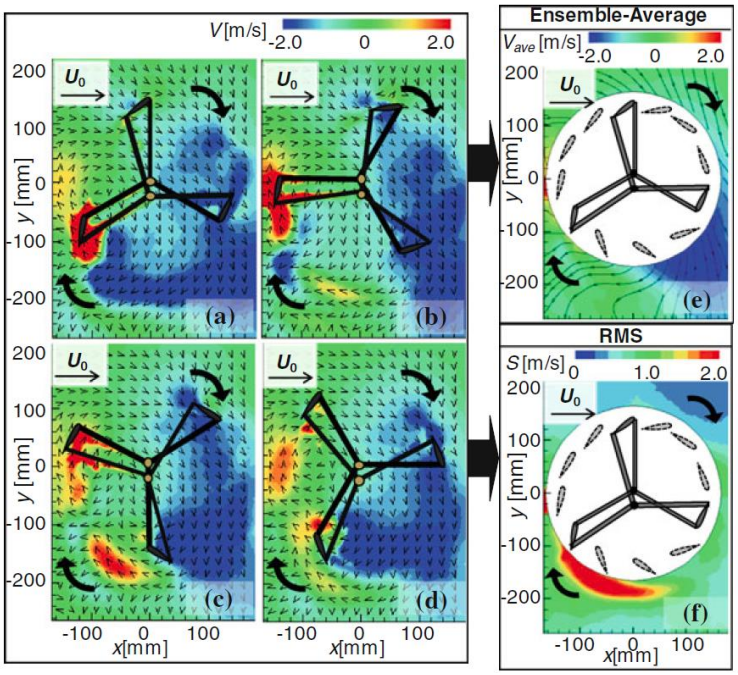

Figure 1.18: 2-D PIV velocity measurements on cyclorotor [47].

synchronizer. A 3-bladed, with a span and diameter of approximately 0.24 m, was tested in hover at a chord Reynolds number of Re = 14,000. Both varying (sinusoidal) and non-varying pitching kinematic were examined. Flow characteristics such as mean velocity, vorticity and the root mean square (RMS) value of velocity fluctuation were obtained. The key conclusions of the study were: 1) a downward flow (i.e. momentum addition to the flow) was observed for varying pitch kinematics and not for constant pitch kinematics 2) larger velocity fluctuations were observed beneath the propeller than above and 3) reattaching flow and vortex shedding were observed at various positions along the circular path of the blades.

Between 2008 and 2012, comprehensive experimental and analytical studies on a MAV-scale cycloidal rotor were performed at the University of Maryland (UMD) by Benedict et. al. [17, 48–50]. Systematic experimental measurements were con-

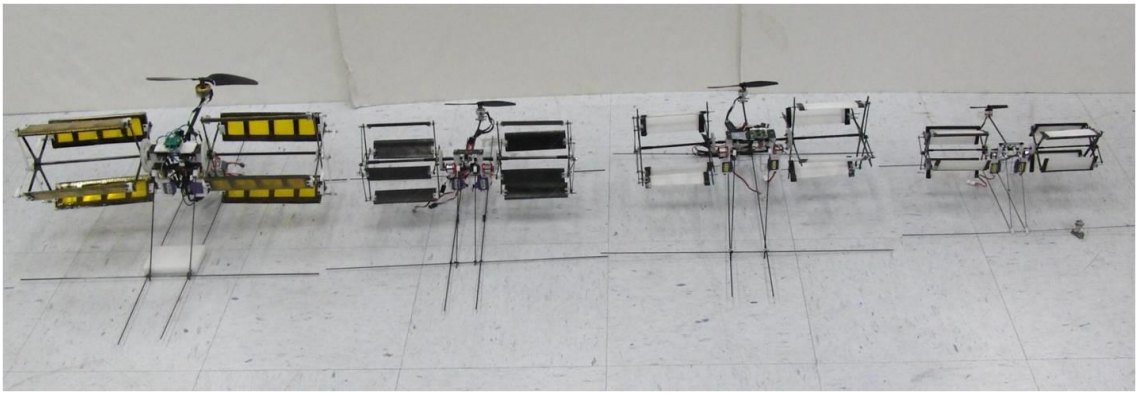

(a) Hover-capable cyclocopter MAVs developed at UMD.

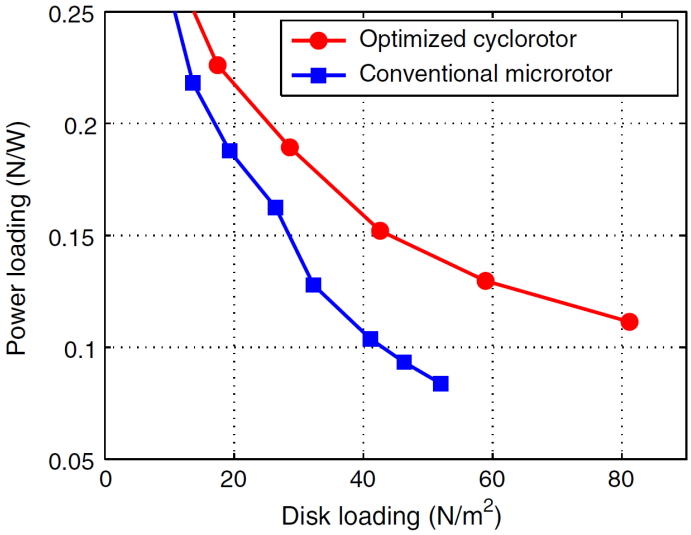

(b) Aerodynamic power loading of conventional MAV rotor versus optimized cyclorotor.

Figure 1.19: Cyclorotor research at the University of Maryland performed by Benedict et. al. [48–50]

ducted on a cyclorotor with dimensions of approximately 15 cm in span and diameter to examine the effects of a wide range of parameters in hover. Some of the parameters tested include: blade airfoil, rotor span and radius, rotor solidity, number of blades, blade chord length, blade planform, blade pitching amplitude and phase, and symmetry of pitching kinematics. Based on the experimental results, an optimized rotor configuration was developed and implemented on a series of hover-capable (un-tethered) cyclocopter MAVs (Fig. 1.19a). The optimized cyclorotor was shown to provide higher values of aerodynamic power loading compared to a conventional edgewise rotor of similar scale. The experimental studies and successful development of a hover-capable cyclocopter MAV established the feasibility of the concept at the MAV-scale.

Benedict [48] performed a detailed analysis on cyclorotor with dimensions of 15 cm in span and diameter. An aeroelastic model was developed and coupled with an unsteady aerodynamic model to predict thrust production. The aeroelastic analysis was performed using two approaches: 1) a second-order non-linear beam FEM analysis for moderately flexible blades and 2) a multi-body based large-deformation analysis incorporating a geometrically exact beam representation. The unsteady aerodynamic analysis was conducted with two different inflow models, which included a single streamtube and a double streamtube model. The analysis was able to predict average thrust with sufficient accuracy over a wide range of rotational speeds, pitching amplitudes and number of blades.

In 2010, Yang et. al. [51, 52] at UMD performed detailed 2-D and 3-D CFD simulations of a MAV-scale cycloidal rotor in hover. The objective of the

study was to develop a computational methodology to understand the complex aerodynamics of the cyclorotor in hover. The simulations were performed using a compressible structured overset Reynolds-Averaged Navier-Stokes (RANS) solver (OVERTURNS). The mesh solver utilized the diagonal form of the implicit approximate factorization method with a preconditioned dual-time scheme to solve the compressible RANS equations. The computations were performed in the inertial frame in a time-accurate manner. The inviscid terms were computed using a third-order MUSCL scheme with Roe flux difference splitting and Korens limiter, and the viscous terms were computed using a second-order central differencing scheme. A low Mach pre-conditioner based on Turkels method was implemented to accelerate the convergence and ensure accuracy of the solution. In the 3-D calculations, the Spalart-Allmaras turbulence model was used for RANS closure. However, due to convergence problems with the Spalart-Allmaras model in the 2-D simulation, a two-layer algebraic 0-equation turbulence model developed by Baldwin and Lomax was employed.

The CFD results were compared with experimental results at various rotational speeds and blade pitch amplitudes. The results showed good agreement for the rotor vertical force, but the sideward force and power were under-predicted by the CFD analysis. A comparison of the 2-D and 3-D CFD simulations showed strong 3-D effects, but the differences in time-averaged forces were not significant. Figure 1.20 shows the 3-D CFD predicted flow field of the cyclorotor in hover. The flow field predicted by the 3-D CFD was also compared with experimental PIV measurements. The CFD predicted flow field showed good similarity with the PIV flow

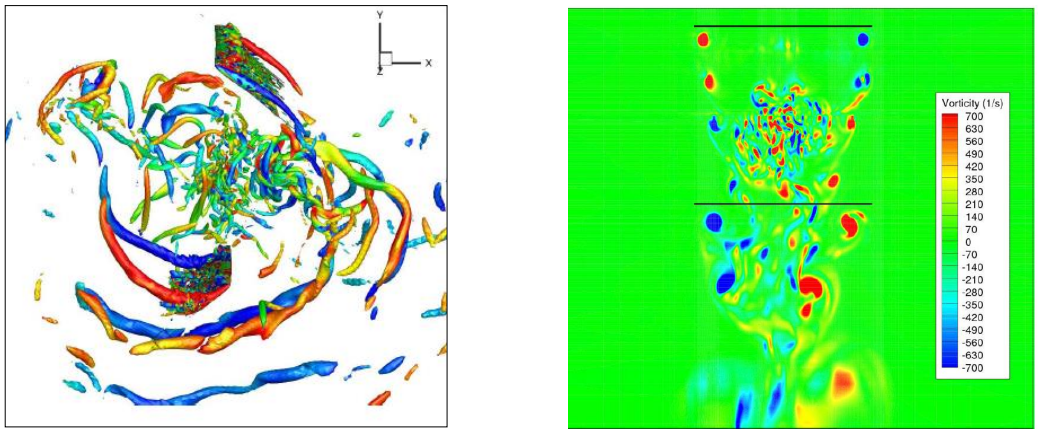

(a) 3-dimensional CFD predicted flow field.

(b) Evolution of tip blade vortices.

Figure 1.20: 3-D CFD cyclorotor simulations performed at the University of Maryland by Yang et. al. [51,52].

field measurements. Some of the flow features observed included: 1) the presence of blade tip vortices which varied in strength as the blade moved along its circular path, 2) a skewed wake structure, 3) wake contraction in the span-wise direction, 4) unsteady shedding, and 5) blade vortex interactions.

Recently, Hrishikeshavan et. al. [53] at UMD conducted one of the first studies to experimentally analyze the maneuverability and disturbance rejection characteristics of a cyclocopter MAV in hover. The study was conducted on a 500 g twin-cyclocopter MAV (Fig. 1.21a). The two cyclorotors on the vehicle provided lateral and directional control, and a tail rotor provided pitch attitude control. The control variables included: 1) rotational speed of each cyclorotor, 2) rotational speed of the tail rotor, and 3) direction of thrust of each cyclorotor. The vehicle was equipped with a 3 g onboard processor, which used a proportional-derivative controller for attitude stabilization.

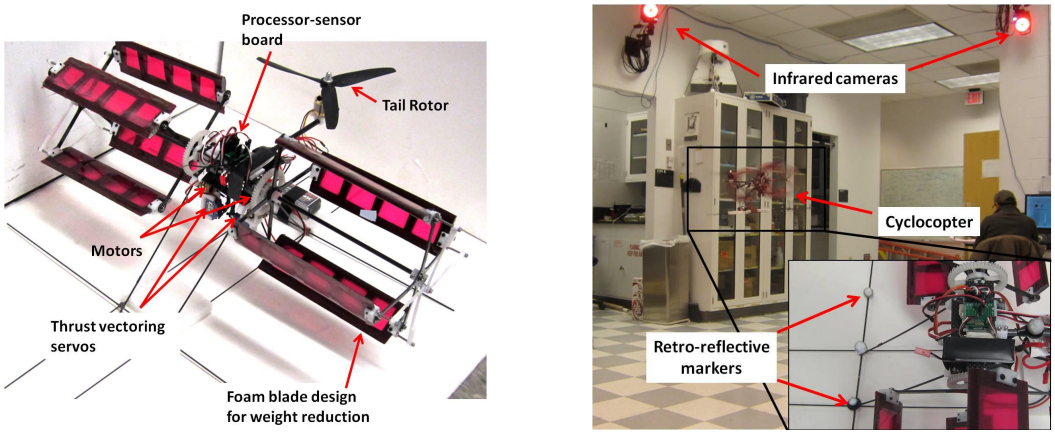

(a) 500 g twin-cyclocopter MAV.

(b) Motion capture system.

Figure 1.21: Flight system identification studies performed by Hrishikeshaven et. al. at the University of Maryland [53].

The experiments were conducted using a motion capture system (Fig. 1.21b). Once the vehicle achieved stable hover, the vehicle was provided with various excitations (inputs), and the states of the vehicle and actuator inputs (outputs) were recorded by the motion capture system and on-board processor. A flight dynamics model was then extracted using time domain system identification techniques based on the input-output data. Furthermore, the identified flight dynamics model was used in conjunction with a control-theoretic framework in order to quantify the maneuverability and disturbance rejection characteristics of the cyclocopter. The key conclusions from the study can be summarized as follows: 1) the cyclocopter is inherently unstable and requires feedback regulation, 2) a strong gyroscopic coupling is present between roll and yaw degrees of freedom, 3) the gyroscopic coupling and absence of damping in attitude dynamics can provide a high maneuverability potential in open-loop condition and 5) the longitudinal and lateral gust tolerances

of the vehicle were estimated at 7.9 m/s and 17 m/s, respectively.

1.6 Objective of Present Work

The current study is a continuation of the previous studies at the University of Maryland [48–53]. Whereas the previous studies were focused on understanding and improving rotor performance in hover, the current research aims to explore the forward flight capability of the cyclorotor through systematic performance studies and flow field measurements. Apart from the few experiments by Wheatley [28] and Eastman [29] in the early 1900s, there have not been any significant experimental studies on the cycloidal rotor in forward flight. Therefore, one of the primary objectives of the current study is to perform wind tunnel experiments to understand the effects of blade pitching kinematics and rotor geometry in forward flight, and to use these results to determine the power consumption and control input requirements that would be required for a cyclocopter MAV such as the one shown in Fig. 1.21a (i.e. trimmed, level performance).

Furthermore, many of the early theoretical studies [26,27] were based on simplifying assumptions and therefore cannot provide a detailed understanding of the cyclorotor flow physics. The analytical studies conducted within the past two decades provided a few key insights, but are still limited due to the lack of tools that accurately model aerodynamics at low Reynolds numbers. Therefore, another important objective of the current work is to examine cyclorotor flow physics in forward flight using an experimental approach (PIV), and to correlate the results with analytical

studies (CFD).

The specific objectives of the performance measurements can be summarized as follows:

(1) To understand the effects of pitching kinematics (pitch amplitude, phase angle and mean pitch angle) on cyclorotor lift, propulsive force and power by systematically varying each parameter at multiple advance ratios.

(2) To determine the trimmed, level flight performance of the cyclorotor by interpolating the time-averaged force measurements. Specifically, to examine the rotor power consumption, lift to drag ratio and control input requirements at different forward speeds, and evaluate the effects of:

- Varying lift
- Varying propulsive force
- Varying rotational speed
- Asymmetric pitching kinematics

(3) To understand the effects of rotor geometry (chord/radius ratio and blade pitching axis location) on the lift and propulsive force producing efficiency of the cyclorotor.

The objectives of the flow field studies are as follows:

(1) To obtain the time-averaged flow field from PIV experiments at different advance ratios and examine the flow velocities along the rotor azimuth.

(2) To determine the phase-averaged flow field from PIV experiments at different advance ratios and investigate the role of unsteady aerodynamics in blade force production.

(3) To correlate the PIV measurements to time-averaged force measurements as well as CFD predictions from previous studies to examine the flow physics behind force production.

The two approaches discussed above will help provide an understanding of the operating principles of the cyclorotor in forward flight, which in turn may aid in the future development of an efficient, forward flight capable cyclorotor-based micro air vehicle.

1.7 Thesis Organization

The key technical challenges faced at the micro air vehicle scale and a discussion of existing MAV platforms has been presented in the current Chapter. Furthermore, a literature review of previous work on cycloidal rotors has been provided, and the motivation for the current research has also been established.

Chapter 2 explains the basic operating principle of the cyclorotor. A discussion of the ideal pitching kinematics, the four-bar based mechanism used to emulate these pitching kinematics, and the experimental validation of the pitching mechanism are provided. The notation and coordinate system used for the forward flight studies are also presented.

Chapter 3 focuses on time-averaged force and power measurements. The effects

of the blade pitching kinematics on cyclorotor force production are investigated at different advance ratios. These results are then interpolated to determine the trimmed, level flight performance of the cyclorotor; in these studies, a 500 g twin-cyclocopter MAV is used to derive the baseline case.

Chapter 4 examines the flow field of the cyclorotor in forward flight. A combination of flow visualization images and PIV measurements are used to explain the underlying physics of cyclorotor force production. Both the time-averaged and phase-averaged flow fields are examined at different advance ratios. The PIV measurements are correlated with both experimental force measurements as well as CFD predictions from previous studies.

Chapter 5 consists of experimental measurements to help identify the role of flow curvature effects (virtual camber and incidence) on cyclorotor aerodynamic performance. Two important rotor geometric parameters were systematically varied in these studies, which included the chord/radius (c/R) ratio and blade pitching axis location.

Chapter 6 concludes this thesis by providing a discussion of the key findings in this work. The Chapter also provides suggestions for future experiments, which may further the progress toward an efficient, high-speed flight capable cyclocopter MAV.

Chapter 2: Cycloidal Rotor Operating Principle

2.1 Overview

As discussed briefly in Chapter 1, the cyclorotor is a rotary-wing system which consists of a set of blades that rotate about a horizontal axis, with the blade span parallel to this axis. The current Chapter explains the the basic operating principles of the cyclorotor, and presents the notation used throughout the remaining chapters.

2.2 Forward Flight Coordinate System

The coordinate system used for the cyclorotor is shown in Fig. 2.1. The incoming flow velocity is from left to right, and the rotor operates in the clockwise direction. The lift and propulsive force components are defined as the net aerodynamic forces produced along the positive Z-axis and Y-axis, respectively. The advance ratio (μ) is defined as the ratio of the incoming flow velocity to the blade translation speed:

$$\mu = \frac{U_\infty}{\Omega R} \tag{2.1}$$

In forward flight, the top half of the cyclorotor ($\psi = 0^\circ$ to 180°) is the 'retreating' side, and the bottom half of the rotor ($\psi = 180^\circ$ to 270°) is the 'advancing' side.

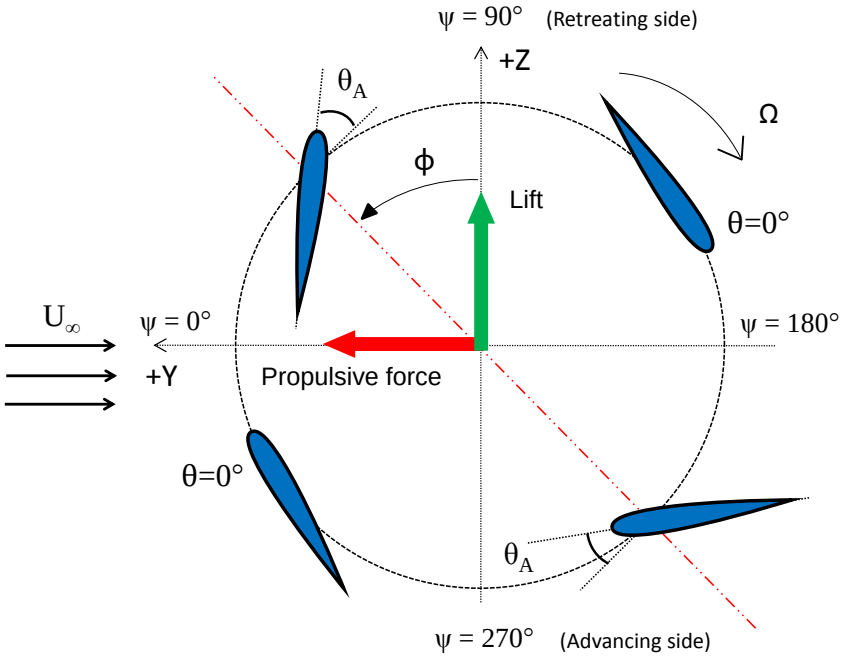

Figure 2.1: Cyclorotor coordinate system.

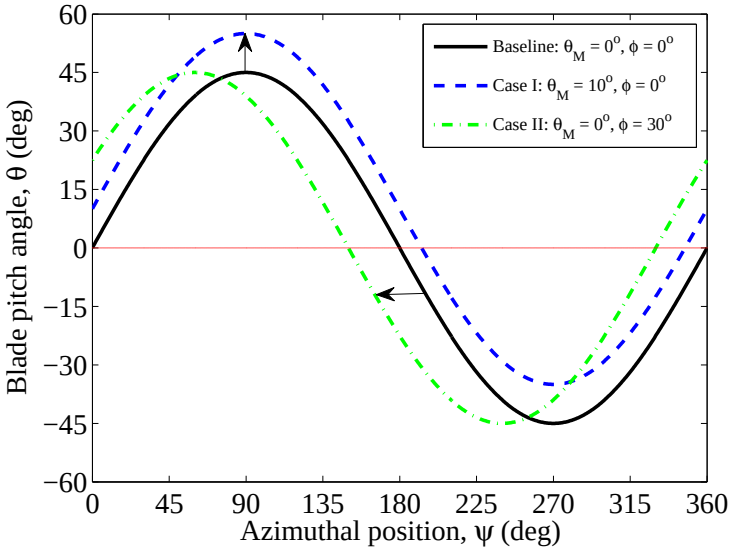

Figure 2.2: Blade pitch angle as a function of rotor azimuth showing effects of mean pitch angle and phase angle at a peak-to-peak amplitude of 90°.

2.3 Blade Pitching Kinematics

2.3.1 Ideal Pitching Kinematics

As each blade of the cyclorotor translates along the circular path, a passive pitching mechanism allows the blade to achieve a harmonic pitching schedule (Fig. 2.2). The pitching kinematics in turn allow the rotor to produce a net non-zero aerodynamic force. The blade pitch angle, defined as the angle between the blade chord line and the tangent to the circular trajectory, can be represented as the following sinusoidal function:

$$\theta(\psi) = \theta_M + \theta_A sin(\psi + \phi) \tag{2.2}$$

In Eq. 2.2, ψ represents the azimuthal position of the blade along its circular path. The azimuth angle is measured in the clockwise direction from the positive Y-axis (i.e. in the direction of rotation), as shown in Fig. 2.1.

The mean pitch angle, θ_M, defines the symmetry of the blade pitching kinematics. A zero mean pitch angle allows the blade to obtain the same pitch angles in both halves of its trajectory, as illustrated by the baseline case in Fig. 2.2. In contrast, a non-zero mean pitch angle allows the blade to achieve higher pitch angles in one half of its circular trajectory compared to the opposing half (i.e. "asymmetric" pitching kinematics). This is illustrated by Case I in Fig. 2.2.

The blade pitch amplitude, θ_A, is the maximum pitch angle the blade achieves along its circular trajectory, as illustrated in Fig. 2.2. In hover, the effect of varying

the blade pitch amplitude is to change the magnitude of the resultant force produced by the cyclorotor.

The pitch phase angle (ϕ) represents a phase shift in the pitching kinematics. The phase angle is measured in the counterclockwise direction from the positive Z-axis (i.e. into the relative flow) (Fig. 2.1). Thus, at a phase angle of 0°, the blade achieves a maximum pitch angle at the top ($\psi = 90°$) and bottom ($\psi = 270°$) points of the circular trajectory. The effect of a positive phase angle is illustrated by Case II in Fig. 2.2. In hover, the effect of varying the phase angle is to change the direction of the resultant force vector. As the cyclorotor transitions from hover to high speed flight, the phase angle increases and approaches a value close to $\phi = 90°$, where the blade achieves a maximum pitch angle at the forward ($\psi = 0°$) and aft ($\psi = 180°$) points of the trajectory. This will be discussed in more detail in Chapter 3.

2.3.2 Four-bar Pitching Kinematics

In order to achieve the harmonic pitching schedule discussed in the previous section, a passive four-bar based pitching mechanism was designed and implemented on the experimental cyclorotor used in this study. The pitching mechanism, shown in Fig. 2.3, is based on a classic "crank rocker" type four-bar linkage system widely used in many mechanical system applications. The four-bar mechanism developed for the cyclorotor was based on previous work [54], although analysis on generic four-bar linkage systems can be found in most classical mechanics textbooks [55].

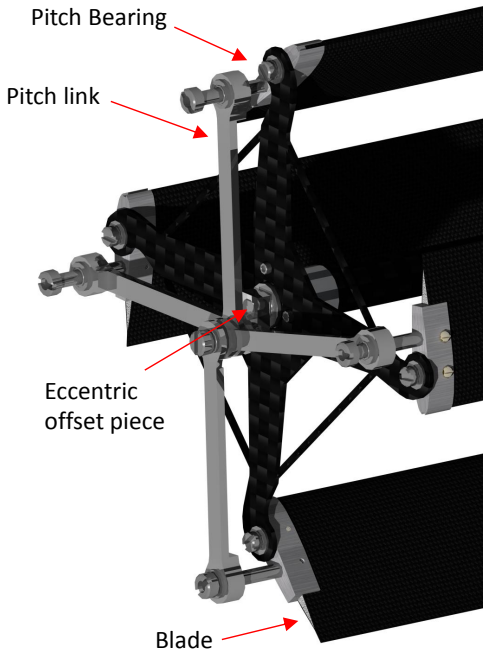

Figure 2.3: Cyclorotor pitching mechanism.

Figure 2.4 shows a schematic of the four-bar linkage system on one blade of the cyclorotor. Points A, B and C represent the center of rotation, blade pitching axis and the blade-pitch link attachment, respectively. The linkages L_1, L_2, L_3 and L_4 are fixed in length throughout the rotation. The description and function of each linkage is presented in Table 2.1. By varying the lengths of linkages L_2 and L_3, the blade pitch amplitude (θ_A) and mean pitch angle (θ_M) can be controlled, respectively. The angle between linkage L_2 and the vertical determines the pitch phase angle (ϕ), as shown in Fig. 2.4.

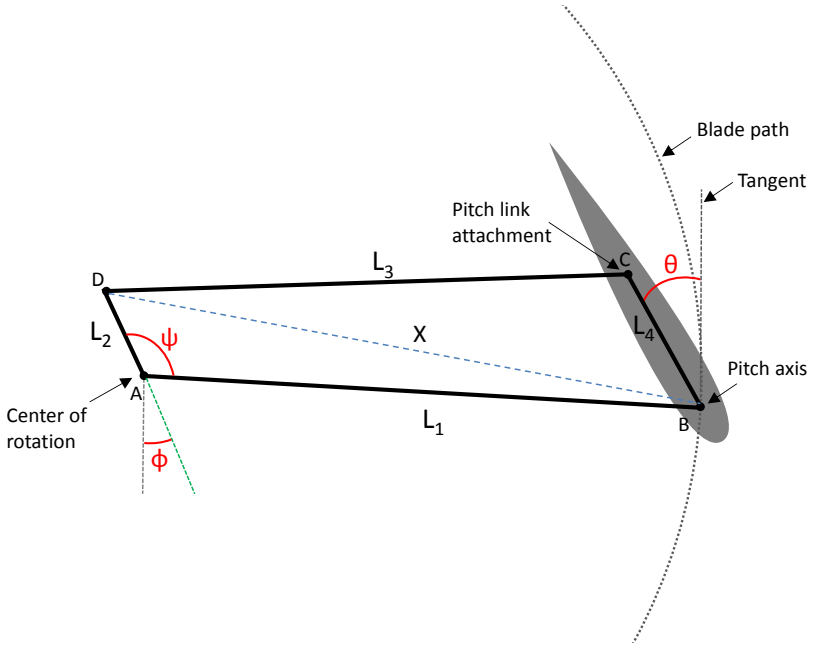

Figure 2.4: Four-bar linkage schematic of cyclorotor blade.

Table 2.1: Description of linkage lengths.

Linkage	Description	Primary function
L_1	Rotor radius	Fixed
L_2	Eccentric offset	Blade pitch amplitude, θ_A
L_3	Pitch link length	Mean pitch angle, θ_M
L_4	Blade pitch axis to pitch link	Fixed
$\angle L_2$	Angle between L_2 and vertical	Pitch phase angle, ϕ

The blade achieves its maximum pitch angle when the segments AD and AB are aligned and the diagonal X becomes *maximum* in length (Fig. 2.4). Similarly, the blade achieves its minimum pitch angle when segments AD and AB and the diagonal X becomes *minimum* in length. The four-bar analysis, along with the linkage lengths used in the current work, are presented in Appendix A.

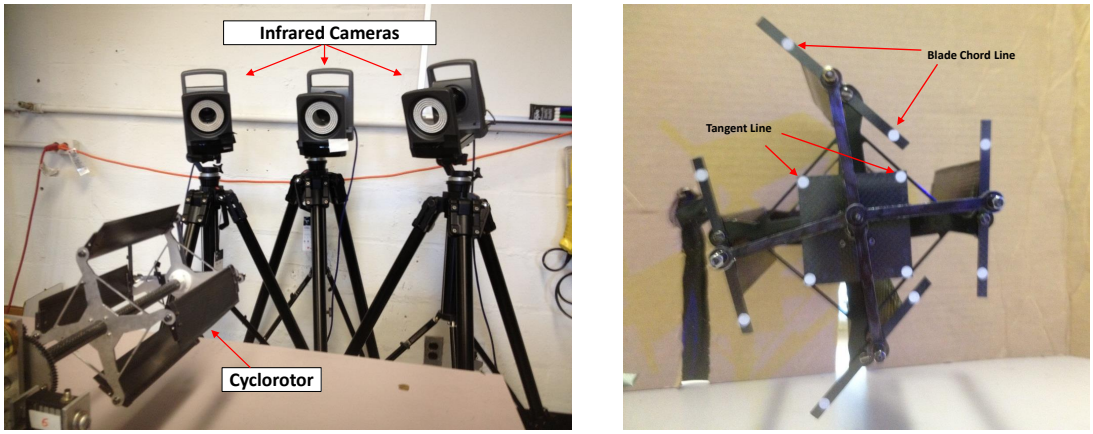

(a) Motion capture system.

(b) Reflective markers on cyclorotor.

Figure 2.5: Experimental setup for pitch angle measurement.

2.3.3 Mechanism Validation

The four-bar based pitching mechanism was validated using experimental measurements from a motion capture system (Fig. 2.5a). The system consisted of three infrared cameras (VICON T-40s system), each consisting of a maximum frame rate of approximately 300 Hz at full resolution. Each of the blades of the cyclorotor were equipped with two pairs of reflective markers, one pair for defining the blade chord line and the corresponding pair defining the tangent to the circular path (Fig. 2.5b). Together, these markers provided a measure of the blade pitch angle. Additional

markers were placed outside of the rotor frame to define the inertial axes. These markers provided measurements of the blade azimuthal position. The tests were conducted with the camera capture rate set at 250 Hz. The cyclorotor was tested for several rotational speeds in the range of 400 to 1000 rpm (6.7 Hz to 16.7 Hz), although there was no variation in the pitch angle measurements.

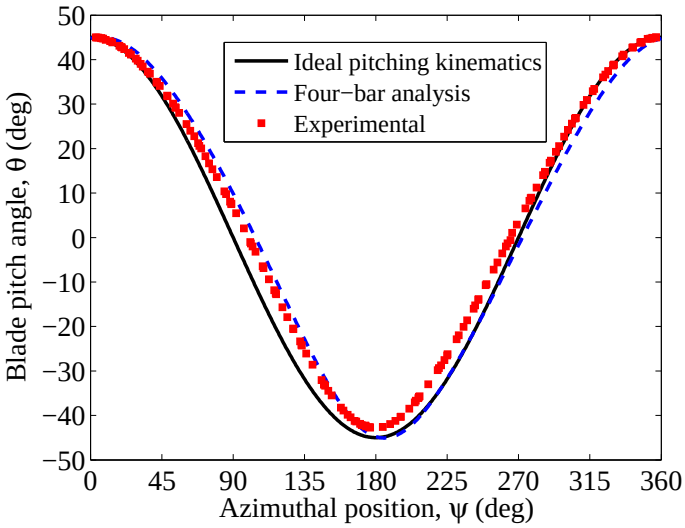

Figure 2.6: A comparison between ideal, four-bar analysis, and measured pitch angle variation at a peak-to-peak pitch amplitude of 90°.

Figure 2.6 shows the pitch angle variation obtained from the experimental measurements, as well as the ideal pitching kinematics and the four-bar analysis. The experimental measurements represent 7 full rotor revolutions, with the rotor operating at 600 rpm. The results in Fig. 2.6 provide two important insights. First, they show that the experimental measurements agree well with the four-bar analysis, although both results have a slight phase difference compared to the ideal pitch angle variation. Second, it shows the repeatability in the pitching kinematics.

2.4 Summary

In this Chapter, the basic operating principle of the cyclorotor was explained. The three blade kinematic parameters of pitch amplitude (θ_A), pitch phase angle (ϕ) and mean pitch angle (θ_M) were introduced. Also, the coordinate system used in forward flight was presented. The second half of the Chapter focused on the passive, four-bar based pitching mechanism implemented on the experimental cyclorotor. Lastly, the mechanism was validated using experimental measurements from a motion capture system. The results were compared with both the ideal kinematics and the four-bar analysis.

Chapter 3: Performance Measurements: Pitching Kinematics

3.1 Overview

As discussed in Chapter 1, the cyclorotor concept was introduced nearly a century ago, yet the number of scientific studies on the concept since then has remained scarce. The few existing studies on cyclorotors were either conducted at relatively large scales (Reynolds Number >100,000) or primarily restricted to the hover condition [21–48]. None of the previous studies examined the forward flight capability of a cyclorotor, especially at the micro air vehicle-scale. Therefore, one of the primary goals of the current research was to perform systematic wind tunnel studies on a small-scale cyclorotor, consisting of a diameter and span of approximately 15 cm. The results from these experiments form the content of the current chapter.

The current Chapter is organized as follows. First, the experimental setup and testing procedures for the wind tunnel experiments will be discussed. In the following section, experimental results will be presented in two parts: 1) fixed control inputs and 2) trimmed, level flight. The first part of the results (fixed control inputs) examines the effects of blade pitching kinematics on rotor aerodynamic performance at different advance ratios. Each blade parameter (blade pitch amplitude, pitch phase angle and mean pitch angle) is systematically varied while the remaining

parameters are held constant. The second part of the results focuses on cyclorotor performance in straight and level flight conditions. The results from the parametric studies are interpolated to determine the power consumption, lift-to-drag ratio and control input requirements at various forward speeds. The findings from the wind tunnel studies will be summarized in the final section. The aim of the current Chapter, therefore, is to provide a well-rounded understanding of the forward flight capability of the cyclorotor concept, which may aid in the future design and development of an efficient, forward flight capable cyclocopter MAV.

3.2 Experimental Apparatus and Procedure

Time-averaged force measurements were obtained for a small-scale cyclorotor in an open-jet wind tunnel. The current section provides a discussion of the experimental setup and testing procedures.

3.2.1 Experimental Cyclorotor

The experimental cyclorotor used in the wind tunnel studies is shown in Fig. 3.1a. The corresponding rotor dimensions are listed in Table 3.1. These dimensions were selected based on previous performance optimization studies conducted in hover [48]. Although these dimensions may not represent the optimal rotor configuration for forward flight, they provide a good starting point for the current studies. Moreover, the focus of the wind tunnel studies was not to optimize the rotor geometry, but rather to understand the dependence of the rotor aerodynamic performance on

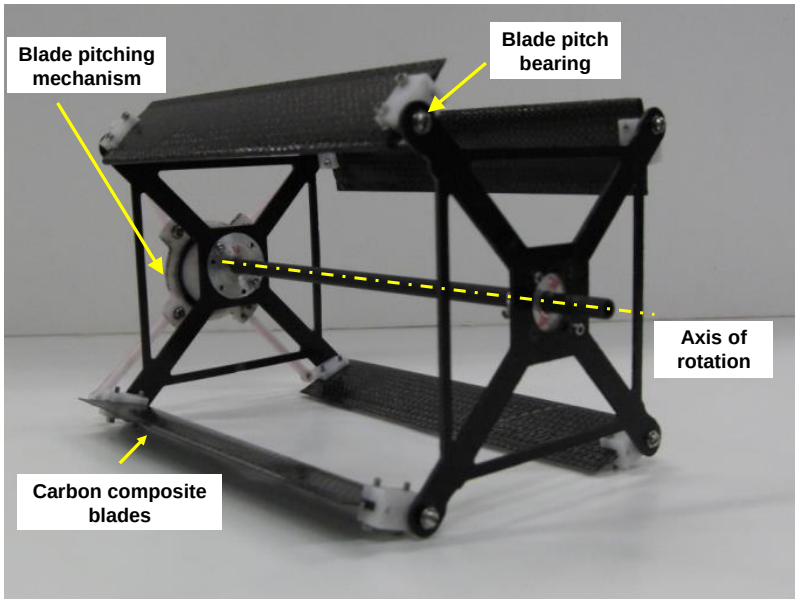

(a) 4-bladed cyclorotor.

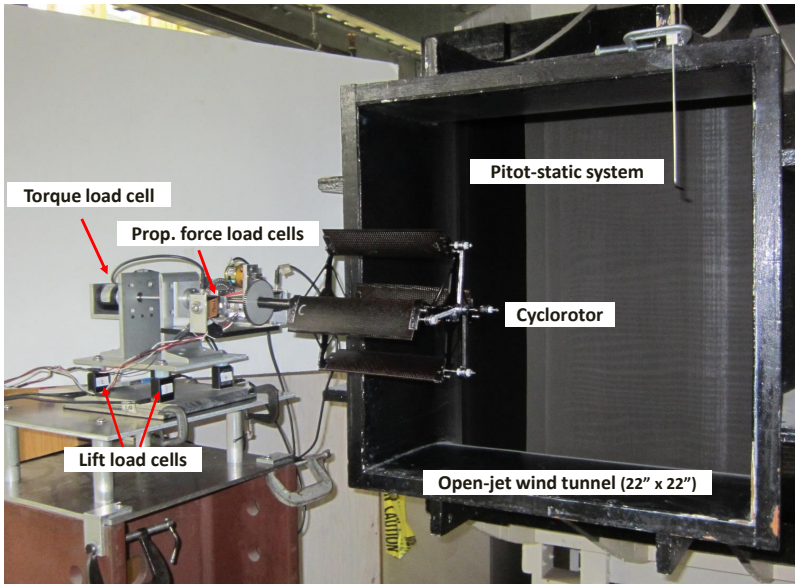

(b) Wind-tunnel force balance setup.

Figure 3.1: Experimental setup.

blade pitching kinematics. The dimensions of the cyclorotor remained unchanged throughout all experiments in the current Chapter.

3.2.2 Wind Tunnel

The experiments were performed in an open-jet/open-circuit wind tunnel facility at the University of Maryland. The"free-jet" wind tunnel consisted of test section dimensions of 0.56 m×0.56 m, a contraction ratio of 0.13, and a turbulence level of 0.25%. The tunnel speed was varied using a variac, and the maximum operational speed was 35 m/s. The airspeed at the test section was measured using a pitot-static system (Fig. 3.1b). Measurements of ambient temperature and pressure were obtained prior to each set of experiments, and the corresponding values of air density were calculated based on these values.

Table 3.1: Experimental cyclorotor dimensions.

Parameter	Measurement
Number of blades (N_b)	4
Blade span (b)	0.159 m (6.25 in)
Blade chord length (c)	0.0495 m (1.95 in)
Rotor radius (R)	0.076 m (3 in)
Airfoil section	NACA 0015

3.2.3 Force Balance and Data Acquisition

A key challenge in the current research involved the design and development of a precise 3-component wind tunnel force balance (Fig. 3.1b) to accurately measure the lift, propulsive force and shaft torque of the cyclorotor. The force balance consisted of four vertically mounted compression/tension load cells to measure the rotor lift component, three horizontally mounted load cells to measure the propulsive force component, and a reaction torque sensor to measure shaft torque. Each load cell had a maximum loading capacity of 1.14 kg and provided a measurement accuracy of ± 0.6 g. The reaction torque sensor consisted of a maximum torque capacity of 0.71 N-m and a measurement accuracy of $\pm 7.1 \times 10^{-4}$ N-m. A detailed schematic of the experimental setup and information on the measurement devices are provided in Appendix B.

Voltage measurements from the load cells and torque sensor were acquired using a data acquisition (DAQ) system which consisted of: 1) signal conditioning connector block (NI SC-2345) 2) high speed USB screw terminal (NI USB-6251) 3) full-bridge input modules (SCC-SG24) and 4) computer equipped with data acquisition software (LabVIEW 8.6). The complete setup is shown in Fig. 3.2. The force balance was systematically calibrated and periodically checked using calibration weights. A 3×3 decoupling calibration matrix was obtained by applying axial loads along the X- and Z-axis directions and a torque load about the X-axis (see Fig. 3.3 for reference). The decoupling calibration matrix was used to convert the measured voltages into force and torque values.

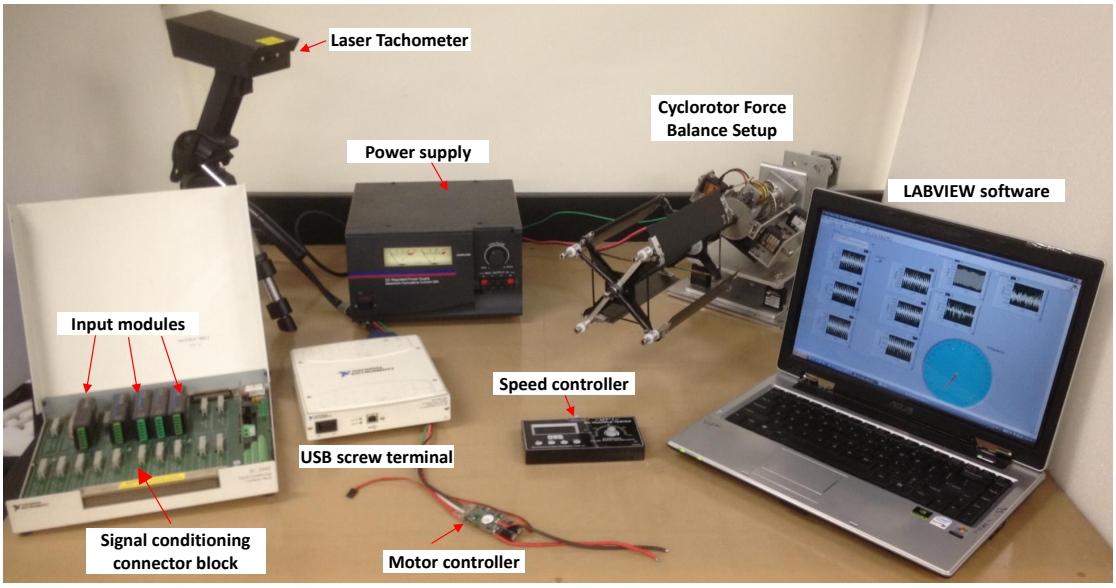

Figure 3.2: Data acquisition system.

Time-averaged force and torque values were obtained by averaging the instantaneous measurements over a period of 5 seconds. The instantaneous data was acquired at a rate of 1000 samples per second (1 kHz). In comparison, the maximum rotational speed tested was 30 Hz (1800 rpm). The rotational speed was measured using two separate methods: 1) laser tachometer and 2) Hall-effect switch. The laser tachometer provided a resolution of ± 1 rpm and was used as the primary method of measurement. The Hall-effect switch had a lower resolution of ± 30 rpm, and its measurements were mainly used within the data acquisition program to organize the force measurement data.

3.2.4 Experimental Test Matrix and Testing Procedures

The experimental test matrix for the wind tunnel studies is provided in Table 3.2. In the first set of experiments (Table 3.2a), the rotor operated with symmetric pitching kinematics, where the blade experiences similar pitch angles in opposing halves of the circular trajectory. A total of five pitch amplitudes (θ_A) were tested in the range of 25° to 50°. For each pitch amplitude, multiple pitch phase angles (ϕ) were tested in the range of 30° to 110°, and the rotational speed (Ω) was varied from 600 to 1800 rpm in increments of 200 rpm. The minimum and maximum freestream velocities (U_∞) tested were 3 and 13 m/s.

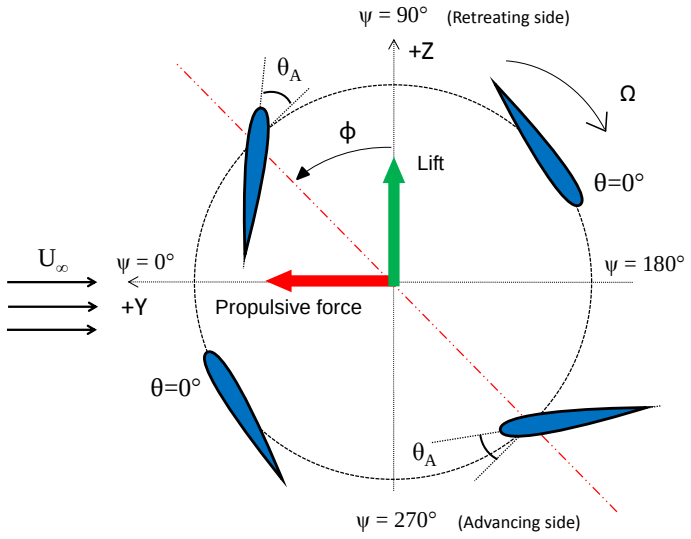

Figure 3.3: Cyclorotor coordinate system.

In the second set of experiments (Table 3.2b), the cyclorotor operated with asymmetric pitching kinematics, where the blade experiences larger pitch angles in one half of the circular trajectory with respect to the other half. In these tests, the total peak-to-peak pitch amplitude was maintained constant at 70°, and a total of

Table 3.2a: Test matrix 1 (symmetric pitching).

Pitch amplitude (θ_A) [deg]	Pitch phase angle (ϕ) [deg]	Freestream velocity (U_∞) [m/s]	Rotational speed (Ω) [rpm]
25	30, 50, 70, 80, 110	3–9	600–1800
30	30, 50, 70, 80, 90	3–9	600–1800
40	30, 50, 70, 80, 90, 100, 110	3–11	600–1800
45	30, 50, 70, 80, 90, 100	3–13	600–1800
50	30, 50, 70, 80, 90, 100, 110	7–13	800–1800

Table 3.2b: Test matrix 2 (asymmetric pitching).

Mean pitch angle (θ_M) [deg]	Pitch phase angle (ϕ) [deg]	Freestream velocity (U_∞) [m/s]	Rotational speed (Ω) [rpm]
-5, 0, 5, 10 ($\theta_{pk\,to\,pk} = 70$)	30, 50, 70, 80, 90, 100, 110	3–9	600–1800

four mean pitch angle (θ_M) were tested in the range of $-5°$ to $10°$. Multiple phase angles were tested in the range of $30°$ to $110°$. The rotational speed was varied from 600 to 1800 rpm and the freestream velocities tested were in the range of 3 to 9 m/s.

Each experiment was carried out at least three times to ensure sufficient repeatability. All measurements in the current Chapter represent the averaged values between three test runs. Tare tests were conducted after removing the blades to measure the parasitic drag and power of the rotor structure (i.e. end-plates, linkages, etc.). The tare measurements were removed from the total measurements of power and propulsive force. Therefore, in the results throughout the current Chapter, the power only includes the induced and profile contributions of the blades, and the propulsive force represents the net aerodynamic force produced by the blades along the freestream direction (Y-axis).

3.3 Results and Discussion

3.3.1 Performance Measurements: Fixed Control Inputs

The effects of blade kinematics on cyclorotor aerodynamic performance was investigated through systematic parametric studies. The three blade parameters varied were: 1) blade pitch amplitude (θ_A), 2) pitch phase angle (ϕ) and mean pitch angle (θ_M). The effect of each blade parameter on cyclorotor lift, propulsive force and power was examined at different advance ratios. The results from these studies will now be discussed.

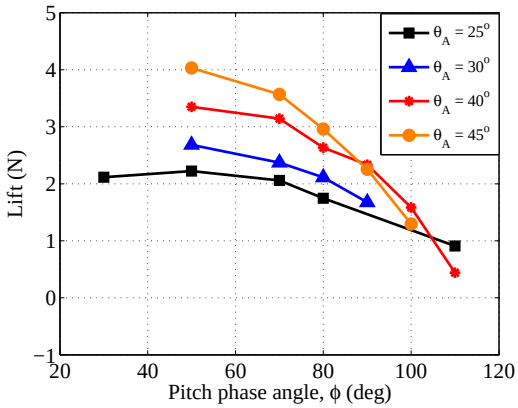

(a) Lift variation.

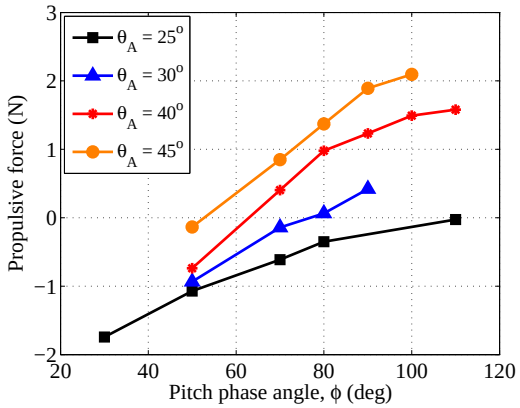

(b) Propulsive force variation.

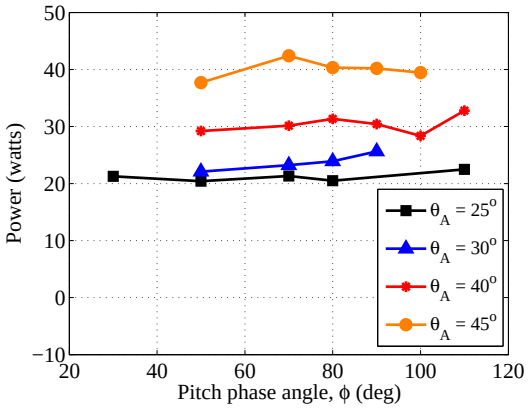

(c) Power variation.

Figure 3.4: Lift, propulsive force and power versus pitch phase angle for different pitch amplitudes at advance ratio 0.49 (Ω=1800 rpm, U_∞=7 m/s).

3.3.1.1 Effect of Pitch Phase Angle

The phasing of cyclic blade pitching (pitch phase angle, ϕ) plays a significant role in the aerodynamics of the cyclorotor in forward flight. By varying the phase angle, the contributions of rotor forces to lift and propulsive force can be changed. In the present section, the effects of phase angle on rotor performance will be examined at

a moderate advance ratio ($\mu = 0.49$) and a high advance ratio ($\mu = 1.13$).

Figure 3.4 shows the variations in lift, propulsive force and power with pitch phase angle for different pitch amplitudes at an advance ratio of 0.49. The rotational speed of the rotor is 1800 rpm ($\Omega R = 14.36$ m/s) and the forward speed is 7 m/s. Figure 3.4a shows that the effect of increasing the phase angle is to decrease lift for a given pitch amplitude. Also, the rate of decrease in lift is greater at larger pitch amplitudes. For example, at a constant phase angle of 100°, the rotor produces a larger lift value at a pitch amplitude of 40° compared to a pitch amplitude of 45°.

Figures 3.4b and 3.4c show the variations in propulsive force and power with pitch phase angle for the same advance ratio ($\mu = 0.49$). For a given pitch amplitude, increasing the phase angle leads to increasing values of propulsive force (Fig. 3.4b). Figure 3.4c shows that the power remains relatively constant with variations in phase angle for all the pitch amplitudes tested.

Figure 3.5 shows the variations in lift, propulsive force and power with pitch phase angle at a high advance ratio of 1.13. Here, the rotational speed is 1000 rpm ($\Omega R = 7.98$ m/s) and the forward speed is 9 m/s. Based on the results in Fig. 3.5a, the effects of phase angle on lift are similar to those previously observed for the lower advance ratio case.

Figures 3.5b and 3.5c show the variations in propulsive force and power at an advance ratio of 1.13. As shown in Fig. 3.5b, the propulsive force does not continue to increase with phase angle at large pitch amplitudes. For example, at a pitch amplitude of 40°, propulsive force increases linearly up to a phase angle of about 80°, beyond which the trend then becomes non-linear and the propulsive

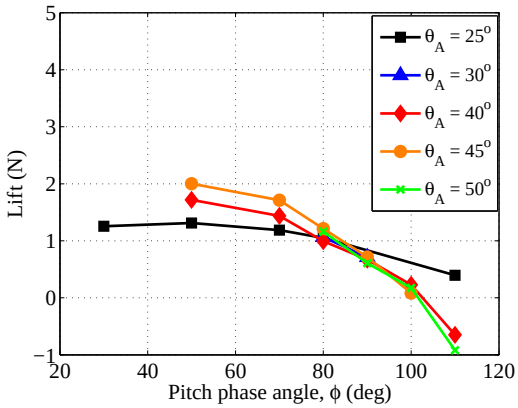

(a) Lift variation.

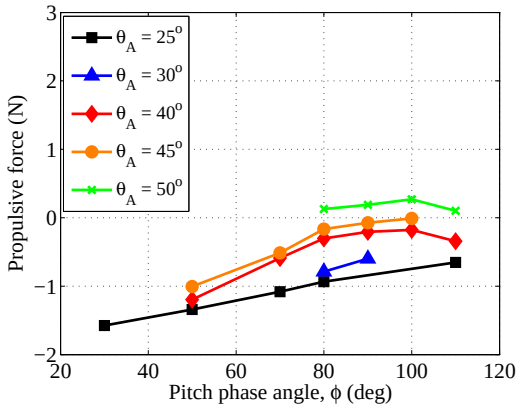

(b) Propulsive force variation.

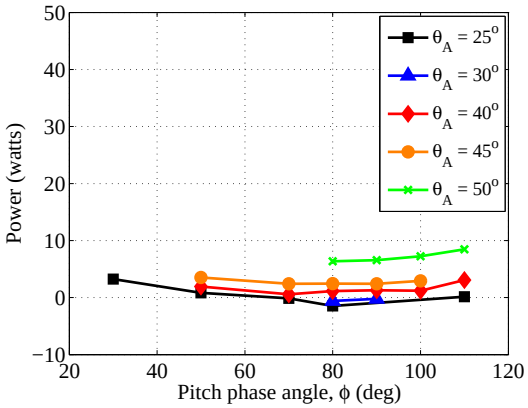

(c) Power variation.

Figure 3.5: Lift, propulsive force and power versus pitch phase angle for different pitch amplitudes at advance ratio 1.13 (Ω=1000 rpm, U_∞=9 m/s).

force begins to decrease. Figure 3.5c shows that power no longer remains constant at the lowest and highest pitch amplitudes tested. At a pitch amplitude of 25°, the power increases below a phase angle of 80°. At a pitch amplitude of 50°, the power increases with increasing phase angle. Furthermore, the relatively low power values at this advance ratio compared to the lower advance ratio case indicate that the rotor is operating close to a wind-mill state, where the rotor extracts energy from

the flow as opposed to adding energy to the flow. This wind-mill state is especially evident for pitch amplitudes of 25° and 30° where the power values are close to zero. The low power values are the result of the low rotational speed of the rotor compared to the high speed of the incoming flow (i.e. high advance ratio).

The effects of pitch phase angle on cyclorotor performance can be summarized as follows. At low to moderate advance ratios, the phase angle may be varied over a relatively wide range (40°–110°) to vary the rotor force contributions to lift and propulsive force, without significantly impacting power consumption. At high advance ratios, the range in which the phase angle can be varied to change the lift and propulsive force components is more limited (40°–90°). Figure 3.5 showed that operating at phase angles outside of these ranges adversely affects propulsive force and/or increases power consumption. In summary, the pitch phase angle is a key control parameter that can be used in a cyclocopter MAV to achieve straight and level flight, as well as acceleration/deceleration and climb/descent maneuvers, with a relatively minimal impact on rotor power.

3.3.1.2 Effect of Blade Pitch Amplitude

The blade pitch amplitude (θ_A) is also an effective control parameter for varying the lift and propulsive force and plays a strong role in rotor propulsive efficiency. In this section, the effects of blade pitch amplitude will be examined at a moderate advance ratio ($\mu = 0.49$) and a high advance ratio ($\mu = 1.13$).

Figure 3.6 shows the variations in lift, propulsive force and power with pitch

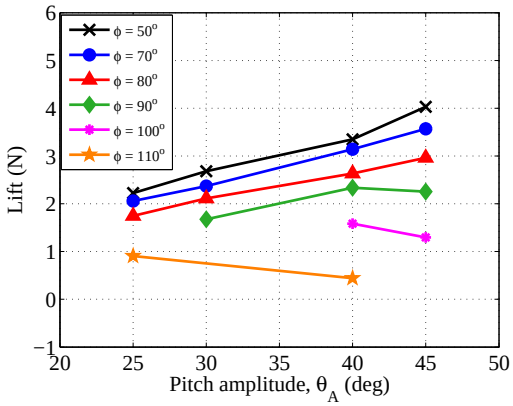

(a) Lift variation.

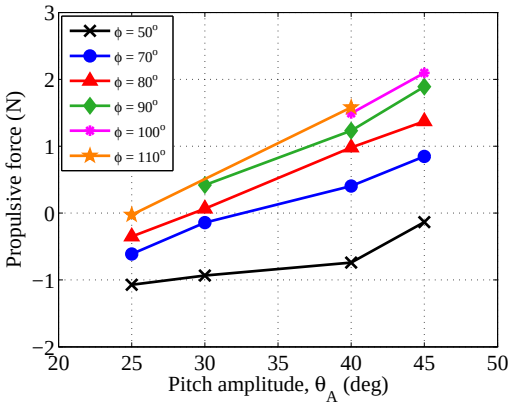

(b) Propulsive force variation.

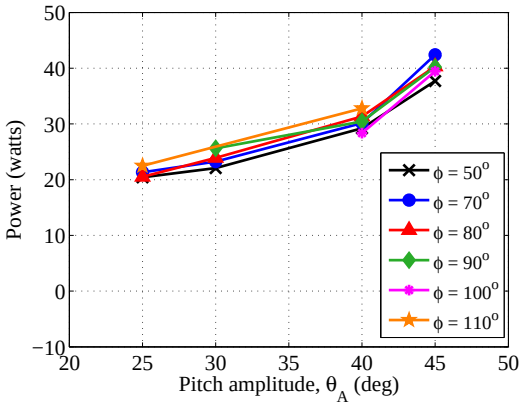

(c) Power variation.

Figure 3.6: Lift, propulsive force and power versus blade pitch amplitude for different phase angles at advance ratio 0.49 (Ω=1800 rpm, U_∞=7 m/s).

amplitude for different phase angles at an advance ratio of 0.49. Figure 3.6a shows that increasing the pitch amplitude increases lift for phase angles up to 90° and decreases lift for phase angles greater than 90°. Figure 3.6b shows the variation in propulsive force with pitch amplitude. For a given phase angle, the propulsive force increases linearly with increasing pitch amplitude. Figure 3.6c shows that power increases with increasing pitch amplitude. The rate of increase in power is greater

for a pitch amplitude larger than 40°, indicating that the blades may be close to stall. These various trends remained the same for low to moderate advance ratios ($\mu < 0.8$).

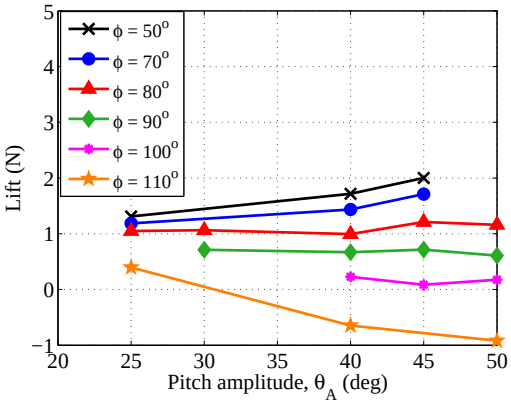

(a) Lift variation.

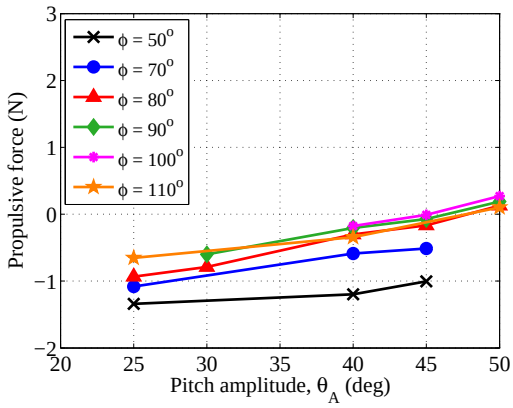

(b) Propulsive force variation.

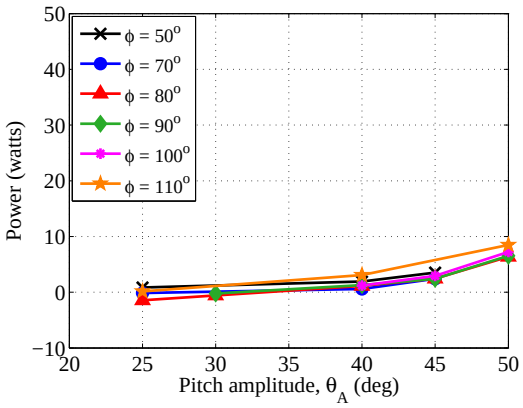

(c) Power variation.

Figure 3.7: Lift, propulsive force and power versus blade pitch amplitude for different phase angles at advance ratio 1.13 (Ω=1000 rpm, U_∞=9 m/s).

Figure 3.7 shows the variations in lift, propulsive force and power with pitch amplitude for various phase angles at a high advance ratio of 1.13. Compared to the lower advance ratio case, Fig. 3.7a shows that the lift is significantly less

sensitive to variations in pitch amplitude at this higher advance ratio. For example, at a constant phase angle of 50°, increasing the pitch amplitude from 25° to 45° at advance ratio 1.13 leads to a 53% increase (1.3 N to 2 N) in lift (Fig. 3.7a). However, for the same case at the lower advance ratio of 0.49, the lift increases by 81% (2.2 N to 4.0 N). The results in Fig. 3.7a suggest that pitch amplitude may not be an effective control parameter for varying the lift component of the cyclorotor at high advance ratios, especially when the operating phase angle is high ($\phi > 80°$). This will be important when considering straight and level flight at high forward speeds, where the rotor may need to operate at relatively large phase angles to maintain the necessary propulsive force.

Figures 3.7b and 3.7c show the variations in propulsive force and power with pitch amplitude at advance ratio 1.13. The propulsive force is shown to increase linearly with increasing pitch amplitude (Fig. 3.7b). The variation in power with pitch amplitude is similar to the low advance ratio case, and the low power values can be attributed to the rotor operating near a wind-mill state as discussed previously.

In summary, the blade pitch amplitude is shown to be an effective parameter for varying lift and propulsive force at lower advance ratios. However, at high advance ratios, the pitch amplitude must be primarily used to vary the propulsive force component. Furthermore, unlike the pitch phase angle, the blade pitch amplitude significantly impacts rotor power consumption and therefore plays a key role in the overall efficiency of the rotor.

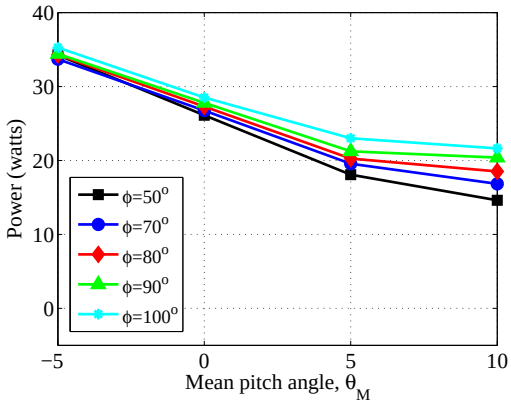

(a) Lift variation.

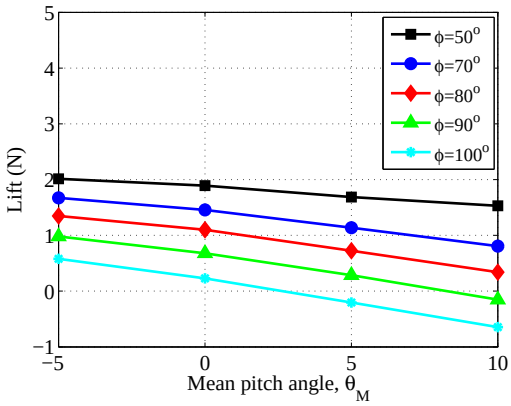

(b) Propulsive force variation.

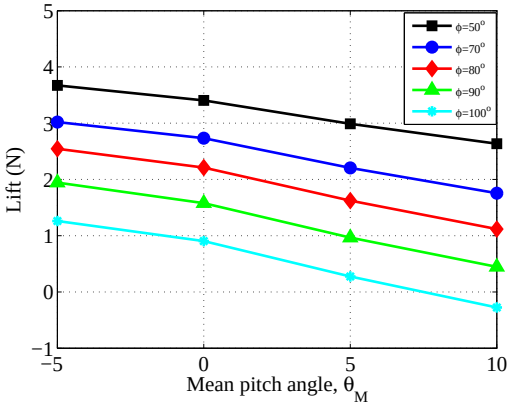

(c) Power variation.

Figure 3.8: Lift, propulsive force and power versus mean pitch angle for different phase angles at advance ratio 0.49 (Ω=1800 rpm, U_∞=7 m/s).

3.3.1.3 Effect of Mean Pitch Angle

Another important blade parameter is the mean pitch angle (θ_M). As illustrated in Chapter 2, a non-zero mean pitch angle introduces an asymmetry in the blade pitching kinematics. The mean pitch angle can have an important impact on cyclorotor aerodynamic performance, and previous studies in hover showed that asymmetric

pitching kinematics improved the cyclorotor power loading (thrust per unit power) for the same disk loading (thrust per unit area) compared to symmetric pitching kinematics [14]. The current section investigates the effects of mean pitch angle on cyclorotor aerodynamic performance at two advance ratios.

Figure 3.8 shows the rotor lift, propulsive force and power as a function of mean pitch angle at advance ratio of 0.49. Recall that a mean pitch angle of 0° corresponds to symmetric pitching kinematics, which forms the baseline case. Figure 3.8a shows that increasing the mean pitch angle leads to an approximately linear decrease in lift. The rate of decrease in lift is the same for all the phase angles tested. Furthermore, Fig. 3.8b shows that the propulsive force is less sensitive to variations in mean pitch angle compared to lift (Fig. 3.8b).

Figure 3.8c shows that increasing the mean pitch angle leads to decreasing values of power. Comparing Figs. 3.8a and 3.8c, it can be seen that the rate of decrease in power is greater than the corresponding rate of decrease in lift. This implies that it may be more power efficient to operate at higher mean pitch angles, although the obvious trade-off is the decreased lift production.

Figure 3.9 shows the variations in lift, propulsive force and power with mean pitch angle at a high advance ratio of 1.13. The results in Figs. 3.9a and 3.9b show that the effects of mean pitch angle on lift and propulsive force are similar to those observed for the lower advance ratio case.

Figure 3.9c shows the variation in power with mean pitch angle at advance ratio 1.13. Unlike the lower advance ratio case, the power remains relatively constant with increasing mean pitch angle. In fact, the power slightly increases with mean

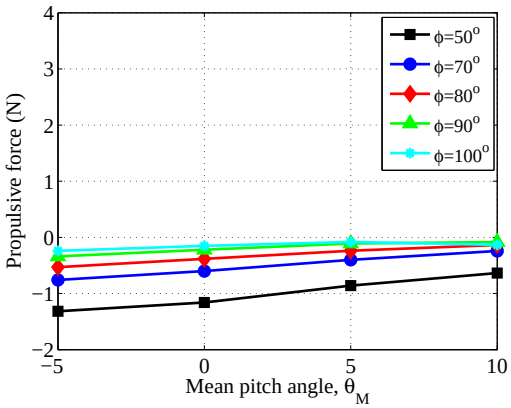

(a) Lift variation.

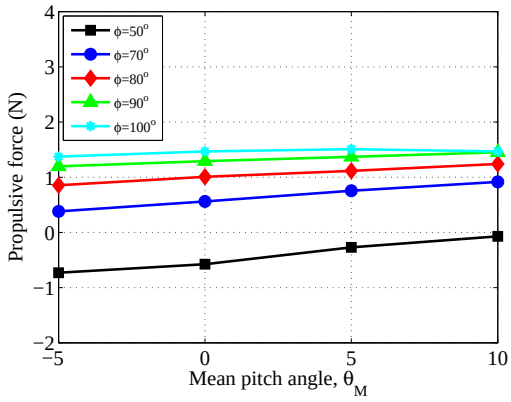

(b) Propulsive force variation.

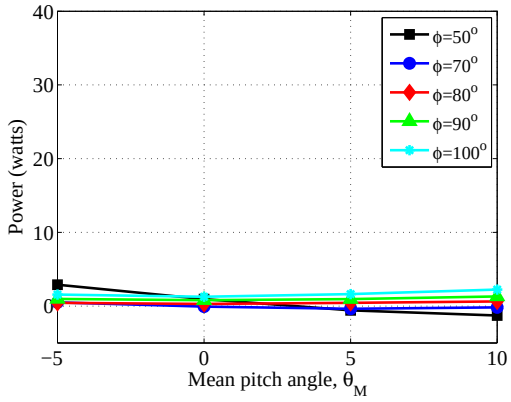

(c) Power variation.

Figure 3.9: Lift, propulsive force and power versus mean pitch angle for different phase angles at advance ratio 1.13 (Ω=1000 rpm, U_∞=9 m/s).

pitch angle at a phase angle of 100°.

Based on Figs. 3.8 and 3.9, the effects of mean pitch angle can be summarized as follows. The mean pitch angle can be used effectively to vary the rotor lift, although the propulsive force is relatively less sensitive. At low to moderate advance ratios, operating at positive values of mean pitch angle may improve the power efficiency of the cyclorotor. However, this benefit may be lost at extremely large

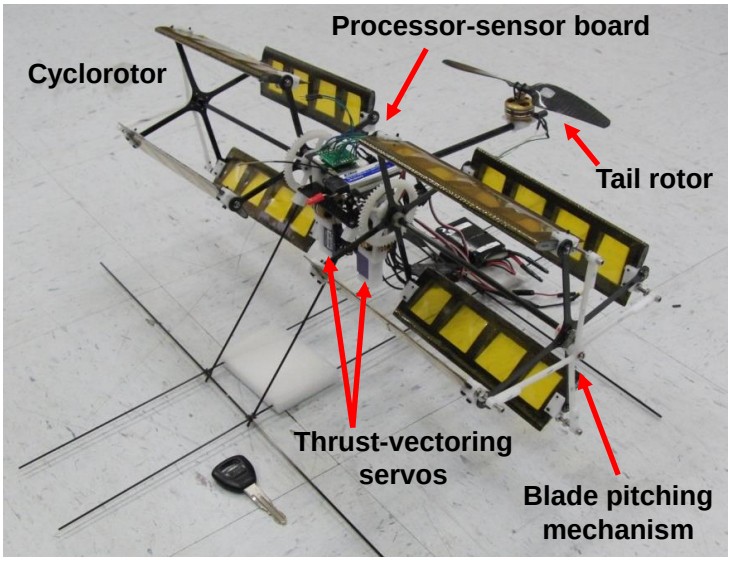

Figure 3.10: Twin-cyclocopter micro air vehicle.

mean pitch angles, where the blades may stall in the azimuthal regions of high pitch amplitude.

3.3.2 Rotor Performance in Trimmed, Level Flight

Using the results from the parametric studies, performance requirements for the isolated cyclorotor in straight and level flight were determined through interpolation. In the interpolation process, the blade pitch amplitude (θ_A) and pitch phase angle (ϕ) were used as the two primary variables to trim the rotor lift and propulsive force at a given forward speed. The rotational speed (Ω) of the rotor was held constant. The baseline lift value was derived based on a 500 g twin cyclocopter MAV, shown in Fig. 3.10. The cyclorotors on this vehicle are assumed to produce approximately 80% of the total required lift in forward flight; thus, the baseline lift value is 200 g (1.96 N) for each cyclorotor.

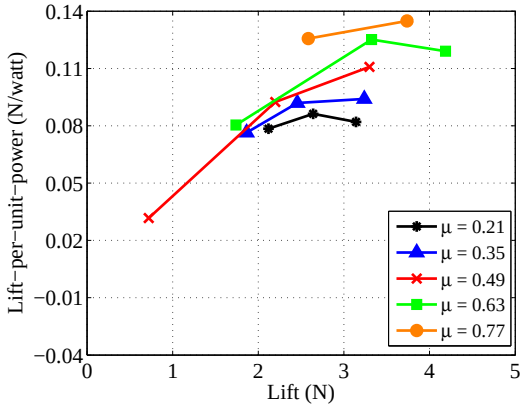

Figure 3.11: Lift production efficiency at different advance ratios (propulsive force=0 N).

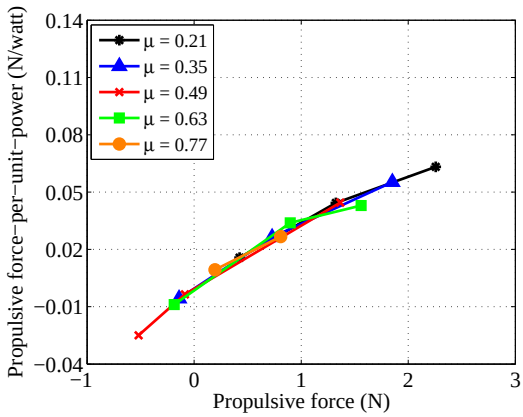

Figure 3.12: Propulsive force production efficiency at different advance ratios (lift=1.96 N).

The current section will be organized as follows. First, the lift and propulsive force producing efficiency of the cyclorotor will be examined at different advance ratios. Next, the effects of varying lift, propulsive force and rotational speed on rotor power, lift-to-drag ratio, and control input angles (pitch amplitude and phase angle) will be shown as a function of forward speed. The effect of asymmetric pitching kinematics on power requirements will also be presented. Lastly, the maximum forward speed tested for the cyclorotor along with the corresponding power requirements will be presented.

3.3.2.1 Lift and Propulsive Force Production Efficiency

Figure 3.11 shows lift per unit power as a function of lift at different advance ratios. These results are for a constant propulsive force value of 0 N. The lift per unit power of the cyclorotor improves with both increasing advance ratio (at constant lift) and

increasing values of lift (at constant advance ratio). These results suggest that the power penalty associated with higher values of lift (i.e. increased payload, in-flight climb maneuvers) is lower at high forward speeds compared to hover and low-speed flight.

Figure 3.12 shows propulsive force per unit power as a function of propulsive force at different advance ratios. These results are for a constant lift value of 1.96 N; thus, the rotor operates in level flight at each advance ratio. For a constant advance ratio, the propulsive force per unit power increases with increasing values of propulsive force, but remains relatively constant with increasing advance ratio.

3.3.2.2 Effect of Varying Lift

Examining the effects of varying lift values on cyclorotor performance can be important for determining the payload capacity and the ability to perform vertical climb/descent maneuvers in forward flight. Figure 3.13 show the variations in power, lift-to-drag ratio, and control input angles as a function of forward speed for different values of lift. Each point in Figs. 3.13a–3.13c corresponds to a trimmed flight condition, where the lift and propulsive force values are constant at 1.96 N and 0 N, respectively, and the rotational speed is held constant at 1800 rpm. Recall that the power measurements are for the isolated cyclorotor and, therefore, only include the induced and profile power contributions of the blades. In the effective lift-to-drag-ratio calculations, the drag was determined by [11]:

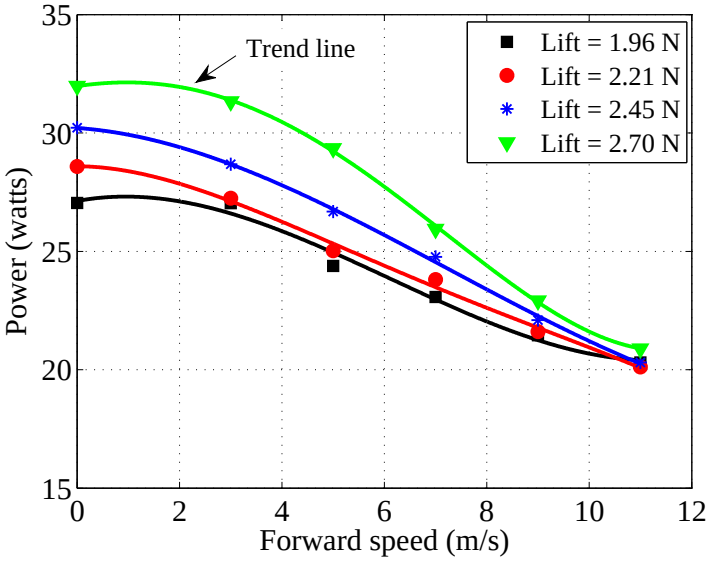

(a) Power variation.

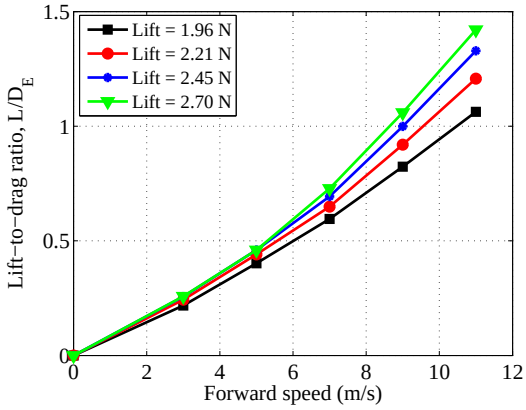

(b) Equivalent lift to drag ratio variation.

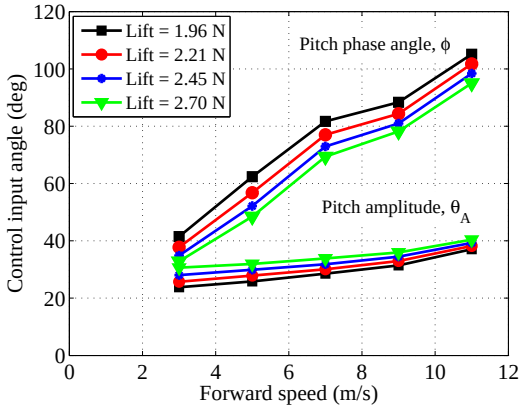

(c) Control input angle variation.

Figure 3.13: Power, lift-to-drag ratio and control input requirements as a function of forward speed for varying values of lift (propulsive force=0 N, Ω=1800 rpm).

$$EquivalentDrag = \frac{Power}{U_\infty} \tag{3.1}$$

Figure 3.13a shows the variation in power with forward speed for lift values of 1.96, 2.21, 2.45 and 2.70 N. For a constant value of lift, the rotor power decreases with increasing forward speed. This is primarily due to the decreased contribution of induced power to the total power as the forward speed increases, similar to a conventional edgewise rotor.

Furthermore, Fig. 3.13a also shows that for a constant forward speed, the rotor power increases with increasing values of lift. The relative differences in power between different values of lift diminish as the rotor approaches higher forward speeds. For example, the difference in power between lift values of 1.96 N and 2.70 N is approximately 16% at a speed of 3 m/s, but only 3% at a speed of 11 m/s. These results are consistent with the observations made in regard to the improved lift producing efficiency of the cyclorotor at high forward speeds. These trends may not necessarily occur at forward speeds greater than 11 m/s, where the advance ratio approaches unity. This is because the increase in profile power contribution to the total power can be expected to dominate the decrease in induced power contribution. The power curve corresponding to each value of lift in Fig. 3.13a can be expected to reach a minimum value and then increase with increasing forward speed.

Figure 3.13b shows the rotor effective lift-to-drag ratio as a function of forward speed for the cases considered in Fig. 3.13a. For a given lift value, the lift-to-drag ratio improves with increasing forward speed. Also, for a given forward speed, the

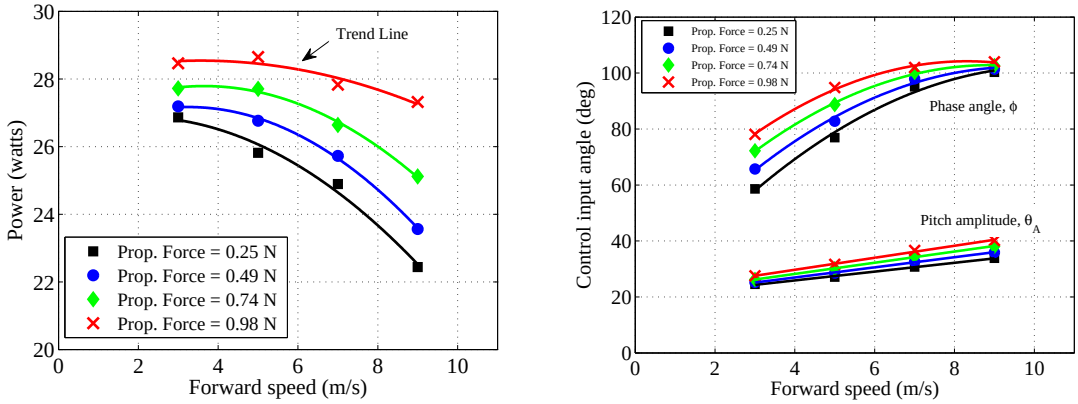

(a) Power variation.

(b) Control input angle variation.

Figure 3.14: Power and control input requirements as a function of forward speed for varying values of propulsive force (lift=1.96 N, Ω=1800 rpm).

lift-to-drag ratio increases with increasing lift values and the relative differences become greater at higher forward speeds. These results agree with those presented in Fig. 3.13a.

Figure 3.13c shows the required blade pitch amplitude and phase angle control inputs for maintaining the straight and level flight conditions in Fig. 3.13a. For a constant value of lift, both pitch amplitude and pitch phase angle must be simultaneously increased with increasing forward speed. Furthermore, for a given forward speed, the rotor must operate with higher pitch amplitudes and lower phase angles for increasing values lift.

3.3.2.3 Effect of Varying Propulsive Force

The results in Fig. 3.13 were for a constant propulsive force of 0 N. It is also important to consider cyclorotor performance at non-zero values of propulsive force

to account for the additional drag of the fuselage and rotor structure. Figure 3.14 shows the power and control input angles as a function of forward speed for varying propulsive force values of 0.25, 0.49, 0.74 and 0.98 N. The lift is constant at 1.96 N and the rotational speed is 1800 rpm.

Figure 3.14a shows that for a constant propulsive force, the rotor power decreases with increasing forward speed, as observed in the previous section. Furthermore, at a given forward speed, the rotor power consumption is higher for larger values of propulsive force. From Fig. 3.14b, we see that both pitch amplitude and phase angle must be increased to maintain straight and level flight at higher values of propulsive force at a given forward speed. The differences in phase angle for maintaining different values of propulsive force decrease with increasing forward speeds, while the corresponding differences in pitch amplitude become larger. This is because as the cyclorotor approaches high forward speeds and high operating phase angles, the propulsive force becomes a stronger function of pitch amplitude than phase angle, as illustrated in previous sections.

3.3.2.4 Effect of Rotational Speed

In addition to considering varying values of lift and propulsive force, the effects of rotational speed on cyclorotor performance must also be examined since the profile power contribution depends strongly on the rotational speed (cube of rpm). Moreover, previous studies on conventional edgewise rotors have shown that the relative contribution of profile power to the total power can be significantly greater at the

MAV-scale as compared to full-scales [12]. Therefore, operating at a low rotational speed may be beneficial in terms of rotor power consumption. Furthermore, operating at lower rotational speeds can also be advantageous from the point of view of vehicle structural design, since a lower rotational speed leads to decreased centrifugal forces on the blades and thereby reduces the structural loads on the rotor structure.

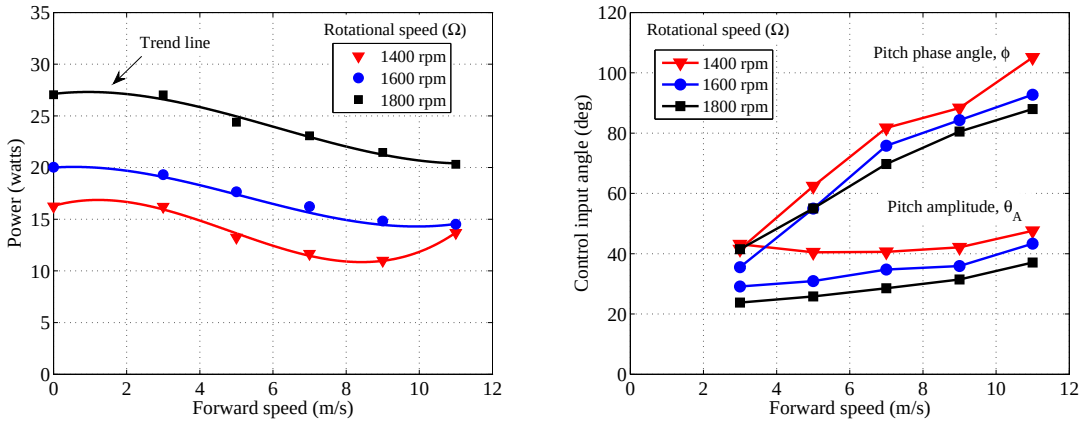

(a) Power variation.

(b) Control input angle variation.

Figure 3.15: Power and control input requirements as a function of forward speed for varying values of rotational speed (lift=1.96 N, propulsive force=0 N).

Figure 3.15a shows the variation in power with forward speed for rotational speeds of 1400, 1600 and 1800 rpm, which correspond to blade translation speeds of 11.17, 12.17 and 14.36 m/s, respectively. For all cases, the rotor lift and propulsive force were constant at 1.96 N and 0 N. From Fig. 3.15a, we see that reducing the operating rotational speed from 1800 rpm to 1400 rpm leads to significant reductions in power consumption for a given forward speed. Also, for a constant rotational

speed of 1400 rpm, the rotor power begins to increase at forward speeds greater than 9 m/s. The corresponding control input requirements are presented in Fig. 3.15b. At a given forward speed, both pitch amplitude and phase angle must be increased to maintain straight and level flight at decreasing rotational speeds.

The results in Figs. 3.15a and 3.15b are explained as follows. When the rotational speed of the rotor is reduced, there is a corresponding decrease in the aerodynamic forces produced by the rotor. The blade pitch amplitude and pitch phase angle must both be increased (Fig. 3.15b) to compensate for the decreased lift and propulsive force to maintain straight and level flight. However, the rotor profile power is a stronger function of rotational speed (cube of rpm) than pitch amplitude (below stall). Thus, when the rotor operates at a lower rotational speed, the decreases in profile power outweigh the corresponding increases resulting from increased pitch amplitude. The net result is a decrease in the total power consumption at a given forward speed, as observed in Fig. 3.15a. However, further decreases in rotational speed will eventually be limited by the onset of blade stall.

Figure 3.15a also showed that for the 1400 rpm case, the power reaches a minimum value at a speed of about 9 m/s and then begins to increase at a higher forward speed. The increase in power indicates that the blades may be close to stall, because of the relatively high pitch amplitude (θ_A=45°) required at this low rotational speed (Fig. 3.15b). Therefore, the profile power benefits gained from operating at a lower rotational speed are no longer realized.

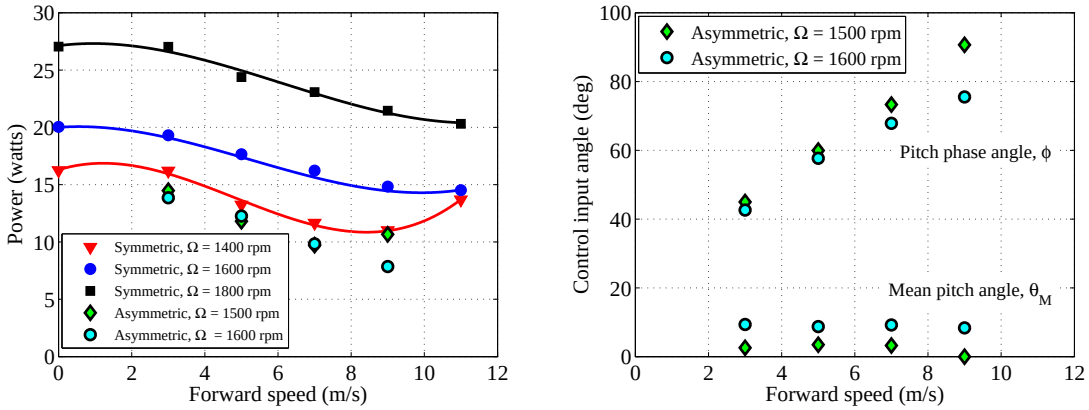

(a) Power variation.

(b) Control input angle variation.

Figure 3.16: Power and control input requirements as a function of forward speed for asymmetric pitching kinematics (lift=1.96 N, propulsive force=0 N).

3.3.2.5 Symmetric vs. Asymmetric Pitching

The impact of asymmetric pitching kinematics on cyclorotor trimmed, level flight performance was investigated and compared to the case of symmetric pitching kinematics. In the interpolation process, the mean pitch angle (θ_M) and phase angle (ϕ) were used as the two control variables (i.e. instead of pitch amplitude and phase angle), and the blade peak-to-peak pitch amplitude and rotational speed were held constant.

Figure 3.16 shows the power and control input angle variations as a function of forward speed. Note that in Fig. 3.16a, the power values for symmetric pitching kinematics from the previous section are re-presented for comparison purposes only. The lift and propulsive force values are constant at 1.96 N and 0 N, respectively.

Comparing the power consumption between symmetric and asymmetric pitch-

ing cases (Fig. 3.16a), it can be seen that asymmetric pitching kinematics can lead to lower values of power consumption at a given forward speed. This is especially evident when the power is compared at the same rotational speed. At a constant rotational speed of 1600 rpm, the power consumption for the asymmetric pitching case is 28% and 47% lower than the symmetric pitching case at forward speeds of 3 m/s and 9 m/s, respectively. Figure 3.16b shows the corresponding control input requirements. As the rotor approaches increasing forward speeds, the phase angle must be increased (to produce the necessary propulsive force) and the mean pitch angle must be slightly decreased (to maintain the necessary lift). Therefore, the results in Fig. 3.16 are promising, as they show that asymmetric pitching kinematics can help improve cyclorotor performance in forward flight.

3.3.2.6 High Speed Flight Capability

The maximum forward speed tested for the cyclorotor while maintaining straight and level flight was 13 m/s. The rotor operated at 1740 rpm ($\Omega R = 13.88$ m/s), corresponding to an advance ratio of 0.94. The rotor was able to maintain a lift value of 2.82 N, which exceeds the requirement for the baseline case of 1.96 N, and the propulsive force was 0 N. The effective lift-to-drag ratio was 1.73. Figure 3.17 shows the variation in power with forward speed for this particular case. The power consumption of the rotor decreases with increasing forward speed, as observed in previous sections, and the rotor power at 13 m/s was 36% lower compared to the hover condition. The result in Fig. 3.17 is promising, showing the cyclorotor to be

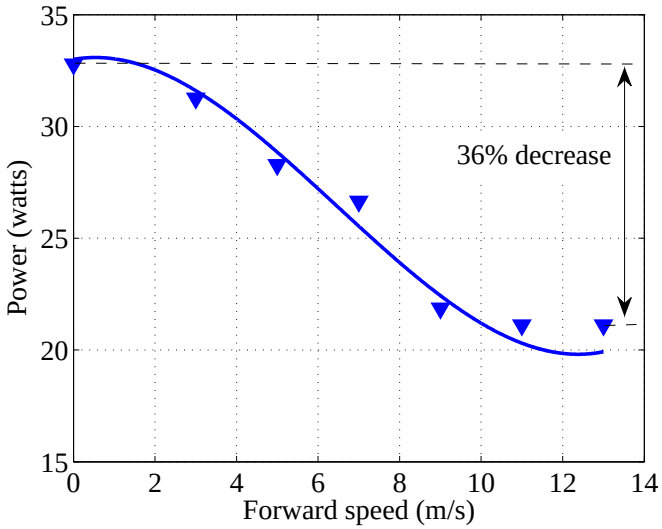

Figure 3.17: Power versus forward speed showing maximum forward speed tested (lift=2.82 N, propulsive force=0 N, and Ω=1740 rpm).

capable of operating efficiently at high forward speeds, while maintaining sufficient lift that would be required by the twin-cyclocopter MAV (Fig. 3.10). The absolute maximum forward speed for the cyclocopter MAV will depend on the total amount of power available on-board and also on the parasitic power of the vehicle fuselage and rotor structure.

3.4 Summary

The forward flight performance of a MAV-scale cyclorotor has been explored through systematic wind tunnel studies. The effects of blade pitch amplitude (θ_A), pitch phase angle (ϕ) and mean pitch angle (θ_M) on rotor lift, propulsive force and power were investigated at different advance ratios. Using these results, performance requirements for the cyclorotor in straight and level flight were determined. The lift

and propulsive force producing efficiency, power, lift-to-drag ratio, and control input requirements were determined at various forward speeds and the effects of varying lift and rotational speed were examined. Also, the power at the maximum forward speed tested was presented.

These results can provide an important framework for the development of a suitable control strategy for the twin-cyclocopter MAV (Fig. 3.10) and also for improving its forward flight performance. However, the findings can also be used to aid the design and development of other cyclocopter MAVs in the future.

Chapter 4: Flow Field Studies

4.1 Overview

The results presented in Chapter 3 primarily focused on time-averaged force measurements. Although these studies provided a well-rounded understanding about the effects of blade kinematics in forward flight and rotor performance in straight and level flight, they do not provide insights into the flow physics behind cyclorotor force production. Therefore, a key objective of the current research was to examine the flow physics of the cyclorotor using flow visualization and particle image velocimetry (PIV) techniques. The current chapter provides a discussion of these flow field studies.

A 2-bladed cyclorotor was tested in a closed-section wind tunnel. A high-speed camera/laser setup allowed for flow visualization and time-resolved, planar PIV measurements. The two dimensional flow field at the mid-span of the cyclorotor was analyzed at different advance ratios. Both time-averaged and phase-averaged flow fields were examined. The time-averaged flow field revealed key insights into the major force production regions along the cyclorotor azimuth. The phase-averaged flow field provided insights into the role of unsteady aerodynamics on rotor force production, particularly blade wake interactions in the lower-aft azimuthal region

of the cyclorotor. The results from the PIV studies were correlated with experimental force measurements as well as CFD-predicted instantaneous blade forces from previous studies. The results in the current Chapter constitute the first known flow field studies on a cyclorotor in forward flight, and aim to provide a fundamental understanding of the flow physics of the cyclorotor.

4.2 Experimental Apparatus and Procedure

4.2.1 Experimental Cyclorotor

The two-bladed cyclorotor designed and built for the PIV experiments is shown in Fig. 4.1a. The rotor employs a unique cantilever design, with the blade pitching mechanism located at the root. The key design constraints for the rotor included a high rotational speed of 1200 rpm, and limited blade radial deflections at this rotational speed. The cantilever design was important as it provided an unobstructed span-wise view for the high speed camera. Two blades were chosen as it is the simplest model of a cyclorotor. Although increasing the number of blades would introduce additional aerodynamic interactions, the general operating principles of the rotor are expected to remain the same. Apart from the number of blades, the remaining rotor dimensions of blade span, blade chord length, rotor radius and airfoil section were the same as the values listed in Table 3.1. Although a two-bladed design provided a simpler case for examining the flow field, it also led to increased vibration levels compared to a rotor with a larger number of blades. Therefore, an important aspect of the design process involved careful balancing of the rotor.

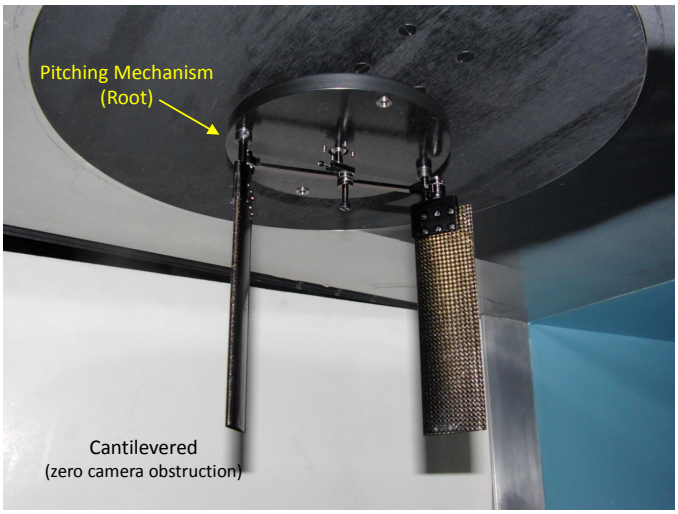

(a) 2-bladed cyclorotor.

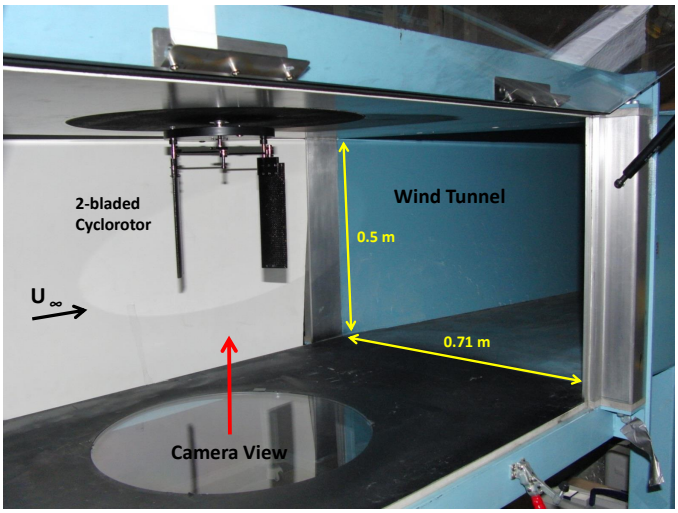

(b) Cyclorotor vertically mounted in test section.

Figure 4.1: Closed-section wind tunnel setup for flow visualization and PIV experiments.

4.2.2 PIV Setup

4.2.2.1 Wind Tunnel Setup

The PIV experiments were conducted in an open-circuit/closed-section wind tunnel with test section dimensions of 0.5 m×0.71 m and a maximum speed of 45 m/s. The cyclorotor was mounted vertically in the tunnel test section, as shown in Fig. 4.1b. The flow was seeded with vaporized mineral oil at the inlet of the wind tunnel. A high-speed, double-pulsed laser illuminated the seeding particles (Litron LDY304 Nd:YLF laser, 30 mJ/pulse at 1 kHz rep-rate). The laser sheet was positioned at the mid-span of the rotor to minimize the presence of three-dimensional tip effects. A square mirror (0.2 m×0.2 m) was used to redirect a portion of the laser sheet back toward the rotor to reduce the shadows cast by the blades. A high-speed camera (Phantom V311, 1MPx, 3,250 fps) was positioned below the test section and oriented upward to view the blades through a circular acrylic window. The camera view angle is shown in Fig. 4.1b.

All PIV experiments were conducted with the rotor at 1200 rpm (blade translation speed of 9.58 m/s). Three different freestream velocities were tested U_∞ = 3, 5 and 7 m/s, which correspond to advance ratios of μ = 0.31, 0.52 and 0.63. Freestream velocities were determined using PIV measurements of the mean flow in the test section (without the rotor present). Furthermore, all the studies were performed with the cyclorotor operating at a phase angle (ϕ) of 90°, which was shown in Chapter 3 to be representative of a high-speed flight configuration. Recall that

at a phase angle of 90°, the blade achieves a maximum pitch angle at the front (ψ = 0°) and aft (ψ = 180°) points of its trajectory (see Fig. 2.1 for reference).

4.2.2.2 PIV Processing

Image pairs were acquired at a sampling rate of 1.6 kHz. The rotor operated at 1200 rpm (20 Hz), resulting in data sets with measurements at 80 rotor azimuthal positions per rotor revolution (i.e. azimuthal resolution of 4.5°). All PIV acquisition and processing was performed using DaVis v8.1.3 by LaVision. Raw images were pre-processed using a spatial background subtraction filter to increase the signal-to-noise ratio (image contrast). Regions where the velocity field was undefined (i.e. blades, shadows and areas of low seeding) were excluded (i.e. masked) from processing. The maximum particle displacement between the two frames of each image pair was approximately 4–7 pixels. A multi-pass cross-correlation algorithm was performed with one pass of a 64×64 pixel window and two passes of a 32×32 pixel window; each pass implemented a 50% window overlap. Circular windows were used to eliminate the bias effects encountered along the diagonals of traditional square windows. The resulting spatial vector field provided a grid of 81×51 vectors (in the Y×Z directions). Spurious vectors accounted for less than 5% of the total vector field and were replaced with second-, third-, or fourth-choice vectors using a remove-and-replace median filter. This was only applied to spurious vectors whose variance from the median of eight neighboring vectors was more than twice the variance of these neighboring vectors.

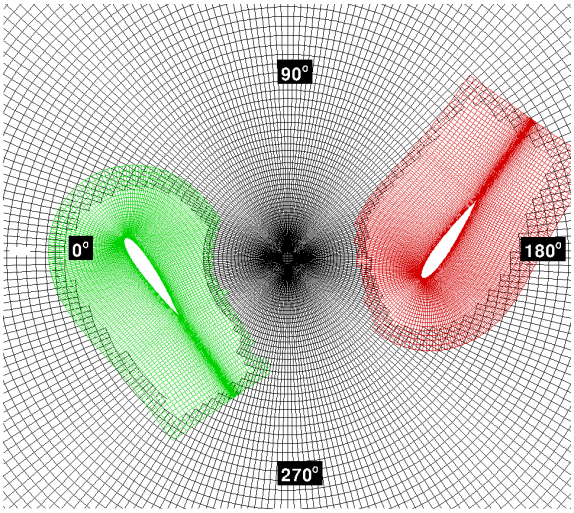

Figure 4.2: 2-D CFD mesh grid [58].

4.2.3 CFD Validation

An important part of the flow field studies was to obtain blade instantaneous forces along the rotor azimuth. However, the experimental setup did not have the capability to measure instantaneous blade forces. In general, it is difficult to implement devices (e.g. pressure taps, strain gauges) to experimentally measure instantaneous blade forces on MAV-scale rotary wing systems due to the imposed space constraints and the high centrifugal load environments in which they operate. Therefore, CFD predictions of the instantaneous blade forces were utilized.

The 2-D CFD studies were performed by Lakshminarayan [58]. The CFD simulations utilized a compressible structured overset RANS solver, OVERTURNS [56]. An overset system of meshes, consisting of a C-type airfoil mesh for each blade and a cylindrical background mesh, was used for the computations. Figure 4.2 shows the mesh system. In this figure, only the field points (points where the flow

equations are solved) are shown. The CFD simulations were performed with and without the use of a transition model to improve the prediction of the RANS model. A two equation $\gamma - \overline{Re_{\theta t}}$ – SA model developed by Medida and Baeder [57] was employed in the simulations using the transition model. The results in Fig. 4.3 show the CFD predictions with and without the transition model. Further details on the grid system and flow solver are presented in [58].

Prior to utilizing the CFD-predicted instantaneous force data, however, an important step was to obtain sufficient validation. The CFD predictions were validated using: 1) experimental time-averaged forces and 2) PIV time-averaged flow field.

4.2.3.1 CFD vs. Experiment: Time-Averaged Forces

Figure 4.3 shows a comparison between the CFD predictions and experimentally measured values for time-averaged lift, propulsive force and power for different advance ratios. The CFD-predicted values show strong correlation with the experimental measurements, both with and without the transition model. However, the CFD results with the transition model show better correlation with experiment; therefore, all CFD results presented in the current Chapter include the transition model. Even though the use of a transition model improves the prediction, the results without a transition model also showed a good qualitative agreement and such simulations might still be valuable if a CFD code is not equipped with a transition model.

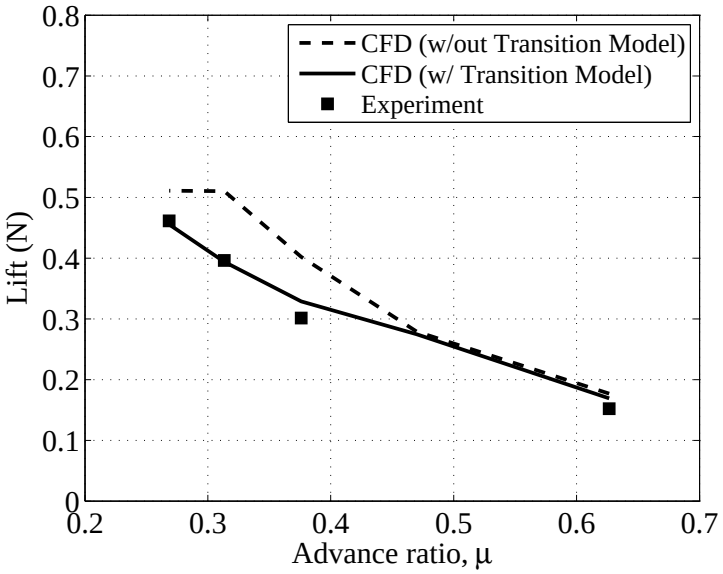

(a) Time-averaged lift.

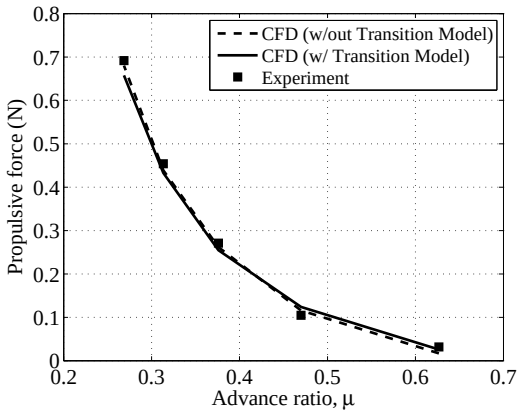

(b) Time-averaged propulsive force.

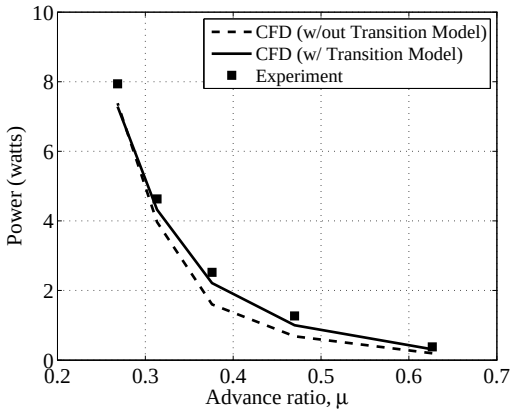

(c) Time-averaged power.

Figure 4.3: Comparison of time-averaged lift, propulsive force and power at different advance ratios between CFD predictions and experimentally measured values.

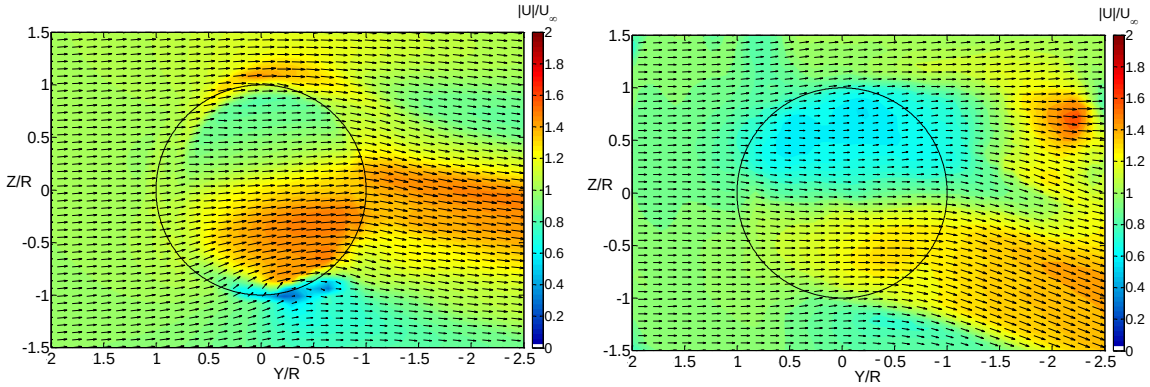

(a) CFD predicted velocity field.

(b) PIV measured velocity field.

Figure 4.4: Comparison of the time-averaged flow field predicted by CFD and measured using PIV at advance ratio $\mu = 0.52$.

4.2.3.2 CFD vs. PIV: Flow Field

The time-averaged flow field predicted by CFD was also compared to PIV measurements. The CFD solution was interpolated onto the PIV grid for the purpose of comparison. Figure 4.4 shows both the CFD predicted flow field and PIV measured flow field at an advance ratio of 0.52 ($U_\infty = 5\,\mathrm{m/s}$, $\Omega R = 9.58\,\mathrm{m/s}$). Although the purpose here is not to analyze the flow field characteristics, it can be seen that many of the flow features seen in the PIV measured flow field are captured in the CFD-predicted results. In both figures, a low velocity region exists in the upper half of the rotor cage while a high velocity region extends from the lower half of the rotor cage into the wake.

Figure 4.5 shows normalized velocity profiles of the time-averaged flow field along the Z direction at various Y/R locations (i.e. vertical sectional cuts). A com-

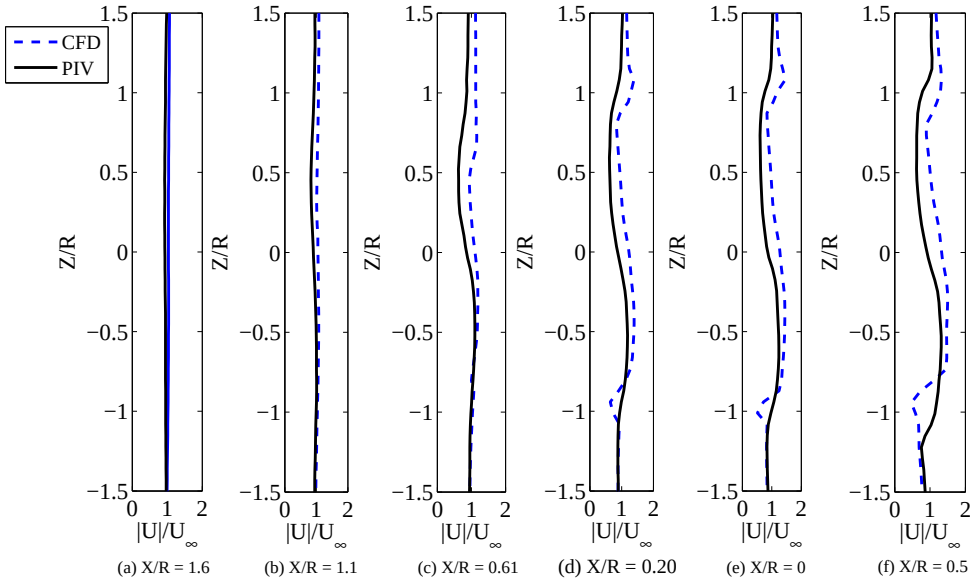

Figure 4.5: Comparison of PIV and CFD velocity profile distribution along Z/R direction at various Y/R locations for advance ratio μ=0.52.

parison between CFD and PIV is made using these velocity profiles. In general, there is good agreement between the velocities predicted by CFD and those measured by PIV, although the CFD results vary slightly in magnitude. Overall, these comparisons between CFD predictions and experimental measurements provided sufficient confidence in the CFD results.

4.3 Results and Discussion

The PIV results will be presented in two parts. The first part examines the time-averaged flow field of the cyclorotor. The principles of cyclorotor force production along the rotor azimuth are explained. The second part examines the phase-averaged flow field, which helps identify the role of unsteady aerodynamics such as blade-wake

interactions in cyclorotor force production. The results are compared with the CFD-predicted values for instantaneous forces and power.

4.3.1 Time-Averaged Flow Field

The time-averaged flow field for the cyclorotor was determined by averaging the instantaneous velocity fields over one complete rotor revolution (80 images per revolution). These results were subsequently averaged for multiple rotor revolutions. A total of 10 rotor revolutions (800 images) were averaged for advance ratio $\mu = 0.52$, and 5 rotor revolutions (400 images) for advance ratios $\mu = 0.31$ and $\mu = 0.73$. Masked regions were excluded from the averaging process.

The time-averaged flow fields corresponding to the three advance ratios are shown in Fig. 4.6. In these images, each vector represents the local flow velocity and its magnitude was calculated using the horizontal (u) and vertical (v) velocity components:

$$|U| = \sqrt{u^2 + v^2} \tag{4.1}$$

The velocity field is normalized by the freestream flow velocity, which travels from left to right. Also, the Y and Z distances have been non-dimensionalized by the rotor radius (R), with the rotation axis of the cyclorotor located at (Y/R, Z/R) = (0, 0).

Several key insights can be gained from Fig. 4.6. First, for all three advance ratios, the flow velocity decreases in magnitude as it passes through the upper half

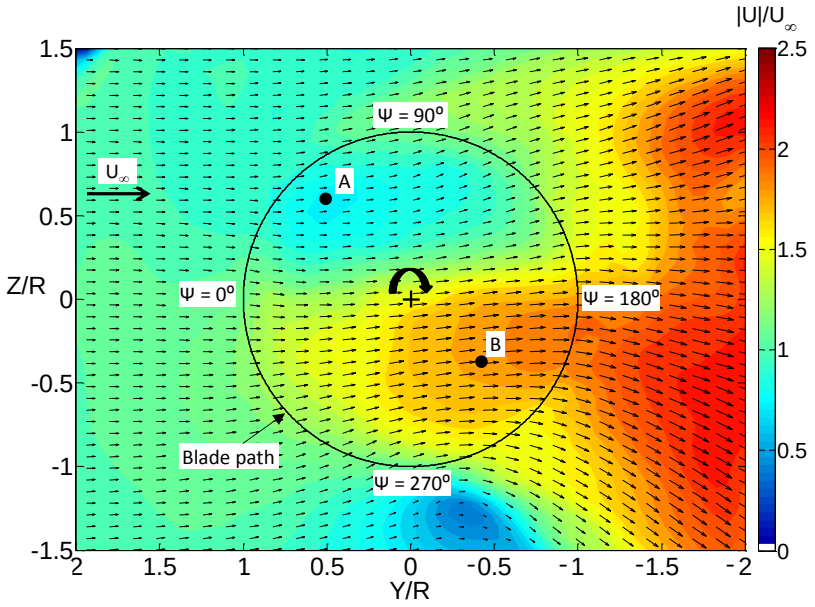

(a) μ=0.31 (U_∞=3 m/s, Ω=1200 rpm).

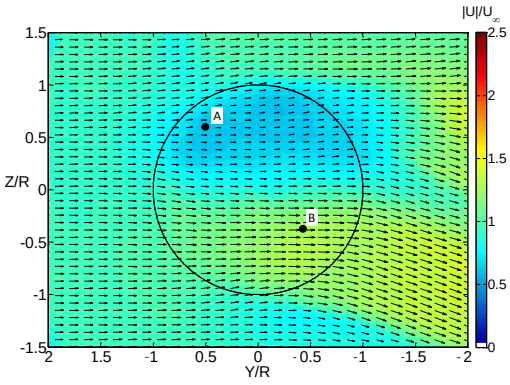

(b) μ=0.52 (U_∞=5 m/s, Ω=1200 rpm).

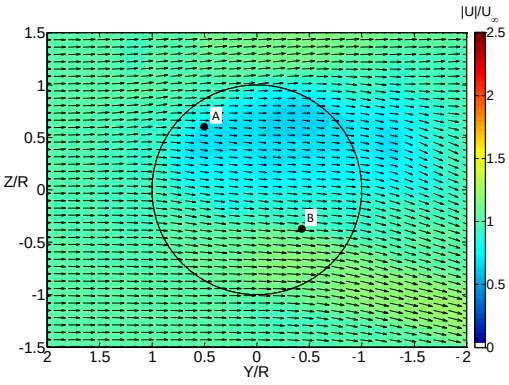

(c) μ=0.73 (U_∞=7 m/s, Ω=1200 rpm).

Figure 4.6: Time-averaged velocity field calculated using time-resolved PIV measurements at different advance ratios.

of the rotor cage (the area enclosed by the circular blade path). For example, in Fig. 4.6a, the local flow velocity at point A is $|U|_A = 2.4$ m/s which is 20% lower than the freestream value of $U_\infty = 3\,\mathrm{m/s}$. These results can be more clearly seen for the higher advance ratio cases of $\mu = 0.52$ and $\mu = 0.73$ (Figs. 4.6b and 4.6c), where the flow velocity at point A is nearly 30% lower than the freestream value in each case. The decreased magnitude of the flow velocities in this region suggests that the blades are extracting energy between azimuthal positions of $\psi = 0°$ to $\psi = 90°$.

Figure 4.6 also shows that the flow gains momentum as it approaches and passes through the lower-rear quadrant of the rotor ($\psi = 180°$ to $\psi = 270°$). At point B in Fig. 4.6a, the flow velocity is nearly 80% greater ($|U|_B = 5.4\,\mathrm{m/s}$) than the freestream value. The flow in the upper half also gains momentum as it exits the upper-rear quadrant of the rotor ($\psi = 90°$ to $\psi = 180°$), as seen by the increased flow velocities in the rotor wake. These observations imply that the blades are adding energy to the flow in the rear half of the cyclorotor. This is especially true in the lower-rear quadrant ($\psi = 180°$ to $\psi = 270°$), where the most significant increases in local flow velocities are visible.

The net increase in momentum in the Y-direction suggests that the rotor is producing a positive net propulsive force. Furthermore, the downward change in direction of the flow in the rotor wake (Fig. 4.6a) corresponds to a net momentum change in the Z-direction, which implies the rotor is producing a net lift force. Together, these observations for rotor lift and propulsive force are confirmed by the experimentally measured time-averaged performance measurements presented (Ta-

Table 4.1: Experimentally measured time-average lift, propulsive force and power.

Advance ratio (μ)	Lift (N)	Propulsive Force (N)	Power (W)
0.31	0.40	0.45	4.63
0.52	0.49	0.26	3.55
0.73	0.64	0.06	2.50

ble 4.1). For all three advance ratios, the rotor produces positive lift and propulsive force. The rotor power decreases with increasing advance ratio, and this is likely due to increased power extraction by the blades between $\psi = 0°$ to $\psi = 90°$.

As discussed previously, estimations of the instantaneous force distributions along the rotor azimuth can be obtained using CFD. Figure. 4.7 shows the CFD-predicted instantaneous lift, propulsive force and power for one blade as a function of rotor azimuth at different advance ratios. It is important to note here that these forces represent the contributions of the blade to the rotor lift and propulsive force, and therefore should not be confused with the local blade lift and drag forces.

A schematic of the cyclorotor is presented in Fig. 4.7a for reference. Figure 4.7b shows that the majority of the lift force is produced in the lower-aft quadrant of the cyclorotor ($\psi = 180°$ to $\psi = 270°$) for all three advance ratios. Also, the blades produce a slightly negative lift in most of the upper half ($\psi = 45°$ to $\psi = 130°$). Figure 4.7c reveals that the rear half of the rotor ($\psi = 90°$ to $\psi = 270°$) is the primary propulsive force producing region. The blades produce a negative propulsive force

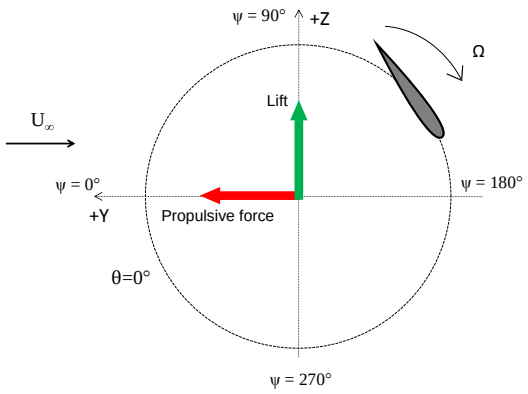

(a) Schematic of cyclorotor (only one blade shown).

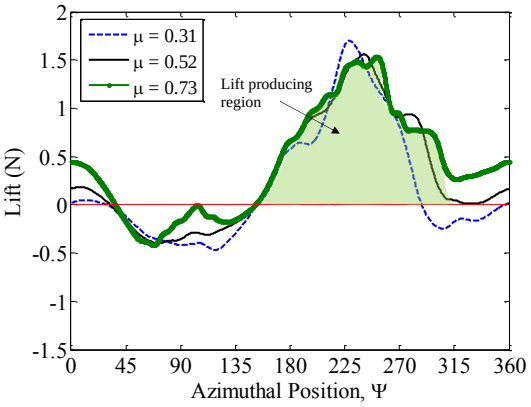

(b) CFD-predicted lift variation.

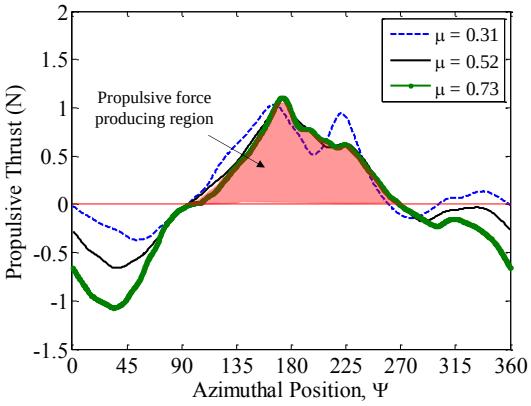

(c) CFD-predicted propulsive force variation.

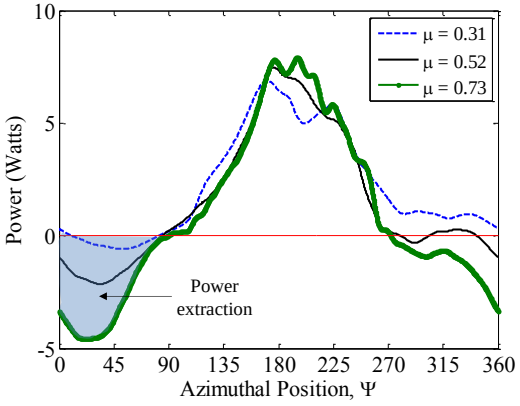

(d) CFD-predicted power variation.

Figure 4.7: CFD-predicted lift, propulsive force and power of one blade as a function of rotor azimuth at different advance ratios.

across the frontal half ($\psi = 270°$ to $\psi = 90°$), which increases in magnitude at higher advance ratios (Fig. 4.7c). Furthermore, Fig. 4.7d shows the variation in power along the rotor azimuth. The blades experience negative values of power (i.e. power extraction) along the frontal half of the rotor, especially in the upper-frontal quadrant ($\psi = 0°$ to $\psi = 90°$). These negative values of power are consistent with the decreased flow velocities observed in this region from the time-averaged PIV flow field.

At this point, a simple aerodynamic analysis will be presented to help develop a better understanding of the results in Fig. 4.6 and 4.7. Specifically, the local aerodynamic environment of the blade will be examined at different azimuthal positions, and the observations made in this analysis will be used to explain the contributions of the blade to rotor lift, propulsive force and power along the rotor azimuth. The analysis will be carried out for a moderate advance ratio of $\mu = 0.52$.

At a given azimuthal position, the three key factors that determine whether the local blade forces contribute to the rotor lift or propulsive force are: 1) the magnitude of the local resultant velocity acting on the blade, 2) the effective aerodynamic angle of attack of the blade and 3) the orientation of the blade with respect to the freestream. The magnitude and direction of the local resultant velocity vector with respect to the blade chord line can be obtained through a vector summation of the local flow velocity and the blade tangential velocity:

$$\vec{U}_{resultant} = \vec{U}_{local} + \vec{U}_{blade} \tag{4.2}$$

(a) Geometric airfoil in curvilinear flow.

(b) Virtual airfoil with camber and incidence in rectilinear flow.

Figure 4.8: Schematic illustrating flow curvature effects on a cyclorotor.

For simplicity, the local flow vector will be assumed to be in the direction of the freestream. The magnitude of the local flow velocities at various azimuthal positions can be obtained using the mean flow field results from PIV.

The effective aerodynamic angle of attack of the blade is a function of the geometric pitch angle (θ), the angle of attack between the resultant velocity vector and the blade chord line (α), as well as an incidence angle (α_i) which results from flow curvature effects on the blade:

$$\alpha_{eff} = f(\theta, \alpha, \alpha_i) \tag{4.3}$$

Flow curvature effects on the blades of a cyclorotor result from a chord-wise variation in the local flow velocity, which can be attributed to the orbital motion of the blades [59]. These flow curvature effects lead to a curvilinear flow along the blade chord, as depicted in Fig. 4.8a. Furthermore, a geometrically symmetric airfoil immersed in a curvilinear flow can be represented as a cambered airfoil in a rectilinear flow. This is illustrated in Fig. 4.8. For the cyclorotor used in the present study (R = 0.076 m, c = 0.05 m, c/R=0.65), a linear approximation [59] shows that

the virtual camber is approximately 8% of the blade chord. In addition, due to the fact that the blade pitching axis is positioned at the quarter-chord and not at the mid-chord, the blade experiences a virtual incidence angle, which is approximately 9° (calculated using the linear model in [59]. Therefore, these values for camber and incidence clearly suggest that flow curvature effects are not negligible for the present cyclorotor. In order to account for flow curvature effects in the current aerodynamic analysis, the *geometric* airfoil is represented as a *virtual* airfoil that features both camber and incidence angle.

The schematics presented in Fig. 4.9 were derived based on the local flow velocities acting on the blade. Figure 4.9a shows the blade at eight different azimuthal positions: $\psi = 0°$, 45°, 90°, 135°, 180°, 215°, 270° and 315°. Here, the camber line (red) corresponds to the virtual airfoil and is superimposed on the geometric airfoil. The local resultant velocity vectors acting on the blade at each azimuthal position are also sketched (in green). Note that these velocity vectors are drawn to scale, based on the local flow velocity (U) and the blade tangential velocity (ΩR). The local flow velocities (U) were obtained using the PIV measurements. Using the information provided in Fig. 4.9a, the directions of the local blade lift and drag forces can be obtained and are shown in Fig. 4.9b. Together, the schematics in Fig. 4.9 will now be used to explain the contributions of the local blade forces to the overall rotor lift and propulsive force in the four regions (Fig. 4.9a) of the rotor azimuth.

Region I: At $\psi = 0°$, the effective angle of attack of the blade is approximately zero, as depicted in Fig. 4.9a. However, the blade is still expected to produce a lift force due to its virtual camber. Based on the orientation of the blade with respect

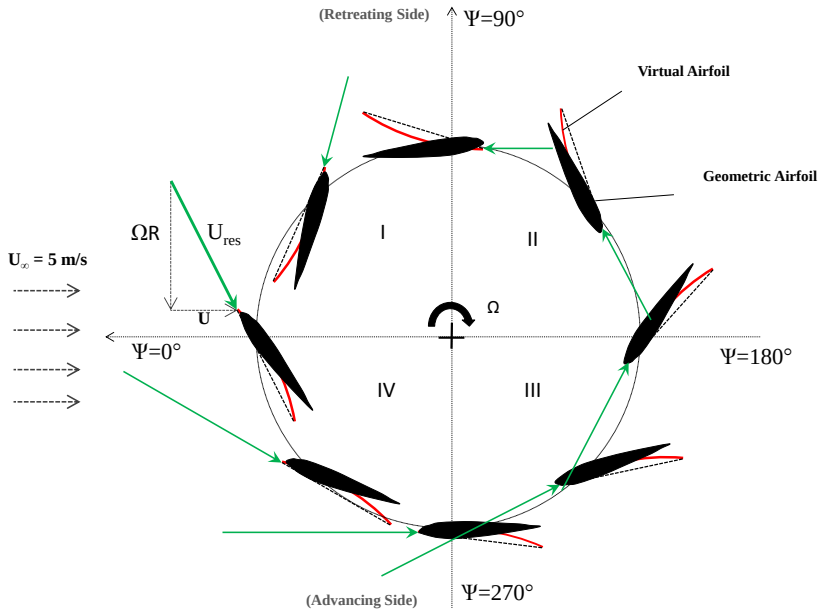

(a) Geometric and virtual airfoils with local resultant velocity vectors.

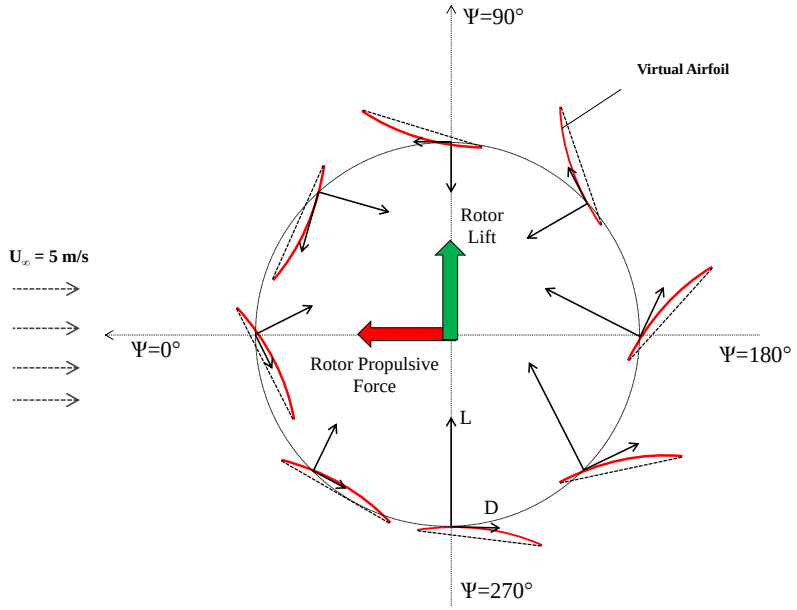

(b) Lift and drag forces on the blade.

Figure 4.9: Schematics showing local aerodynamics of blade at several azimuthal positions for advance ratio 0.52.

to the freestream, the blade lift force is expected to increase the net rotor lift, but decrease the net propulsive force (Fig. 4.9b). The CFD-predicted results in Figs. 4.7b and 4.7c support this finding, as they show negative values for propulsive force and positive values for lift.

At $\psi = 45°$, the blade operates with a slightly positive effective angle of attack. However, the orientation of the blade is such that the lift force acts to decrease both rotor propulsive force and rotor lift. Furthermore, the blade produces a force in the direction opposing the freestream flow and as a result the incoming flow velocity is expected to decrease across this region. This is consistent with the observations made previously in the PIV flow field measurements (Figs. 4.6b). In reducing the flow velocities, the blade extracts energy from the flow; this is evidenced by the negative values of power observed in the CFD results (Fig. 4.7d).

Region II: At $\psi = 90°$, the blade operates with an increased effective angle of attack. However, it is clear from Fig. 4.9b that the orientation of the blade is such the majority of the blade lift force will be in the negative Z-axis direction, which decreases the net rotor lift. This coincides with the negative values of lift observed in this region from CFD predicted results (Fig. 4.7b). It should be noted, however, that the blade is in the retreating half of the rotor in this region and therefore experiences lower local resultant velocities. Thus, the decreases in net rotor lift will be less pronounced.

At $\psi = 135°$, the blade is at a slight positive effective angle of attack. Based on the orientation of the blade in Fig. 4.9b, the local lift force has components along the positive Y-axis and negative Z-axis directions. Therefore, the blade increases

the net rotor propulsive force, but continues to decrease the net rotor lift. It should be recalled that the local flow velocities in this region are lower in magnitude due to the power extraction by the blades in region I. Therefore, the blade effective angle of attack in region II will be slightly greater compared to region I.

Region III: At $\psi = 180°$, the blade has an increased effective angle of attack. The orientation of the blade reveals that the blade contributes to positive rotor lift and propulsive force. The contribution of the blade forces to the rotor propulsive force will be maximum at an azimuthal location between $\psi = 135°$ and $\psi = 180°$, when its local lift vector becomes parallel to the free stream. This observation is captured in the CFD-predicted results in Fig. 4.7c, where the maximum propulsive force value occurs at approximately $\psi = 170°$.

At $\psi = 225°$, the blade experiences a large positive effective angle of attack (Fig. 4.9a). Therefore, as shown in Fig. 4.9b, the local aerodynamic forces on the blade are significant. Furthermore, the orientation of the blade suggests blade lift force will have components in the positive Y-axis and Z-axis directions. Thus, the blade contributes to positive rotor propulsive force and lift in this region.

Region IV: At $\psi = 270°$, the blade is still at a relatively large positive effective angle of attack. Figure 4.9b shows that the majority of the blade lift force is along the positive Z-axis direction and therefore the primary contribution will be to the rotor lift.

At $\psi = 315°$, the blade is close to a zero effective angle of attack. However the virtual camber allows the blade to produce a non-zero local lift force, which has components along the negative Y-axis and positive Z-axis directions. Thus, the

blade still contributes to the net rotor lift, but decreases the net propulsive force in this region.

Although the above discussion was for one particular advance ratio ($\mu = 0.52$), the same general principles were found to hold true for the lower and higher advance ratios ($\mu = 0.31$ and $\mu = 0.73$). However, the effective angle of attack distribution of the blades along the rotor azimuth will be different due to variations in the freestream velocity (constant Ω). From the CFD results presented in Figs. 4.7b–4.7d, it can be seen that the primary lift and propulsive force producing regions remain relatively the same for the three different advance ratios. Figure 4.7d shows that the effect of increasing advance ratio is to increase the power extraction along the frontal half of the rotor ($\psi = 270^\circ$ to $\psi = 90^\circ$), whereas the power in the rear half of the rotor azimuth remains relatively constant. This is a key reason for the decrease in power observed in the time-averaged experimental measurements (Table 4.1).

The analysis just presented uses a simplified model, but it effectively provides a fundamental understanding of the physics behind the distribution of forces and power along the rotor azimuth. These insights can assist with the design of a rotor for a flight-capable cyclocopter MAV. For example, asymmetric pitching kinematics, where one-half of the rotor operates at larger pitch angles than the corresponding half, may help improve rotor propulsive efficiency by leading to a more uniform azimuthal distribution of forces. Also, the idea of using geometrically cambered airfoils for improving cyclorotor performance may be worthwhile to consider.

4.3.2 Phase-Averaged Flow Field

Time-averaged PIV results provide insights into the mean flow field of a cyclorotor, but do not show the effects of unsteady aerodynamic flow features. In the current section, the phase-averaged PIV flow field is analyzed and the unsteady flow features are quantified and evaluated based on their impact on the aerodynamic performance of the blades at specific azimuthal positions.

As described previously, the PIV time-resolved measurements were acquired at a sampling rate of 1.6 kHz, and the rotor operated at 20 Hz (1200 rpm). This provided a total of 80 images for the flow field measurements. Because of the symmetry of the 2-bladed rotor, it was possible to analyze two blade azimuthal positions using one flow field image. In the following results, the upstream blade will be referred to as blade A and the downstream blade will be referred to as blade B. Thus, for example, when blade A is positioned at $\psi_A = 0°$, blade B is positioned at $\psi_B = 180°$, etc. This constitutes a "pair" of azimuthal positions.

Instantaneous flow field measurements for each pair of azimuthal positions were isolated from the data set. The data set spanned 9.5 full rotor revolutions, therefore providing 19 instantaneous flow field measurements (i.e. one image for each rotor half-revolution) for each pair of azimuthal positions. The instantaneous velocity fields corresponding to the 19 images were then averaged to obtain the phase-averaged velocity field. Phase-averaging in this way highlights prominent periodic flow features and reduces the appearance of aperiodic effects in the flow.

In the following analysis, phase-averaged results will be considered for the

moderate advance ratio case of $\mu = 0.52$ (U_∞=5 m/s, Ω=1200 rpm). A total of four pairs of azimuthal positions will be considered: 1) $\psi_A = 330°$, $\psi_B = 150°$ 2) $\psi_A = 0°$, $\psi_B = 180°$ 3) $\psi_A = 30°$, $\psi_B = 210°$ and 4) $\psi_A = 60°$, $\psi_B = 240°$. Emphasis is placed on the rear half of the rotor azimuth, where the blades operate in the wake of the frontal half and are therefore exposed to several unsteady aerodynamic flow features (most notably, blade-wake interactions).

4.3.2.1 Flow Periodicity

The process of phase-averaging highlights the periodic features of a flow. One way of assessing flow periodicity is by comparing the variance of a velocity profile at a given vertical section over multiple rotor revolutions. Figure 4.10a shows profiles of total velocity (normalized by the freestream velocity) at the center of the rotor (Y/R = 0). The 19 instantaneous flow field images (blue) and the final phase-averaged result (red) are shown in Fig. 4.10a. For the data shown here, the blades are at azimuthal locations of $\psi = 0°$ (rotor forward) and $\psi = 180°$ (rotor aft). In general, the instantaneous velocity profiles show good agreement; the aperiodicity of the flow is captured in the deviations of the instantaneous velocity profiles from the phase-averaged velocity profile. The effects of phase-averaging on the flow field are illustrated in Fig. 4.10b–4.10c where an instantaneous vorticity field is compared with the phase-averaged vorticity field. The instantaneous vorticity field (Fig. 4.10b) reveals numerous discrete vortices, especially in the upper-rear quadrant ($\psi = 90°$ to $\psi = 180°$) of the rotor. The phase-averaged vorticity field (Fig. 4.10c) appears more

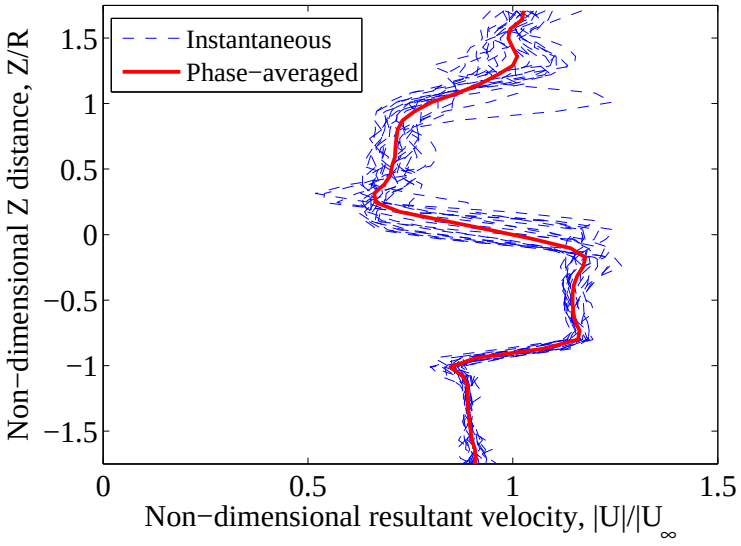

(a) Velocity distribution along Z-axis at Y/R = 0.

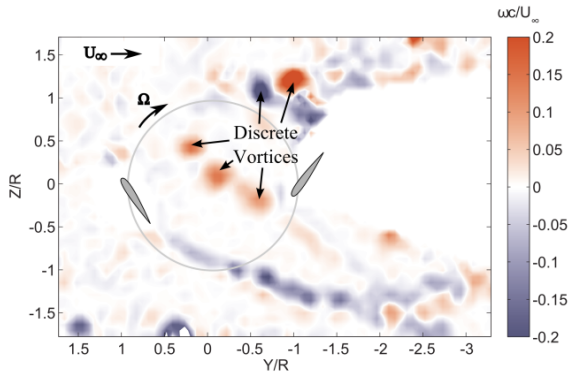

(b) Instantaneous vorticity field.

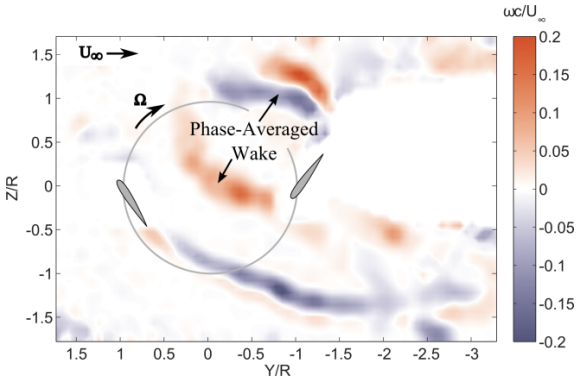

(c) Phase-averaged vorticity field.

Figure 4.10: Comparison of instantaneous and phase-averaged flow with blades at ψ_A=0° and ψ_B=180° (μ=0.52).

diffuse, which can be attributed to variations in the spatial position and intensity of the vortices between rotor revolutions. However, it can be seen that the phase-averaged vorticity field more clearly shows the general shape and trajectory of the blade wakes. A detailed discussion on these blade wakes follows in the remainder of this section.

4.3.2.2 Blade-Wake Interactions

Figures 4.11–4.14 show phase-averaged flow fields for different blade azimuthal positions. Each figure consists of: (a) an instantaneous smoke flow visualization image, (b) the total velocity field, non-dimensionalized by the freestream velocity, and (c) the vorticity field, scaled by the blade chord and non-dimensionalized by the freestream velocity:

$$\omega^* = \frac{\omega c}{U_\infty} \tag{4.4}$$

In the velocity contour plots, only one-eighth of the total vectors calculated in the y-direction are shown for clarity. In the vorticity contour plots, positive vorticity (red) corresponds to counter-clockwise rotation and negative vorticity (blue) corresponds to clockwise rotation. In all figures, the freestream velocity is from left to right.

Figure 4.11 shows phase-averaged results for the two blades at azimuthal positions of $\psi_A = 330°$ and $\psi_B = 150°$ at an advance ratio of 0.52. The flow visualization image (Fig. 4.11a) reveals two wake structures (denoted as wakes A and B) gener-

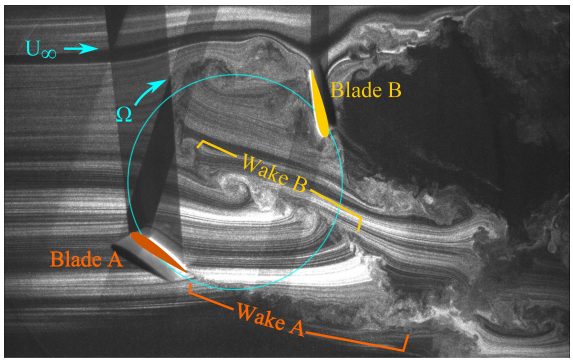

(a) Instantaneous flow visualization.

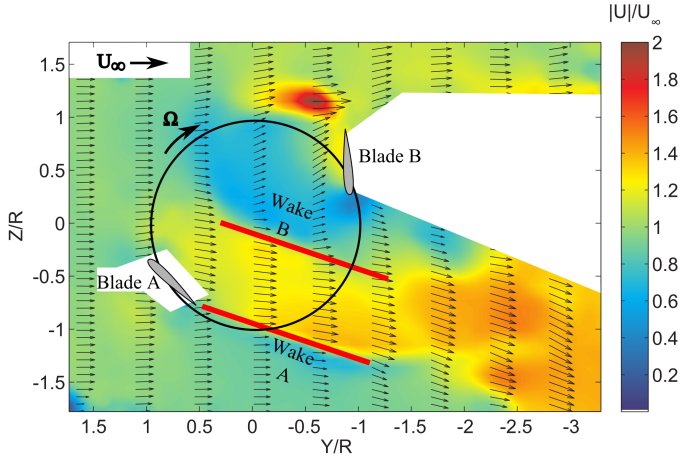

(b) Velocity field.

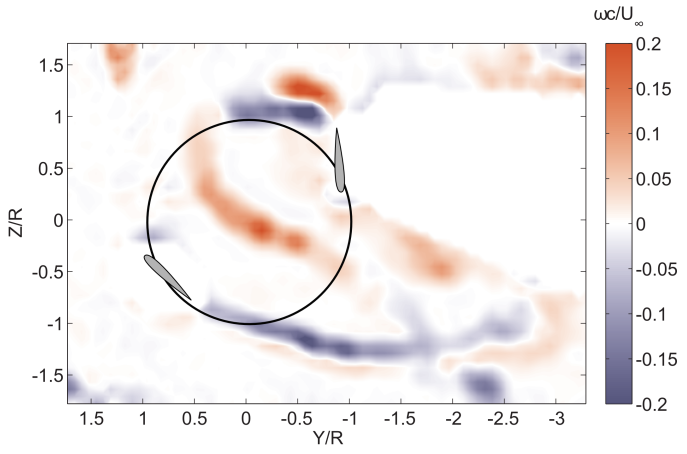

(c) Vorticity field.

Figure 4.11: Phase-averaged flow field with blades at ψ_A=330° and ψ_B=150° (μ=0.52).

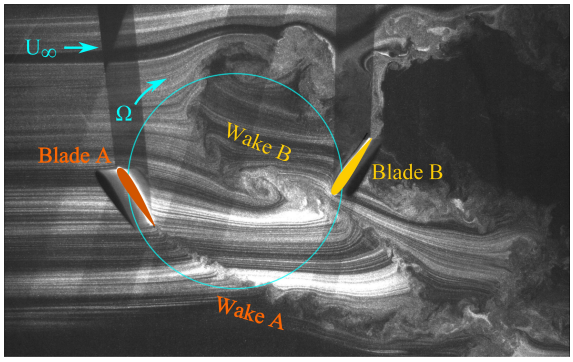

(a) Instantaneous flow visualization.

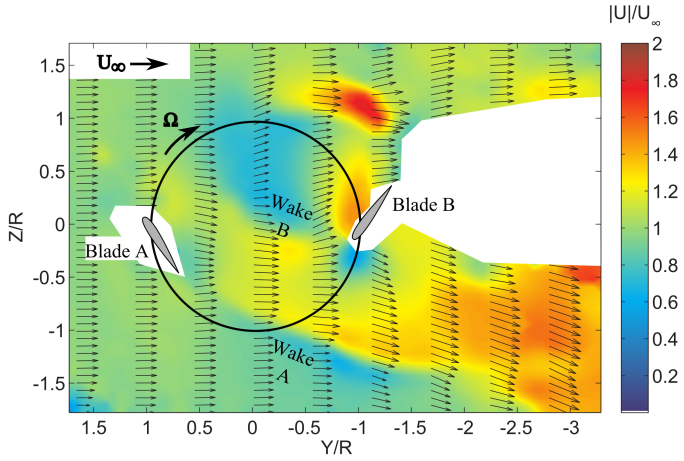

(b) Velocity field.

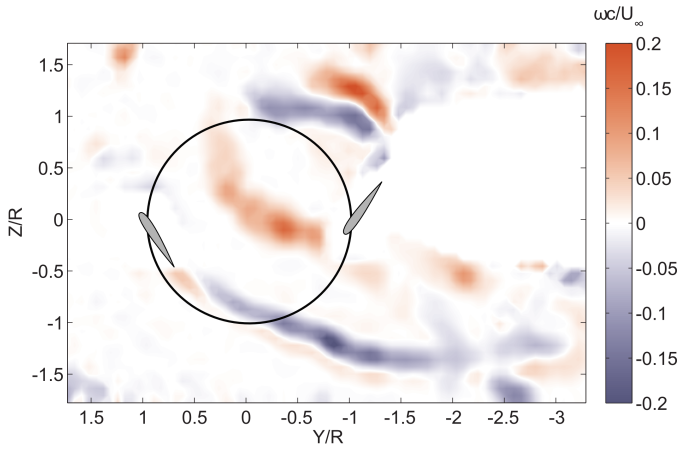

(c) Vorticity field.

Figure 4.12: Phase-averaged flow field with blades at ψ_A=0° and ψ_B=180° (μ=0.52).

ated by the blades. Wake A follows blade A, which experiences fully attached flow due to its low effective aerodynamic angle of attack in this region. Wake B follows blade B and has begun to convect downstream as a result of the incoming flow; the wake age of wake B is one-half of a rotor revolution older than wake A. A close look at the flow visualization reveals that these trails of vorticity are made up of small-scale vortices, a result of a Kelvin-Helmoholtz instability along each shear layer [60].

Figure 4.11b shows the corresponding velocity contour plot, and illustrates the two shear layers formed by the blade wakes. Each shear layer separates a high velocity region from a low velocity region, and the direction of rotation of the vortices along the shear layer is determined by this separation. The vorticity contour plot (Fig. 4.11c) reveals that wake A primarily consists of clockwise (negative) vorticity while wake B consists of a trail of counter-clockwise (positive) vorticity that extends through the rotor cage. The rotation direction of the vortices will become important when evaluating the blade-wake interactions that take place as blade B progresses further along the azimuth.

Figure 4.12 shows blades A and B advanced to azimuthal positions of $\psi_A = 0°$ and $\psi_B = 180°$ for an advance ratio of 0.52. The flow visualization image (Fig. 4.12a) shows the leading edge of blade B approaching the trail of counter-clockwise vortices of wake B. The velocity contour plot in Fig. 4.12b reveals a slightly increased velocity region near the upper surface of blade B.

Figure 4.13 shows blades A and B advanced to $\psi_A = 30°$ and $\psi_B = 210°$ for an advance ratio of 0.52. From Fig. 4.13a, a blade-wake interaction between the

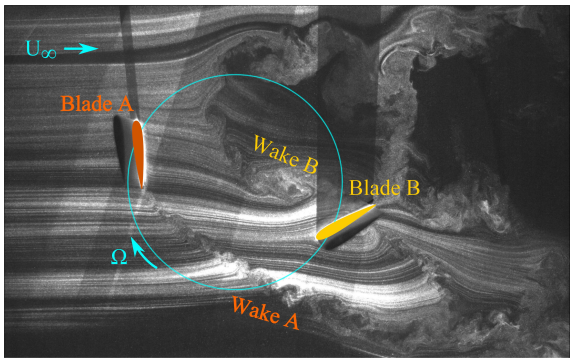

(a) Instantaneous flow visualization.

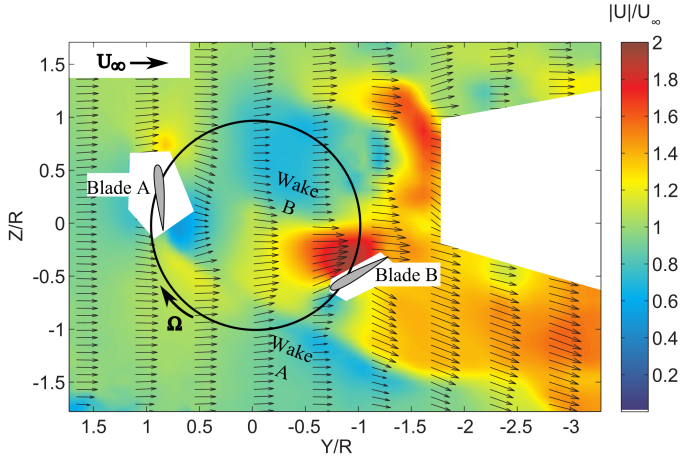

(b) Velocity field.

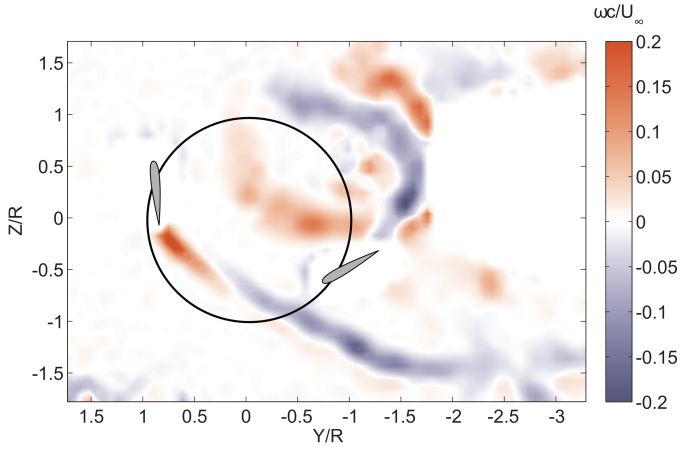

(c) Vorticity field.

Figure 4.13: Phase-averaged flow field with blades at ψ_A=30° and ψ_B=210° (μ=0.52).

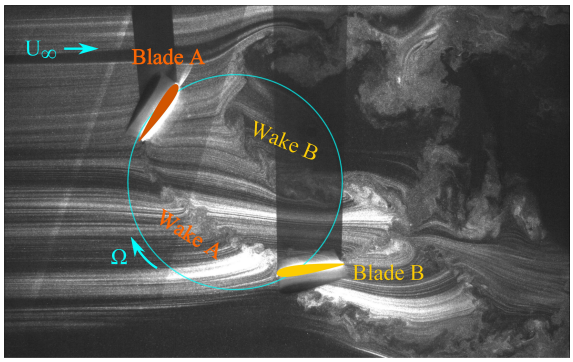

(a) Instantaneous flow visualization.

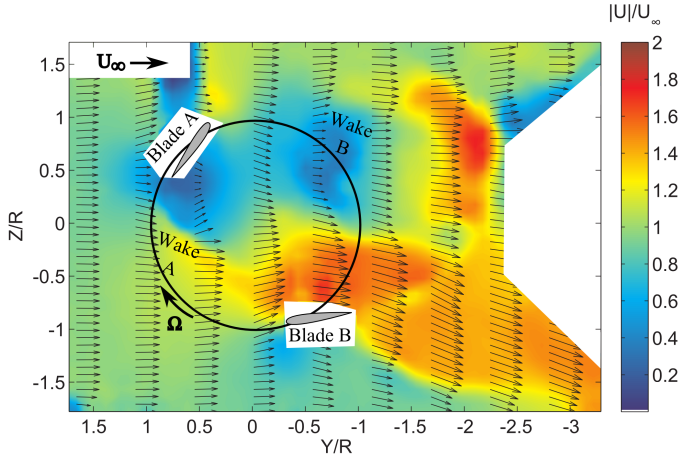

(b) Velocity field.

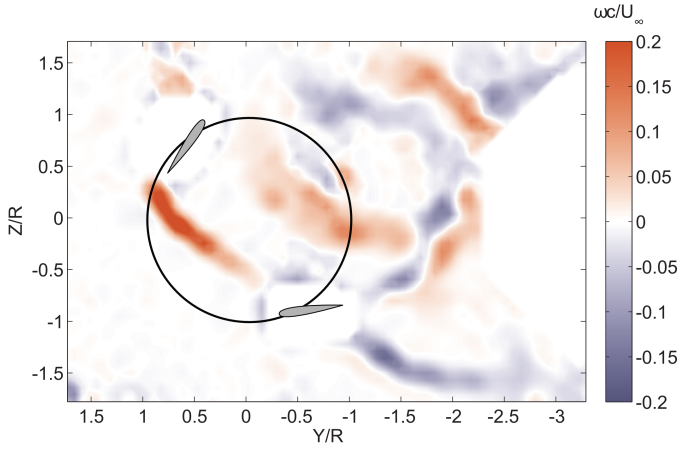

(c) Vorticity field.

Figure 4.14: Phase-averaged flow field with blades at ψ_A=60° and ψ_B=240° (μ=0.52).

upper surface of blade B and the counter-clockwise vortices of wake B can clearly be seen. The velocity contour plot (Fig. 4.13b) shows that this interaction leads to significantly increased flow velocities over the upper surface of blade B. It was shown in the previous section that the blade operates with a positive effective angle attack and experiences high dynamic pressure in this region. These two characteristics, combined with the blade-wake interaction, increase the local flow velocity on the upper surface of blade B to almost twice the freestream value. Meanwhile, the flow near blade A is nearly perpendicular to the blade chord. The flow downstream of blade A is slowed (to the right and down of the blade in Figure 4.13b); blade A is operating in a power extraction region as discussed previously. This prompts a change in the direction of vorticity in the shear layer formed in wake A, as evidenced by Fig. 4.13c.

Figure 4.14 shows the blades at $\psi_A = 60°$ and $\psi_B = 240°$. The flow visualization image shows a second blade-wake interaction, which occurs between blade B and the wake of blade A. The result is a high velocity region on the upper surface of blade B (Fig. 4.14b). However, the magnitude of the flow velocities are slightly lower than those observed during the first blade-wake interaction.

It should be noted that the location and intensity of the vortices along the wakes vary with each rotor revolution due to the inherent aperiodicity of the flow. As a result, the exact position of the blade-wake interactions observed in Figs. 4.11–4.14 may vary slightly between revolutions.

Ultimately, it is important to consider the impact of these blade-wake interactions on the aerodynamic performance of the blades. The observations made from

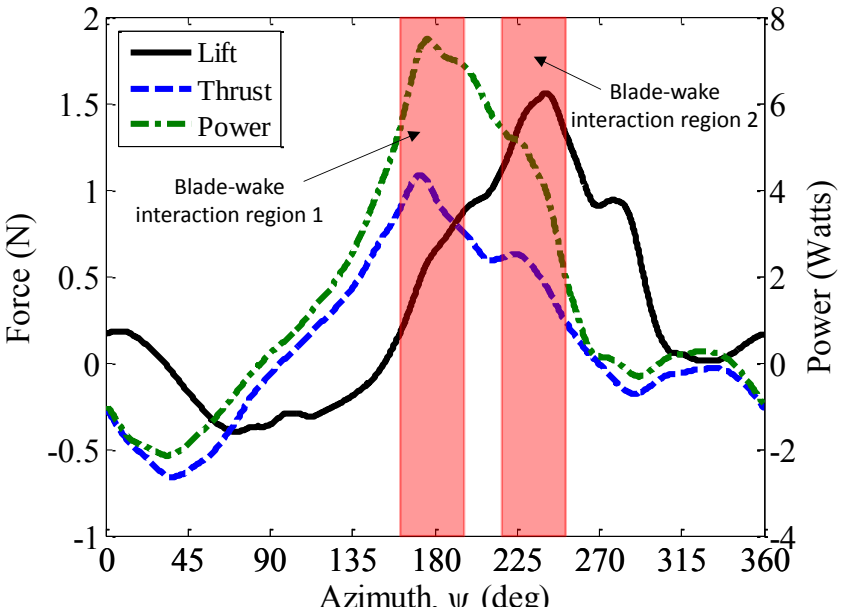

Figure 4.15: CFD-predicted instantanous lift, propulsive force and power. Experimentally observed blade-wake interaction regions shown in red (μ=0.52).

Figs. 4.11–4.14 can be used in conjunction with the CFD-predicted instantaneous lift, propulsive force, and power along the rotor azimuth to quantify the influence of the blade-wake interactions on the aerodynamic performance of the individual blades. The CFD-predicted instantaneous forces and power are presented for an advance ratio of 0.52 in Fig. 4.15. The regions of the experimentally observed blade-wake interactions are highlighted in red. The maximum propulsive thrust generated by the blade occurs near the first blade-wake interaction. Similarly, the maximum blade lift occurs at an azimuthal location where the second blade-wake interaction was observed. An exact one-to-one comparison of the azimuthal locations between the CFD and PIV results may not be possible due to the unsteady nature of the flow, resolution of the image acquisition, and variation from ideal blade pitching

kinematics. However, these findings collectively suggest that unsteady aerodynamic flow features and constructive blade-wake interactions in the rear half of the cyclorotor may be fundamental to enhancing the lift and propulsive thrust.

4.4 Summary

The purpose of the flow field studies was to develop an understanding of the physics behind the force production of the cyclorotor in forward flight. Experimental measurements (time-resolved planar PIV and time-averaged force measurements) were used in conjunction with CFD-predicted instantaneous blade forces to fulfill this objective. In the first half of the paper, time-averaged flow field results calculated using PIV measurements were examined for different advance ratios. An aerodynamic analysis of the blades at various azimuthal locations was presented to describe the flow physics that govern the lift and propulsive force production of the cyclorotor. The second half of the paper focused on the role of unsteady aerodynamic flow features and their impact on the instantaneous force production of the blades as they travel around the rotor azimuth. The unsteady flow features were evaluated using phase-averaged flow field measurements, with the blades at selected azimuthal locations. Observations from this analysis were correlated to CFD-predicted instantaneous aerodynamic forces and power to help understand the role of blade-wake interactions in the generation of lift and propulsive force by the cyclorotor.

Chapter 5: Performance Measurements: Rotor Geometry

5.1 Overview

The results in Chapter 4 clearly showed that flow curvature effects play an important role in the aerodynamic performance of the cyclorotor. The blades experience a curvilinear flow as opposed to a rectilinear flow, leading to a chord-wise variation in local blade velocity which, in turn, results in a 'virtual' camber and incidence angle. The virtual camber affects the coefficients of lift (C_l) and drag (C_d) of the blade sections, and is a strong function of the rotor chord-to-radius (c/R) ratio. The virtual incidence angle affects the blade effective angle of attack along the azimuth, and is a function of the blade pitching axis location as well as the c/R ratio.

The focus of the current section is to experimentally investigate the impact of flow curvature effects on the lift and propulsive force production and power consumption of the cyclorotor by systematically varying: 1) blade chord-to-radius ratio (c/R) and 2) blade chord-wise pitching axis location. The experiments were conducted using the wind-tunnel setup previously described in Section 3.2 (Fig. 3.1). Measurements of time-averaged lift, propulsive force and power were obtained at various forward speeds and rotational speeds. For all cases, the pitching kinematics remained unchanged, with the blade pitch amplitude and pitch phase angle constant

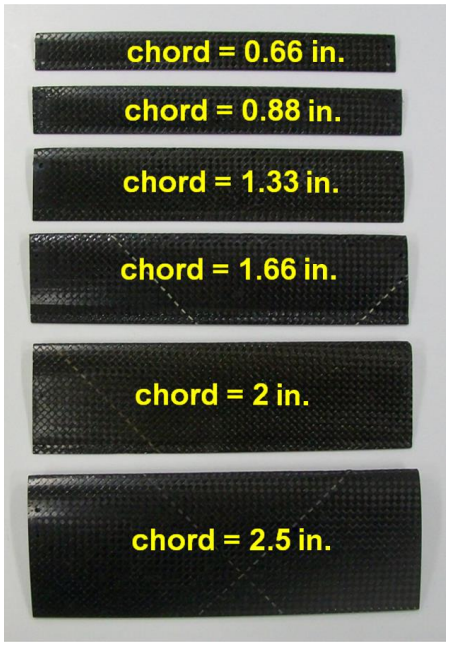

Figure 5.1: Blade chord lengths tested to vary c/R ratio.

at $\theta_A = 45°$ and $\phi = 90°$, respectively. Thus, the blades achieve a pitch angle close to 45° at the front ($\psi = 0°$) and aft ($\psi = 180°$) azimuthal locations, and a pitch angle close to 0° at the top ($\psi = 90°$) and bottom ($\psi = 270°$). This particular configuration was chosen to highlight the role of flow curvature effects. Since the blade experiences a relatively low geometric pitch angle at the top and bottom, the net lift force is intuitively expected to be close to zero. However, the experiments clearly showed the presence of a large non-zero lift force.

5.2 Effect of Chord/Radius Ratio

A total of six blade chord lengths were tested: 0.665, 0.89, 1.33, 1.65, 2, and 2.5 in (Fig. 5.1). The rotor radius was constant at 3 in, and therefore the blade chord lengths correspond to c/R ratios of 0.22, 0.29, 0.44, 0.55, 0.67, and 0.83, respectively.

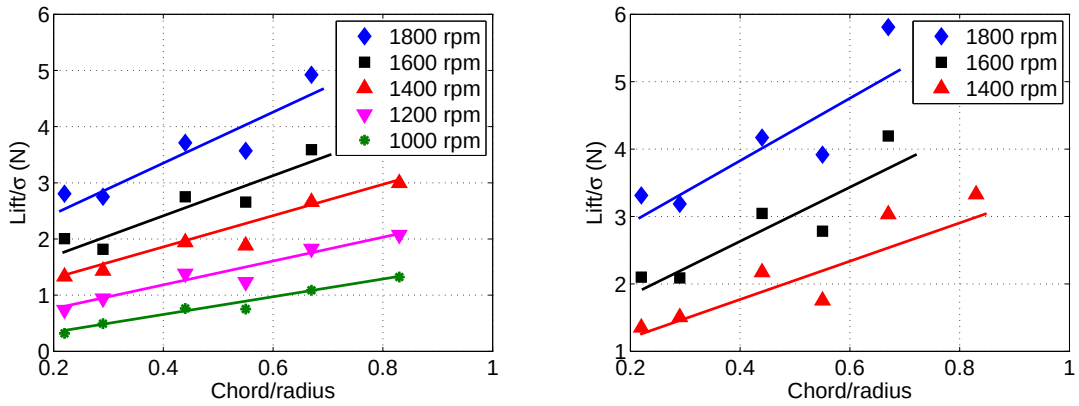

(a) Wind speed = 5 m/s

(b) Wind speed = 9 m/s

Figure 5.2: Lift/solidity versus chord/radius ratio for different rotational speeds with pitching axis at 0.25c.

The blade pitching axis location was fixed at 25% chord from the leading edge (i.e. quarter-chord).

Varying the blade chord (at constant radius) changes the total blade area of the rotor. In order to remove the effect of blade area and highlight the effects of virtual camber and incidence, the cyclorotor lift, propulsive force and power were be non-dimensionalized the rotor solidity (σ):

$$\sigma = \frac{N_b c}{2\pi R} \tag{5.1}$$

where N_b is the number of blades. As indicated in Eq. 5.1, the rotor solidity is a ratio of the total blade area to the cylindrical area swept by the blades.

Figures 5.2–5.4 show the variations in the normalized lift, propulsive force and power as a function of c/R at two different freestream velocities ($U_\infty = 5$ and 9 m/s). For each freestream velocity, multiple rotational speeds are shown. Figure 5.2 shows

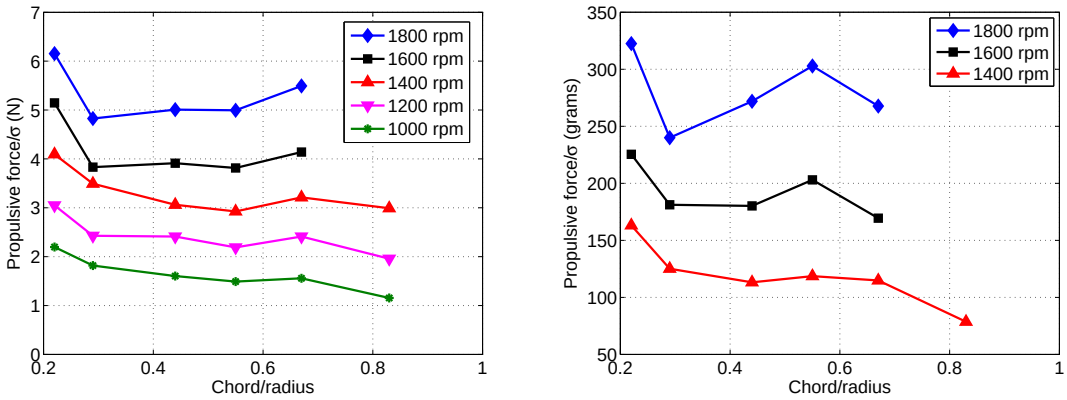

(a) Wind speed = 5 m/s

(b) Wind speed = 9 m/s

Figure 5.3: Propulsive force/solidity versus chord/radius ratio for different rotational speeds with pitching axis at 0.25c.

that as the c/R ratio is increased, the lift increases almost linearly at a given rotational speed. This is true for both freestream velocities tested, although the rate of increase in lift for the higher speed ($U_\infty = 9\,\mathrm{m/s}$) is greater.

Figure 5.3 shows the variation of propulsive force with chord/radius ratio. Compared to the variation in lift, the propulsive force is relatively less sensitive to variations in c/R, although it becomes non-linear at extremely low and high values of c/R. Figure 5.4 shows the variation of power as a function of c/R for the two wind speeds. At both freestream velocities, the rotor power decreases with increasing chord/radius ratio until a critical c/R between 0.4 and 0.5, and then increases. This trend suggests that there may be an optimum c/R for minimum power consumption. From a MAV design perspective, Figs. 5.2–5.4 show that increasing the c/R ratio is an effective method to maximize the lift per unit blade area without significantly impacting propulsive force and power consumption.

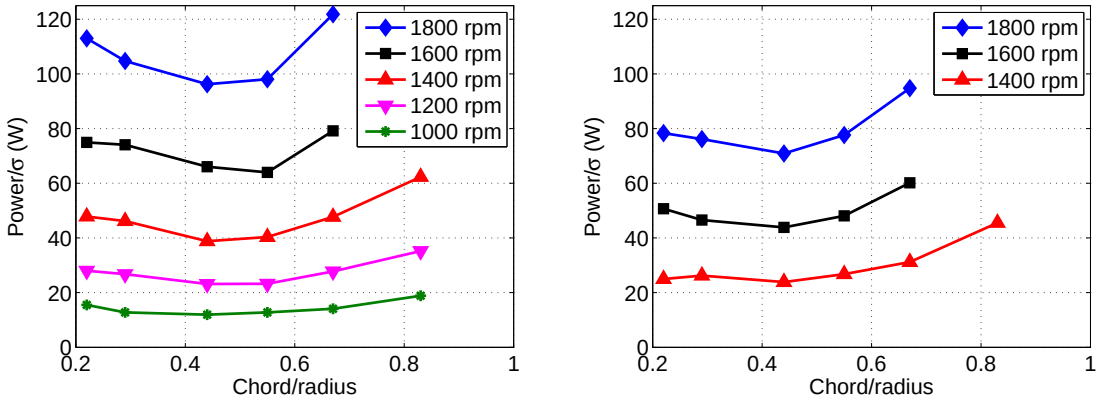

(a) Wind speed = 5 m/s

(b) Wind speed = 9 m/s

Figure 5.4: Power/solidity versus chord/radius ratio for different rotational speeds with pitching axis at 0.25c.

The results in Figs. 5.2–5.4 will now be explained in detail. Specifically, the schematics in Fig. 5.5 will be used in conjunction with the CFD predicted pressure contour plot in Fig. 5.6 to explain the physics behind the trends observed in Figs. 5.2–5.4. The CFD simulation, performed by Lakshminarayan [61], are based on the same methodology and mesh-grid system discussed earlier in Section 4.2.3.

Lift Production — The virtual airfoil and geometric airfoil at four different azimuthal locations are shown in Fig. 5.5a. The geometric blade has a zero angle at the top and bottom locations, since the operating phase angle is $\phi = 90°$. However, as a result of the flow curvature effects, the blade has a negative virtual camber and incidence ($C_l < 0$) in the upper half, and a positive camber and incidence ($C_l > 0$) in the lower half of the trajectory. In the absence of a forward speed (i.e. hover), the blades should produce a force that is equal in magnitude but opposite in direction, canceling each other. In the presence of a forward velocity, however, the magnitudes

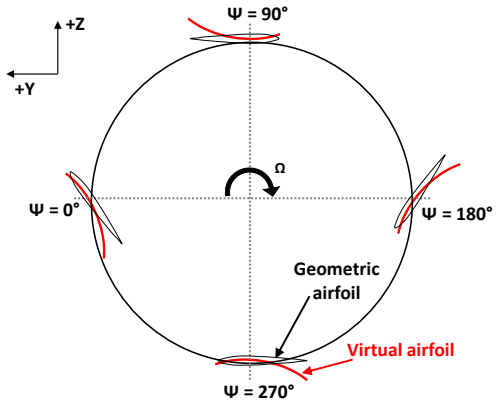

(a) Virtual airfoil.

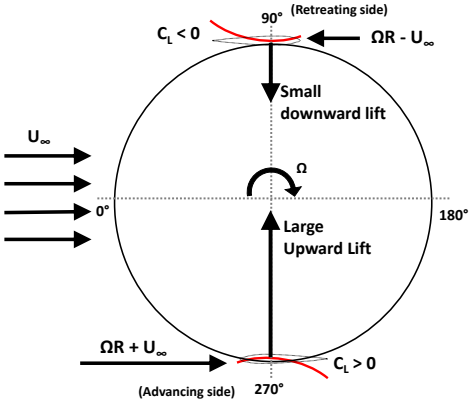

(b) Lift production.

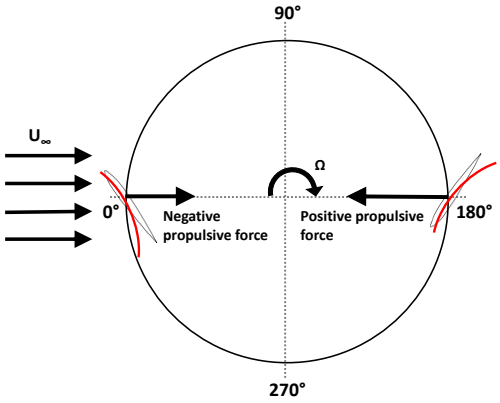

(c) Propulsive force production.

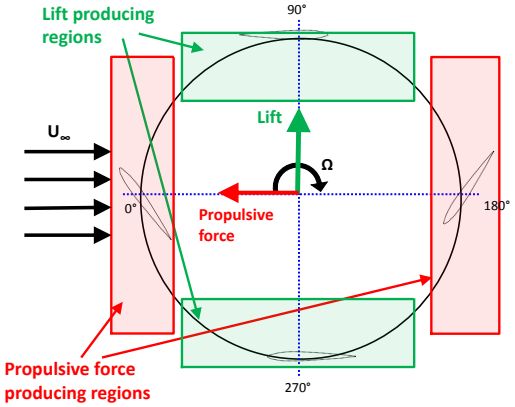

(d) Cyclorotor force producing regions.

Figure 5.5: Schematics showing effect of virtual camber on force production of cyclorotor in forward flight ($\phi = 90°$).

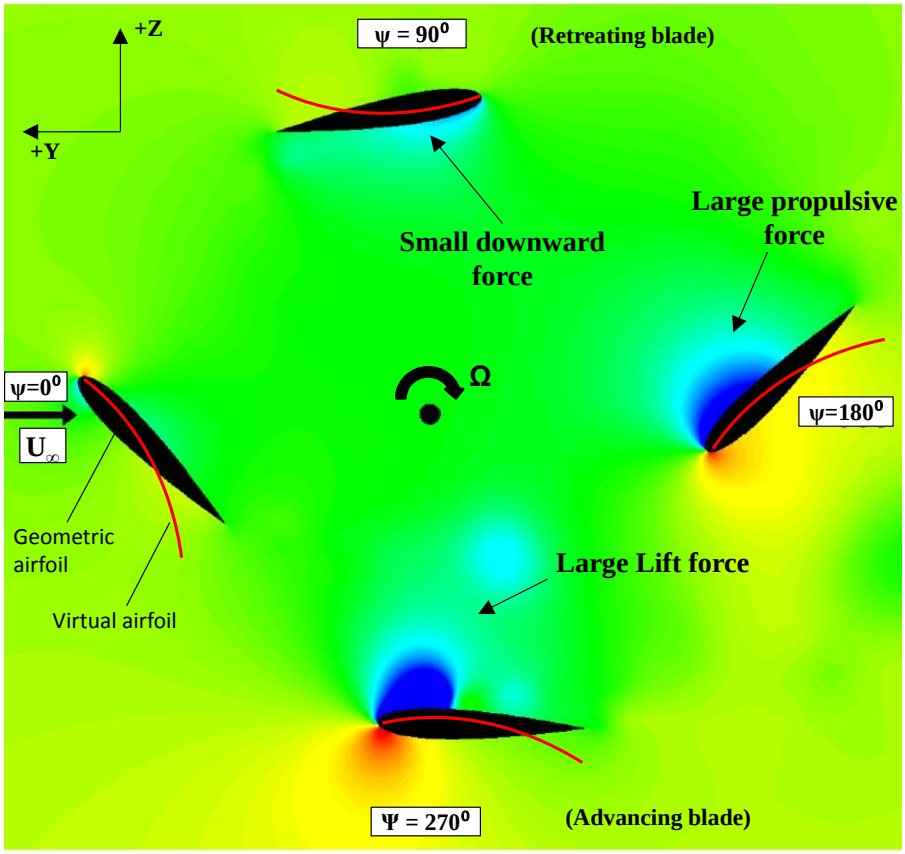

Figure 5.6: CFD predicted pressure contour plot at $U_\infty = 5\,m/s$, $\Omega = 1600\,\text{rpm}$, c/R=0.67.

of the force are no longer the same. This is clearly illustrated in Fig. 5.5b. The blade now moves in the same direction as the wind speed in the upper half of the trajectory (i.e. retreating side) and in the opposite direction to the freestream velocity in the lower half (i.e. advancing side). Thus, the blade tangential velocity at the top ($\psi = 90°$) is lower ($\Omega R - U_\infty$) compared to the tangential velocity at the bottom ($\psi = 270°$, $\Omega R + U_\infty$). Since lift is proportional to the square of velocity, the blade produces a larger upward lift force in the lower half compared to the downward lift in the upper half. As the forward speed increases, the difference in the magnitude of lift between the upper and lower halves becomes greater, resulting in a larger net left in the positive Z direction. This is clearly shown in the CFD predicted pressure contour plot in Fig. 5.6; there is a large low pressure region on the upper surface of the bottom blade, and a smaller low pressure region on the bottom surface of the top blade. The lift production becomes more pronounced with increasing c/R ratio due to the corresponding increase in virtual camber and incidence. This is clarified by the trends observed in Fig. 5.2.

Propulsive Force Production — Flow curvature effects also affect the propulsive force production. The schematic in Fig. 5.5c shows the effect of flow curvature on propulsive thrust production. It can be seen that at ψ=0° the blade operates at a large negative camber which could cause the blade to stall, reducing the propulsive force produced by the blade in the frontal section. At ψ=180°, the blade operates with large positive virtual camber, which increases the propulsive force produced by the blade. This is shown in the CFD pressure contour plot (Fig. 5.6). However, the difference in the blade tangential velocity at the front and

aft of the trajectory is relatively the same, unlike the top and bottom azimuthal locations. Therefore, increasing the c/R ratio may not lead to increased propulsive force production, and this is evidenced in the trends observed in Fig. 5.3.

Aerodynamic Power — The impact of flow curvature effects on rotor aerodynamic power is twofold: (1) the virtual camber and incidence vary the lift and propulsive forces of the cyclorotor, affecting rotor induced power, and (2) the virtual camber changes the zero-lift drag coefficient ($C_{d_{min}}$) of the airfoil and virtual incidence changes the effective geometric angle of attack of the airfoil, resulting in changes in the blade profile drag and hence rotor profile power.

5.2.1 Importance of Cyclorotor Direction of Rotation

In a conventional edgewise rotor, the direction of rotation does not impact rotor aerodynamic performance in hover or forward flight. In contrast, the direction of rotation is critical for a cyclorotor in forward flight. Based on Fig. 5.6, rotating in the opposite direction would lead to the advancing side on the upper half of the rotor and the retreating side on the lower half. The virtual camber and incidence of the blades would remain unchanged, and therefore the downward force produced by the upper blade in would be greater in magnitude compared to the upward lift of the lower blade. At high forward speeds, the result will be a large net downward lift of the cyclorotor. This is an important aspect of the cyclorotor in forward flight, and has not been explicitly discussed in previous studies. As a general design guideline for a MAV, therefore, the cyclorotor should operate in the counter-clockwise direction

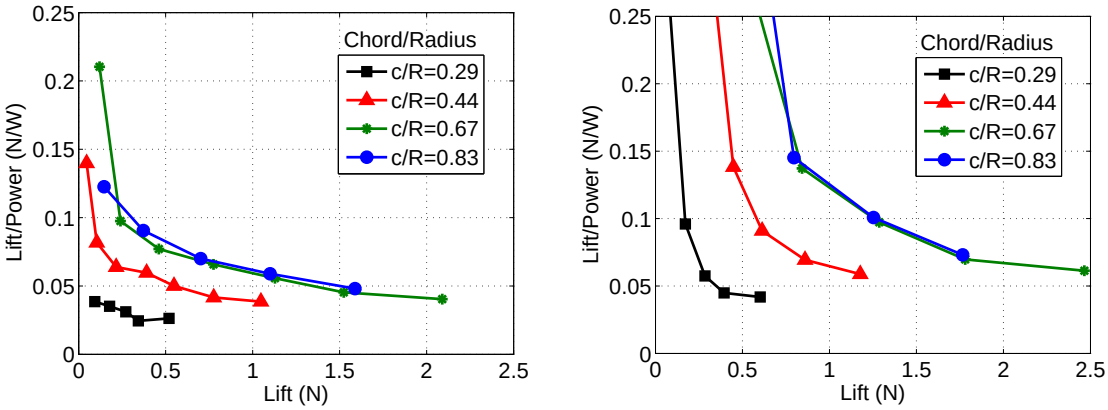

(a) Wind speed = 5 m/s

(b) Wind speed = 9 m/s

Figure 5.7: Lift-per-unit-power versus lift for different c/R ratios with pitching axis at 0.25c.

relative to the freestream velocity (i.e. with a 'backspin'), with the advancing blade on the bottom and retreating blade on the top of the circular trajectory.

5.2.2 Optimum c/R Ratio in Forward Flight

Figure 5.7 shows the cyclorotor lift-per-unit-power as a function of lift for different chord/radius ratios at two different freestream velocities ($U_\infty = 5, 9\, m/s$). For each c/R ratio, the lift was varied by changing the rotational speed. Figure 5.7a shows that for a constant value of lift, the lift-per-unit-power of the cyclorotor improves with increasing values of c/R, although the increase from a c/R of 0.67 to 0.83 is minimal. The same trend is shown for the higher freestream velocity (Fig. 5.7b). However, comparing Figs. 5.7a and 5.7b, the overall lift-per-unit power increases with forward speed. These results suggest that the optimum c/R ratio for maximizing the lift-per-unit power is between 0.67 and 0.83, and is not a strong

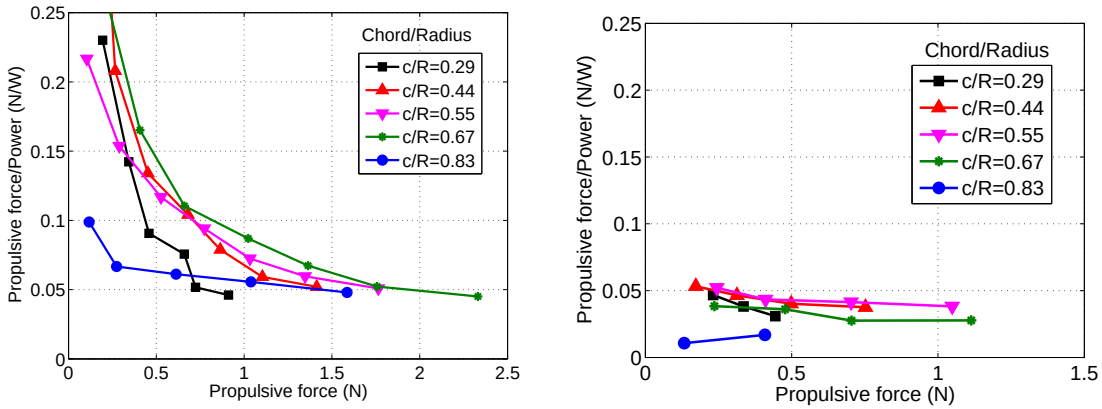

(a) Wind speed = 5 m/s

(b) Wind speed = 9 m/s

Figure 5.8: Propulsive force-per-unit-power versus propulsive force for different c/R ratios with pitching axis at 0.25c.

function of forward velocity.

Figure 5.8 shows the cyclorotor propulsive force-per-unit-power as a function of propulsive force for the two freestream velocities. The propulsive force per unit power increases with chord/radius ratio, but the optimal c/R ratio in this case is dependent on the forward speed. For the lower forward speed of 5 m/s (Fig. 5.8a), the propulsive force-per-unit-power at a constant value of propulsive force increases up to a c/R ratio of c/R of 0.67, and then decreases significantly for a c/R ratio of 0.83. For the higher forward speed of 9 m/s (Fig. 5.8b), however, the propulsive force-per-unit-power increases up to a lower c/R ratio of 0.55. In fact, the propulsive force/power for c/R ratio of 0.83 was lower compared to a c/R ratio of 0.29. The decreased propulsive force producing efficiency of the cyclorotor at high c/R ratios and forward speeds may be due to the large negative propulsive forces produced by the blades along the frontal half of the rotor ($\psi = 270°$ to $90°$). Therefore, in regard

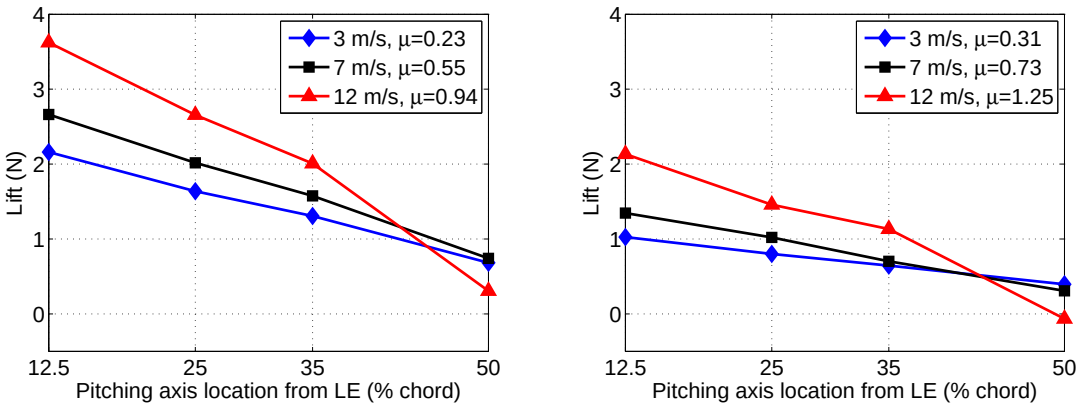

(a) Rotational speed = 1600

(b) Rotational speed = 1200

Figure 5.9: Lift versus chord-wise pitching axis location at constant wind speeds ($c/R = 0.67$).

to propulsive force-per-unit-power, the optimum c/R ratio depends on the forward speed and may be between a c/R of 0.55 and 0.67.

5.3 Effect of Blade Pitching Axis Location

The previous section examined the combined effects of virtual camber and incidence on cyclorotor aerodynamic performance. The chord/radius ratio was varied, and the blade pitching axis location was fixed at quarter-chord. The goal of the current section is to isolate and examine the effects of virtual incidence on rotor aerodynamic performance. By varying the blade chord-wise pitching axis location, the virtual incidence can be changed without affecting the virtual camber. Thus, experiments were conducted at a fixed c/R ratio of 0.67 ($c = 2\,\text{in}$, $R = 3\,\text{in}$) at four different pitching axis locations: 12.5%, 25%, 35%, and 50% chord.

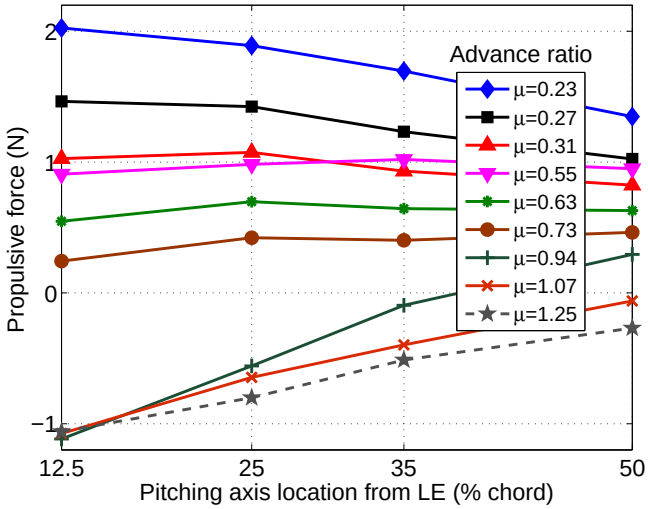

Figure 5.10: Propulsive force versus chord-wise pitching axis location at different advance ratios ($c/R = 0.67$).

Figure 5.9 shows the variation in lift with pitching axis location at different wind speeds (3, 7 and 12 m/s) at two different rotational speeds (Ω = 1600 and 1200 rpm). At the higher rotational speed of 1600 rpm (Fig. 5.9a), the lift decreases linearly as the pitching axis location is moved away from the leading edge. At a constant pitching axis location, the lift increases with increasing forward speed (i.e. advance ratio). The same trends are shown for a lower rotational speed of 1200 rpm (Fig. 5.9b), although the overall lift values are lower in magnitude.

The results in Fig. 5.9 be explained as follows. As the pitching axis location is moved away from the leading edge, there is a corresponding decrease in the virtual incidence angle experienced by the blades. At a pitching axis location of 50% chord, the virtual incidence angle is zero. Decreasing the virtual incidence angle reduces the effective angle of attack of the blades, leading to decreased force production.

This explains why the lift force decreases as the pitching axis location is moved from 12.5% to 50% chord. Furthermore, the lift is greater at higher advance ratios for a given pitching axis location due to reasons discussed in the previous section. As the advance ratio increases, the contribution of the upward lift in the lower half of the rotor is greater than the downward lift in the upper half, resulting in an overall increase in lift. From a cyclorotor design perspective, the results in Fig. 5.9 show that pitching the blades closer to the leading edge (high virtual incidence) will maximize lift production at a given advance ratio.

Figure 5.10 shows the variation in propulsive force with pitching axis location for a wide range of advance ratios. At low advance ratios ($\mu < 0.31$), the propulsive force decreases as the pitching axis location is moved away from the leading edge, similar to the behavior of lift. At moderate advance ratios ($\mu = 0.31$ to 0.73), the propulsive force is relatively insensitive to variations in the pitching axis location. At high advance ratios ($\mu > 0.73$), the propulsive force actually increases as the pitching axis is moved away from the leading edge. These results suggest that the role of virtual incidence on the propulsive force is dependent on the advance ratio.

Figure 5.11 shows the variation in power with pitching axis location for the same cases as in Fig. 5.9. At the higher rotational speed of 1600 rpm (Fig. 5.11a), the power decreases in a parabolic fashion as the pitching axis location is moved away from the leading edge. At a high advance ratio of $\mu = 0.94$, the power begins to increase as the pitching axis is moved from 35% to 50% chord. These trends are generally the same for the lower rotational speed of 1200 rpm (Fig. 5.11b), although the increase in power for the highest advance ratio tested occurs beyond a pitching

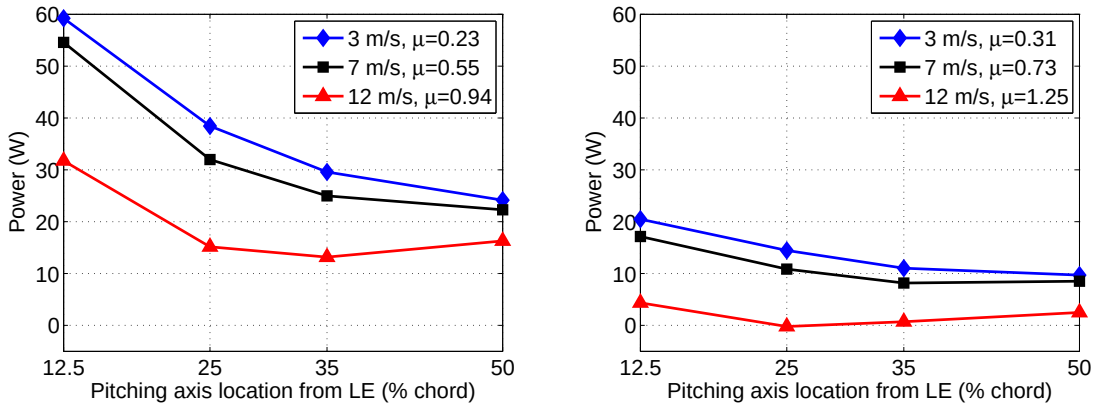

(a) Rotational speed = 1600

(b) Rotational speed = 1200

Figure 5.11: Power versus chord-wise pitching axis location at constant wind speeds ($c/R = 0.67$).

axis location of 25% chord. These trends suggest that the pitching axis location for achieving minimum power is between 35% and 50% chord for low to moderate advance ratios.

5.3.1 Optimum Pitching Axis Location in Forward Flight

Figure 5.12 shows the rotor lift-per-unit-power as a function of lift for different chord-wise pitching axis locations at two forward speeds ($U_\infty = 3$ and 7 m/s). For both forward speeds, pitching axis locations of 12.5%, 25% and 35% chord do not significantly impact the lift producing efficiency of the cyclorotor. In both cases, a pitching axis location of 50% chord leads a very low lift producing efficiency, although a pitching axis location of 35% chord also leads to a slight decrease for the 7 m/s case. Therefore, in regard to the lift producing efficiency of the cyclorotor, the optimum pitching axis location may be between 12.5% and 25% chord.

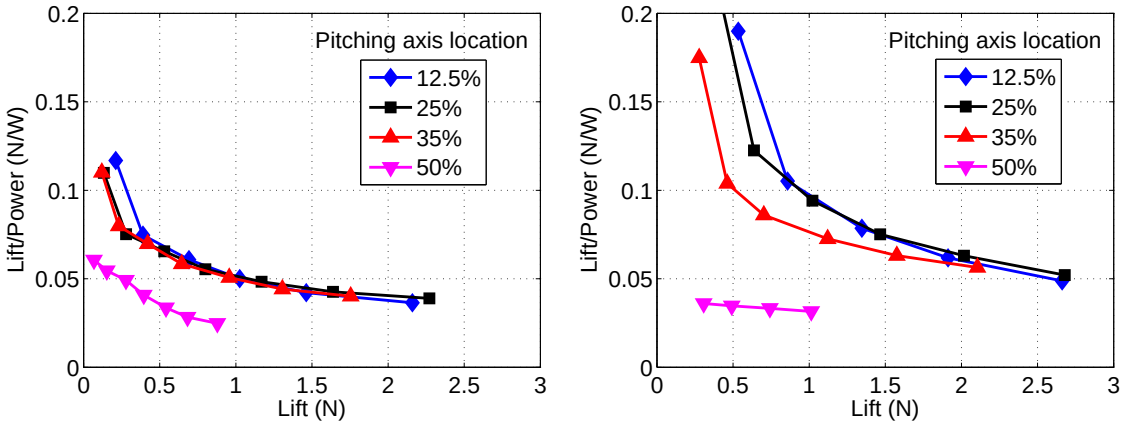

(a) Wind speed = 3 m/s (b) Wind speed = 7 m/s

Figure 5.12: Lift/power versus lift for different pitching axis locations ($c/R = 0.67$).

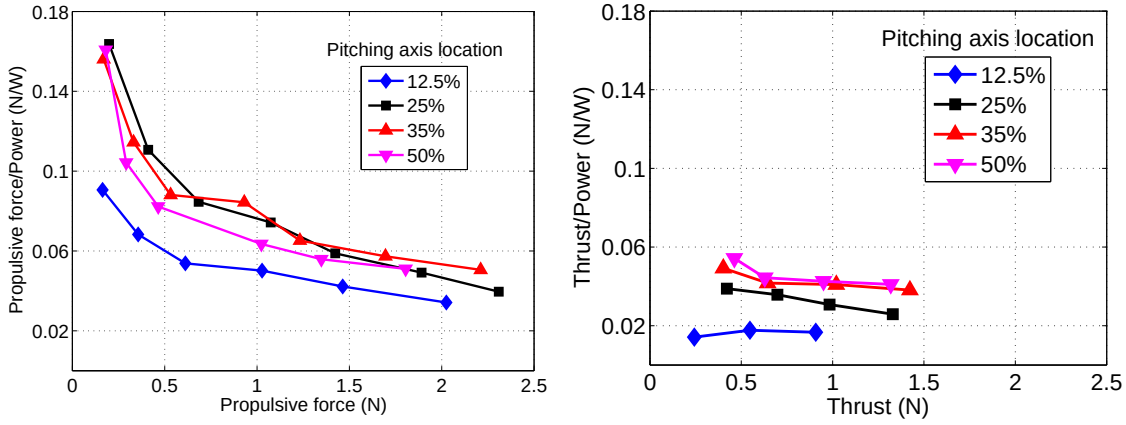

(a) Wind speed = 3 m/s (b) Wind speed = 7 m/s

Figure 5.13: Propulsive force/power versus propulsive force for different pitching axis locations ($c/R = 0.67$).

Figure 5.13 shows the rotor propulsive force-per-unit-power as a function of propulsive force. For both forward speeds, the pitching axis location has a strong impact on the propulsive force producing efficiency of the cyclorotor. For the 3 m/s wind speed case (Fig. 5.13a), the optimum pitching axis location of is between 25% and 35%. For the 7 m/s case (Fig. 5.13b), the optimum pitching axis location is farther from the leading edge between 35% and 50% chord. For both cases, a pitching axis location of 12.5% chord significantly decreases the propulsive force producing efficiency of the cyclorotor. The results in Fig. 5.13 show that the pitching axis location has a strong impact on the propulsive force producing efficiency of the cyclorotor, with a pitching axis location between 25% and 50% chord leading to improved values of propulsive force-per-unit-power.

5.4 Summary

The current Chapter was focused on examining the role of flow curvature effects (virtual camber and incidence) on cyclorotor aerodynamic performance. Since the flow curvature effects are strongly dependent on the rotor chord/radius ratio and pitching axis location, two parameters were systematically varied to understand their impact on cyclorotor lift, propulsive force and power. Experiments were conducted at different freestream velocities and rotational speeds, with the blade pitching kinematics held constant. The specific conclusions from these experiments can be summarized as follows:

1. **Flow curvature effects** and differences in aerodynamic velocities between

the upper (retreating) and lower (advancing) halves of the cyclorotor were identified as an important part of lift production. Unlike a conventional edgewise rotor, the direction of rotation of a cyclorotor becomes extremely important in forward flight. In order to produce a net positive lift, the cyclorotor must operate in the counter-clockwise direction if the freestream velocity is from left to right (i.e. a back-spin with respect to the forward speed). A forward-spin would produce a negative or downward lift force.

2. Increasing the **chord/radius (c/R) ratio** (increases virtual camber and incidence) led to a linear increase in lift-per-unit-blade area at a fixed rotational speed and forward velocity, but did not significantly impact propulsive force-per-unit-blade area or power-per-unit-blade area. The lift and propulsive force producing efficiency of the cyclorotor improved with increasing c/R ratio at a constant rotational speed and forward speed. The lift-per-unit-power did not depend on the forward velocity, whereas the propulsive force-per-unit-power was a function of forward velocity. The optimum c/R ratio for maximum lift-per-unit-power was between 0.67 and 0.83. For maximum propulsive force-per-unit-power, the optimum c/R ratio was 0.67 at 5 m/s and 0.55 at 9 m/s.

3. Moving the **blade pitching axis** away from the leading edge (decreases virtual incidence) decreased the rotor lift and power; however, the effect on propulsive force production depended on the advance ratio. Moving the pitching axis away from the leading edge decreased propulsive force at low advance ratios ($\mu < 0.31$), but increased propulsive force at high advance ratios ($\mu > 0.73$).

The pitching axis location did not significantly affect cyclorotor lift producing efficiency, but had a strong impact on propulsive force producing efficiency. The optimum pitching axis location for maximum propulsive force-per-unit-power was between 25% and 35% chord from the leading edge.

Chapter 6: Concluding Remarks

6.1 Overview

This dissertation has explored the forward flight performance of a cycloidal rotor using two distinct approaches. The first approach was to examine the time-averaged aerodynamic force and power measurements through systematic parametric studies, and use these results to determine trimmed, level flight performance of the cyclorotor. The three blade kinematic parameters examined were the blade pitch amplitude (θ_A), pitch phase angle (ϕ) and mean pitch angle (θ_M). The effects of each parameter on rotor lift, propulsive force and power were investigated at different advance ratios. The results were then interpolated to determine the power consumption, lift to drag ratio and control input requirements necessary to maintain trimmed, level flight at different forward speeds. A 500 gram twin-cyclocopter micro air vehicle was used as a reference for deriving the baseline case in these studies. Finally, the effect of rotor geometry (c/R ratio and blade pitching axis location) were varied to examine the impact of flow curvature effects.

The second approach was focused on understanding the underlying principles of force production on the cyclorotor. Flow field studies, which comprised of flow visualization and particle image velocimetry (PIV) studies, were conducted to fulfill

this objective. Both the time-averaged and phase-averaged flow field of the cycloro-tor were analyzed. The distribution of aerodynamic forces and power along the rotor azimuth was explained, and the role of unsteady aerodynamics on rotor force production was discussed. The experimental PIV results were correlated with both time-averaged force measurements as well as CFD-predicted instantaneous blade forces from previous studies.

Together, the two approaches of this work not only provided an in-depth understanding of the operating principles of the cyclorotor in forward flight, but also established an important framework which may help guide the future development of an efficient, forward-flight capable cyclocopter micro air vehicle.

6.2 Conclusions of the Study

6.2.1 Experimental Performance Studies

6.2.1.1 Effect of Blade Pitching Kinematics

1. The pitch phase angle (ϕ) can be effectively used to vary the rotor lift and propulsive force components at low to moderate advance ratios, with minimal impact on rotor power consumption. At high advance ratios, however, the range in which the phase angle can be varied is more limited. Operating at extremely large phase angles decreases the propulsive force and increases power consumption.

2. The blade pitch amplitude (θ_A) is also an effective parameter for varying the rotor lift and propulsive force components at low to moderate advance ratios.

However, the pitch amplitude can only be used to vary the propulsive force component at high advance ratios, where the rotor must operate at large phase angles. Furthermore, unlike the phase angle, the pitch amplitude significantly impacts rotor power consumption and therefore plays an important role in rotor propulsive efficiency.

3. The mean pitch angle (θ_M) introduces an asymmetry in the pitching kinematics of the cyclrotor. Operating at a positive mean pitch angle can be beneficial at low to moderate advance ratios in regard to power consumption, although there is a slight corresponding decrease in lift production.

6.2.1.2 Rotor Performance in Trimmed, Level Flight

1. The lift per unit power (at constant propulsive force) of the cyclorotor improved with both increasing advance ratio and increasing values of lift. The propulsive force per unit power (at constant lift) remained relatively constant with increasing advance ratio. These findings suggest that the cyclorotor has an added advantage in lift production at high forward speeds, whereas its ability to produce propulsive force for a given amount of power remains unaffected.

2. For a given forward speed, the effect of increasing values of lift is to increase rotor power requirements (straight and level flight). However, the relative differences in power for different lift values decrease at high forward speeds due to the increased lift producing efficiency of the rotor at high speeds. This result can be important, for example, when considering increased payload capacity for a cyclocopter MAV

with a mission profile that requires high forward speeds and minimal flight time in hover or low speeds.

3. The effect of increasing values of propulsive force is to increase rotor power requirements at a constant forward speed (straight and level flight). At high forward speeds, the pitch amplitude is a more effective control parameter for achieving larger propulsive force values than phase angle.

4. Decreasing the operating rotational speed (straight and level flight) led to significant reductions in power consumption at a given forward speed. This trend is attributed to the reduction in profile power (cube of rpm), which can be significant for MAVs. However, the minimum possible rotational speed is governed by the onset of blade stall. At the lowest rotational speed tested (1400 rpm), the high operating pitch amplitudes required to maintain straight and level flight lead to increased power consumption at forward speeds greater than 9 m/s.

5. Asymmetric pitching kinematics can allow for more efficient forward flight compared to symmetric pitching kinematics. For a trimmed rotor at a constant rotational speed of 1600 rpm, the power consumption for the asymmetric case was 28% and 47% lower than the symmetric case at speeds of 3 and 9 m/s. However, the primary limitation of increasingly asymmetric pitching kinematics is the significant reduction in lift production. Thus, asymmetric pitching kinematics may not be suitable for trimming the rotor at high values of lift (i.e. increased payloads and climb maneuvers).

6. The maximum forward speed tested for the isolated cyclorotor in straight and level flight was 13 m/s (25 kt). At this speed, the rotor operated at 1740 rpm

(advance ratio = 0.94) and was able to maintain sufficient lift (2.82 N) that is required for the twin-cyclocopter MAV. The power consumption at this speed was 36% lower than in hover.

6.2.1.3 Effect of Rotor Geometry

1. The direction of rotation of the cyclorotor with respect to the direction of flight is extremely important due to flow curvature effects. The rotor must rotate such that the advancing blade is on the bottom and the retreating blade is on the top (i.e. a backspin with respect to the direction of flight). Rotating in the opposite direction would cause a large downward lift force.

2. Increasing the chord/radius (c/R) ratio, which in turn increases virtual camber and incidence, improves both the lift-per-unit-power and propulsive force-per-unit-power of the cyclorotor at a constant rotational speed and forward velocity. The optimum c/R ratio for maximum lift-per-unit-power was independent of forward velocity, but the maximum propulsive force-per-unit-power was a function of forward velocity.

3. Varying the distance between the blade pitching axis and leading edge, which affects virtual incidence, has a strong impact on the propulsive force-per-unit-power, but did not significantly impact lift-per-unit-power. The optimum pitching axis location for maximum propulsive force efficiency was between 25% and 35% from the leading edge.

6.2.2 Flow Field Studies

1. The flow velocity decreases in magnitude as it passes across the upper-frontal quadrant ($\psi = 0°$ to $\psi = 90°$) of the cyclorotor. This is attributed to power extraction by the blades in this region. The effect of increasing advance ratio is to increase power extraction in the frontal half.

2. The primary force producing region of the cyclorotor lies in the lower-aft section of the rotor azimuth ($\psi = 180°$ to $\psi = 270°$). An aerodynamic analysis based on PIV time-averaged flow field measurements revealed the blades operate in a high dynamic pressure environment with a high effective angle of attack in this region. The significant momentum addition by the blades leads to high flow velocities across the lower half of the rotor cage.

3. Constructive blade-wake interactions appear to play an important role in enhancing the lift and propulsive force generation of the blades in the rear half of the rotor azimuth ($\psi = 150°$ and $\psi = 270°$). The downstream blade encounters two blade-wake interactions: one with its own wake and another with the wake of the upstream blade. The rotational flow induced by the vortices located along the blade wakes accelerates the flow over the upper surface of the blade.

6.3 Recommendations for Future Work

The research presented in this dissertation is a small step towards the ultimate goal, which is the development of an efficient cyclocopter micro air vehicle capable of hover and high speed flight. Although the current work has provided many insights

into the cyclorotor aerodynamic performance and the underlying flow physics of force production in forward flight, there remain many opportunities for further study and improvements.

1. **Cyclocopter MAV development:** The control input requirements presented in this work should be implemented and tested on a cyclocopter micro air vehicle such as the one shown in Chapter 3 (Fig. 3.10). Wind tunnel tests can be performed on the vehicle at various speeds, followed by free-flight tests. A good starting point in the control strategy would be to use the pitch amplitude (θ_A) and pitch phase angle (ϕ) as the two control variables. The pitching mechanism would require rotating servos for phase angle control and linear servos to change the eccentricity offset for pitch amplitude control.

2. **Performance studies**: More time-averaged experimental studies can be conducted towards an optimized cyclorotor configuration that provides a balanced aerodynamic performance between hover and forward flight. The cyclorotor used in the current research was optimized for hover only, and thus, further improvements in power consumption could be achieved through variations in rotor geometric and blade kinematic parameters.

3. **Flow field studies**: The PIV and CFD studies in the current research clearly showed a large non-uniformity in the distribution of forces along the rotor azimuth. This may be disadvantageous at high forward speeds, where the blades may begin to stall in the highly loaded azimuthal regions. Thus, experimental and computational tools (PIV and CFD) should be used to examine the effects of asymmetric pitching kinematics on the distribution of forces. Another important

study would be to examine the effects of geometrically cambered blades to improve aerodynamic performance through flow curvature effects.

4. **Study of vibrations:** High vibratory loads are a key limiting factor for the achievement of high speed flight for conventional helicopter rotors. Thus, an important aspect of future cyclorotor research should be the examination of vibratory loads in high speed flight and on what can be done to improve them.

5. **Cyclorotor aeroacoustics:** A very important potential advantage of the cycloidal rotor could lie in its reduced acoustic signature. For a given value of thrust, the cycloidal rotor can operate at significantly lower tip speeds in comparison to a conventional rotor of the same scale. Experimental acoustic tests need to be performed to quantify and compare the noise levels between a cycloidal rotor and a conventional rotor of the same scale.

Chapter A: Appendix A: Four-bar Pitching Mechanism

A.1 Four-bar Analysis

L_1 = Rotor radius

L_2 = Eccentric offset

L_3 = Pitch link length

L_4 = Distance between blade pitching axis and linkage attachment point

$$a = sin(\psi) \tag{A.1}$$

$$b = cos(\psi) + \frac{L_1}{L_2} \tag{A.2}$$

$$c = \frac{L_1}{L_4} cos(\psi) + \frac{L_1^2 + L_2^2 + L_4^2 - L_3^2}{2L_2L_4} \tag{A.3}$$

$$\theta(\psi) = 2\arctan(\frac{a - \sqrt{a^2 + b^2 - c^2}}{b + c}) \tag{A.4}$$

Note: For all cases, the rotor radius (L_1) was constant at 3 in, and the distance between the pitching axis and pitch link attachment (L_4) was 0.4331 in.

Table A.1a: Linkage lengths used for symmetric pitching.

Pitch amplitude (θ_A)	Linkage length (L_3)	Eccentric offset (L_2)
$\pm 25°$	3.0260 in	0.1811 in
$\pm 30°$	3.0260 in	0.2160 in
$\pm 35°$	3.0210 in	0.2470 in
$\pm 40°$	3.0158 in	0.3050 in
$\pm 45°$	3.0158 in	0.3300 in
$\pm 50°$	3.0158 in	0.3540 in
$\pm 55°$	3.0100 in	0.3730 in

Table A.1b: Linkage lengths used for asymmetric pitching ($\theta_{pk-to-pk} = 70°$).

Mean pitch angle (θ_M)	Linkage length (L_3)	Eccentric offset (L_2)
$-5°$	3.0490 in	0.2470 in
$0°$	3.0210 in	0.2470 in
$5°$	2.9900 in	0.2470 in
$10°$	2.9600 in	0.2470 in

Chapter B: Appendix B: Forward Flight Experimental Setup

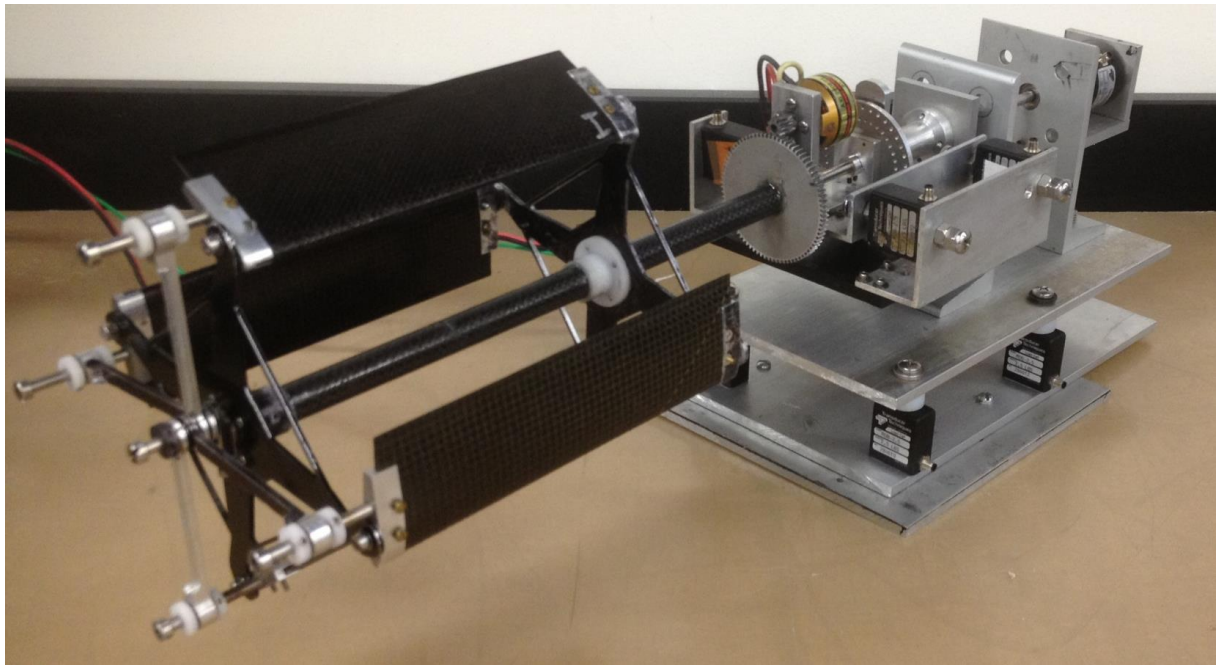

Figure B.1: Forward flight setup.

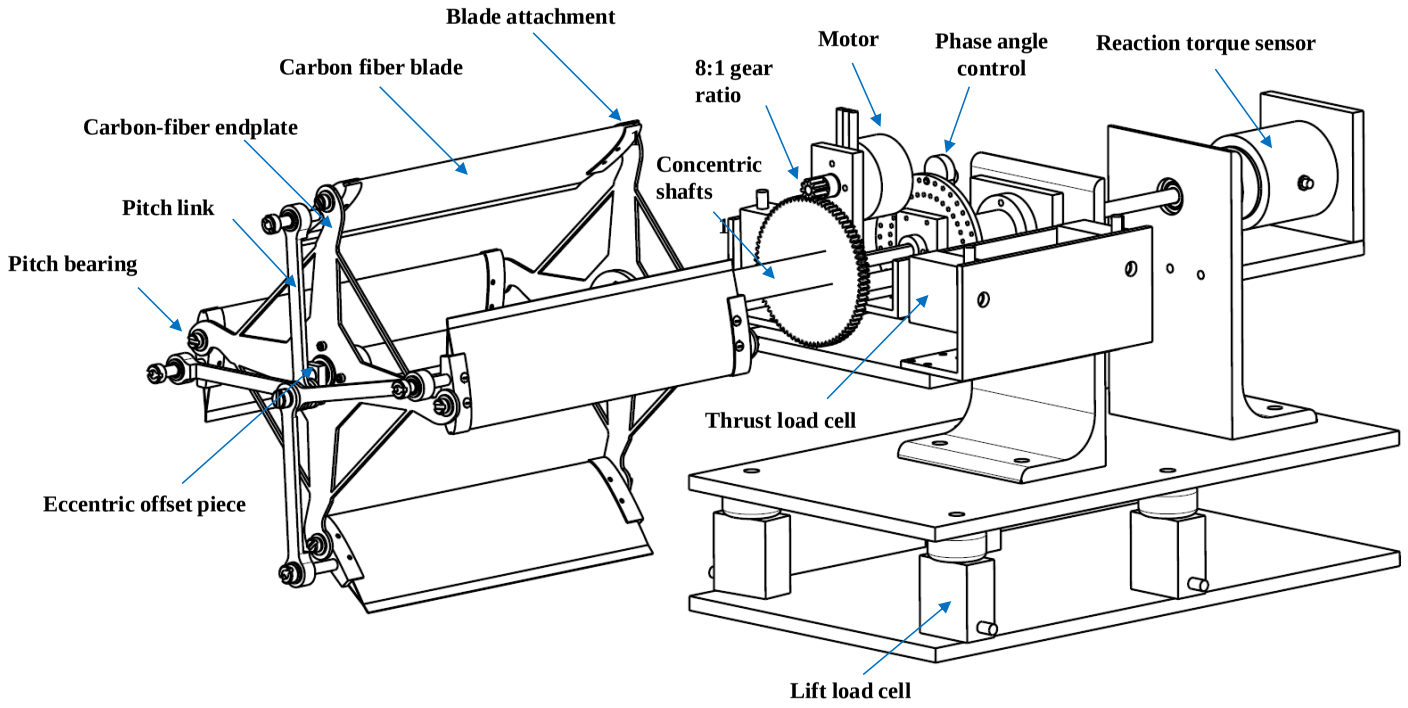

Figure B.2: 3-dimensional drafting view of forward flight setup.

NOTE: RTS-10 shown in image (RTS-100 used)

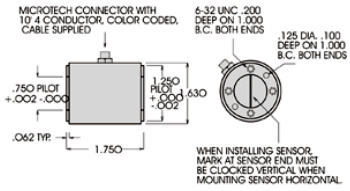

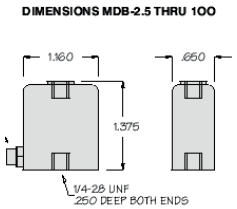

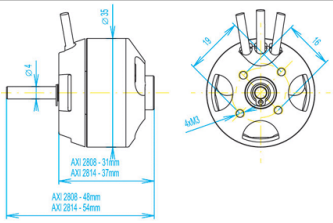

Torque reaction sensor (Transducer Techniques RTS-100)	
Rated output (R.O.)	1.5 mV/V nominal
Nonlinearity	0.1% of R.O.
Nonrepeatability	0.05% of R.O.
Hysteresis	0.1% of R.O.
Excitation Voltage	10 VDC
Safe overload	150% of R.O.
Maximum capacity	100 oz-in

Load cell (Transducer Techniques MDB-2.5)	
Type	Compresison/tension
Rated output (R.O.)	2 mV/V nominal
Nonlinearity	0.05% of R.O.
Nonrepeatability	0.05% of R.O.
Hysteresis	0.05% of R.O.
Excitation Voltage	10 VDC
Safe overload	150% of R.O.
Maximum capacity	2.5 lbs

Motor specifications (AXI 2808/24)	
No. of cells	6 – 10 (2 - 3 Li-Poly)
RPM/V	1190 RMP/V
Max. efficiency	82%
Max. efficiency current	6 - 15 A (>75%)
No load current / 10 V	1 A
Current capacity	22 A/60 s
Internal Resistance	115 mohm
Weight with cables	76 g

Figure B.3: Electric motor and load cell information.

Bibliography

[1] Mueller, T. J., "On the Birth of Micro Air Vehicles," *International Journal of Micro Air Vehicles*, Vol. 1, (1), March 2009, pp. 1–12.

[2] McMichael, J. M., and Francis, M. S., "Micro Air Vehicles — Toward a New Dimension in Flight," Technical Report, Defense Advanced Research Projects Agency, Aug 7, 1997. Available from: `http://www.fas.org/irp/program/collect/docs/mav_auvsi.htm` [cited Sept 1 2013].

[3] Pines, D., and Bohorquez, F., "Challenges Facing Future Micro-Air-Vehicle Development," *Journal of Aircraft*, Vol. 43, (2), March/April 2006, pp. 290–305.

[4] Mueller, T. J., "Aerodynamic Measurements at Low Reynolds Numbers for Fixed Wing Micro Air Vehicles," Presented at the RTO AVT/VKI Special Course on Development and Operation of UAVs for Military and Civil Applications, VKI, Belgium, September 13–17, 1999.

[5] Chopra, I., "Hovering Micro Air Vehicles: Challenges and Opportunities," Proceedings of American Helicopter Society Specialists' Conference, International Forum on Rotorcraft Multidisciplinary Technology, October 15–17, 2007, Seoul, Korea.

[6] McMasters, J. and Henderson, M., "Low-Speed Single Element Airfoil Synthesis," Technical Soaring, Vol. 6, 1980, pp. 1–21.

[7] Meuller, T. J. and DeLaurier, J. D., "Aerodynamics of Small Vehicles," Annual Review of Fluid Mechanics, 2003, (35) pp. 89–111,.

[8] Spadaccini, C.M., Zhang, X., Cadou, C.P., Miki, N. and Waitz, I.A.,"Preliminary Development of a Hydrocarbon-fueled Catalytic Micro-

Combustor," Sensors and Actuators A: Physical, Vol. 103, No. 1, January 2003, pp. 219–224(6).

[9] "Aerovironment Wasp III Technical Data Sheet," World-Wide Web document, http://www.avinc.com/uas/adc/wasp/, [cited September 6, 2013].

[10] "PD-100 Personal Reconnaissance System (PRS) Specifications," World-Wide Web document, http://www.proxdynamics.com/products/pd_100_prs/, [cited November 18, 2013].

[11] Leishman, J. G., *Principles of Helicopter Aerodynamics*, Cambridge University Press, New York, NY, 2006, pp. 229, 280, 334–337.

[12] Ramasamy, M., Johnson, B., and Leishman, J.G., "Understanding the Aerodynamic Efficiency of a Hovering Micro Rotor," *Journal of the American Helicopter Society*, Vol. 53 (4), October 1, 2008, pp. 412–428.

[13] Shyy, W., Lian, Y., Tang, J., Viieru, D., and Liu, H., *Aerodynamics of Low Reynolds Number Flyers,* Cambridge University Press, New York, NY, 2008.

[14] Birch, J. M., Dickson, W. B., and Dickinson, M. H., "Force Production and Flow Structure of the Leading Edge Vortex on Flapping Wings at High and Low Reynolds Numbers," *The Journal of Experimental Biology,*, 2004, (207) pp. 1063–1072, .

[15] Seshadri, P., "Biomimetic Insect Flapping Wing Aerodynamics and Controls for Micro Air Vehicles," Master of Science Thesis, University of Maryland, College Park, 2011.

[16] Keennon, M., Klingebiel, K., Won, H., and Andriukov, A., "Development of the Nano Hummingbird: A Tailless Flapping Wing Micro Air Vehicle," 50^{th} AIAA Aerospace Sciences Meeting, , Nashville, TN, January 9–12, 2012.

[17] Benedict, M., Jarugumilli, T., and Chopra, I., "Experimental Investigation of the Effect of Rotor Geometry and Blade Kinematics on the Performance of a MAV-scale Cycloidal Rotor," Proceedings of the American Helicopter Society Specialists' Meeting on Unmanned Rotorcraft and Network Centric Operations, Tempe, AZ, January 25–27, 2011.

[18] Shavrov, V., *History of Aircraft Construction in the USSR to 1938*, Mashinostroenie (Moscow), Vol. 1, pp. 39–40, 1985.

[19] "Cyclogyro History," World-Wide Web document, http://rotoplan.narod.ru/history_e.htm, [cited September 6, 2013].

[20] Boirum, C. G. and Post, S. L., "Review of Historic and Modern Cyclogyro Design," Proceedings of the 45^{th} AIAA Joint Propulsion Conference and Exhibit, Denver, CO, August 2–5, 2009.

[21] Kirsten, F. K., "Cycloidal Propulsion Applied to Aircraft," *Transactions of the American Society of Mechanical Engineers,* Vol. 50, No. AER-50-12, 1928, pp. 25–47.

[22] Sachse, H., "Kirsten-Boeing Propeller," NACA Technical Report No. 351, Washington D.C., January 14, 1926.

[23] "Voith Schneider Propeller," World-Wide Web document, `http://www.voith.com/en/index.html`, [cited September 6, 2013].

[24] Schneider, E., "Blade Wheel Propeller Particularly for Watercraft," Patent 2,291,062, 28 July 1942.

[25] Bartels, Jens-Erk, and Dirk Jrgens, *The Voith Schneider Propeller: Current applications and new developments*, Technical report, Voith Turbo Marine GmbH, 2006.

[26] Strandgren, C. B., "The Theory of the Strandgren Cyclogiro," NACA Technical Report Vol. 41, No. 7, Washington D.C., July 1933.

[27] Wheatley, J., "Simplified Aerodynamic Analysis of the Cyclogiro Rotating-Wing System," Technical Report 467, National Advisory Committee for Aeronautics, August 1933.

[28] Wheatley, J. B., and Windler, R., "Wind-Tunnel Tests of a Cyclogiro Rotor," NACA Technical Notes No. 28, May 1935.

[29] Eastman., F., Cottas, N., Barkheines, G., "Wind Tunnel Tests on a High Pitch Cyclogyro," University of Washington Aeronautical Laboratory Report 191-A, 1943.

[30] Eastman., F., "The Full Feathering Cyclogiro," University of Washington Aeronautical Laboratory Report No. 317, December 1945.

[31] Lee, J., Eberhardt, D.S., Breidenthal, R.E. and Bruckner, A.P., "A History of the University of Washington Department of Aeronautics and Astronautics 1917–2003," Department of Aeronautics and Astronautics, University of Washington, Seattle, WA, May 27, 2003.

[32] Sharpe, T. H., "Lift Augmenting Device for Aircraft," Patent 4194707, 25 March 1980.

[33] Chabonat, M., "Propulsive Lifting Rotors," Patent 4210299, 1 July 1980.

[34] Crimmins, A. G., "Cyclorotor Composite Aircraft," Patent 4482110, 13 November 1984.

[35] Gerhardt, H. A., "Paddle Wheel Rotorcraft," Patent 5265827, 30 November 1993.

[36] Gibbens, R., Boschma, J., and Sullivan, C., "Construction and Testing of a New Aircraft Cycloidal Propeller," Paper AIAA-1999-3906, AIAA 13th Lighter-Than-Air Systems Technology Conference Proceedings, Norfolk, VA, June 28–July 1, 1999.

[37] Boschma, J. H, "Modern Aviation Applications for Cycloidal Propellers," Proceedings of the 1^{st} AIAA Aircraft Technology Integration and Operations Forum, Los Angeles, CA. pp. AIAA-2001-5267, 2001.

[38] McNabb, M. L., "Development of a Cycloidal Propulsion Computer Model and Comparison with Experiment," Master of Science Thesis, Mississippi State University, Mississippi, December 2001.

[39] Kim, S., Yun, C., Kim, D., Yoon, Y., and Park, I., "Design and Performance Tests of Cycloidal Propulsion Systems," Paper AIAA-2003-1786, 44th AIAA/ASME/ASCE/AHS/ASC Structures, Structural Dynamics, and Materials Conference, Norfolk, Virginia, April 710, 2003.

[40] Yun, C. Y., Park, I. K., Hwang, I. S., and Kim, S. J., Thrust Control Mechanism of VTOL UAV Cyclocopter with Cycloidal Blades System, *Journal of Intelligent Material Systems and Structures,* Vol. 16, No. 11–12, December 2005, pp. 937–943.

[41] Yun, C. Y., Park, I. K., Lee, H. Y., Jung, J. S., Hwang, I. S., and Kim, S. J., "Design of a New Unmanned Aerial Vehicle Cyclocopter," *Journal of American Helicopter Society*, Vol. 52, (1), January 2007, pp. 24–35.

[42] Hwang, I. S., Min, S. Y., Lee, C. H., and Kim, S. J., "Development of a Four-Rotor Cyclocopter," *Journal of Aircraft,* Vol. 45, (6), December 2008, pp. 2151–2157.

[43] Min., S. Y., Lee. C. H., Sung, M. H., Kim, Y. S., Hur, C. M., and Kim, S. J., "Experimental Study of a Quadrotor Cyclocopter," Proceedings of the 69^{th} American Helicopter Society Annual Forum, Phoenix, AZ, May 21–23, 2013.

[44] Sirohi, J., Parsons, E., and Chopra, I., "Hover Performance of a Cycloidal Rotor for a Micro Air Vehicle," *Journal of American Helicopter Society,* Vol. 52, (3), July 2007, pp. 263-279.

[45] Parsons, E., "Investigation and Characterization of a Cycloidal Rotor for Application to a Micro-Air Vehicle," M.S. Thesis, University of Maryland, College Park, MD, 2005.

[46] Siegel, S., Seidel, J., Cohen, K., and McLaughlin, T., "A Cycloidal Propeller Using Dynamic Lift," Paper AIAA-2007-4232, AIAA 37th Fluid Dynamics Conference and Exhibit, Miami, FL, June 25–28, 2007.

[47] Nakaie, Y., Ohta, Y., and Hishida, K., "Flow Measurements Around a Cycloidal Propeller," *Journal of Flow Visualization*, Vol. 16, No. 4, pp. 393–402 July 6, 2010.

[48] Benedict, M., "Fundamental Understanding of the Cycloidal-Rotor Concept for Micro Air Vehicle Applications," Ph.D. Thesis, University of Maryland, College Park, MD December 2010.

[49] Benedict M., Ramasamy, M., and Chopra, I., "Improving the Aerodynamic Performance of Micro-Air-Vehicle-Scale Cycloidal Rotor: An Experimental Approach," *Journal of Aircraft*, Vol. 47, No. 4, July–August 2010, pp. 1117–1125.

[50] Benedict, M., Jarugumilli, T., and Chopra, I., "Experimental Performance Optimization of a MAV-Scale Cycloidal Rotor," *Journal of American Helicopter Society,* Vol. 56, No. 2, April 2011, pp. 022005-1–022005-11.

[51] Yang, K., Lakshminarayan, V. K., and Baeder, J. D., "Simulation of a Cycloidal Rotor System Using an Overset RANS Solver," Proceedings of the 66^{th} American Helicopter Society Annual Forum, Phoenix, AZ, May 11-13, 2010.

[52] Yang, K., "Aerodynamic Analysis of an MAV-Scale Cycloidal Rotor System Using a Structured OVERSET RANS Solver," Master of Science Thesis, University of Maryland, College Park, 2010.

[53] Hrishikeshavan, V., Benedict, M., and Chopra, I., "Flight Dynamics Identification of a Cyclocopter Micro Air Vehicle in Hover," Proceedings of the 69^{th} American Helicopter Society Annual Forum, Phoenix, AZ, May 21–23, 2013.

[54] Benedict, M., "Aeroelastic Design and Manufacture of an Efficient Ornithopter Wing," Master of Science Dissertation, Department of Aerospace Engineering, Indian Institute of Technology, Bombay, 2004.

[55] Sclater, N., *Mechanisms and Mechanical Devices: Sourcebook*, McGraw-Hill, New York, NY, December 2006.

[56] Lakshminarayan, V. K., "Computational Investigation of Micro-Scale Coaxial Rotor Aerodynamics in Hover," Ph.D. Thesis, Department of Aerospace Engineering, University of Maryland at College Park, 2009.

[57] Medida, S. and Baeder, J. D., "Application of the Correlation-based $\gamma - \overline{Re_{\theta t}}$ Transition Model to the Spalart-Allmaras Turbulence Model," American Helicopter Society 67th Annual Forum, May 2011, Virginia Beach, VA.

[58] Jarugumilli, T., Lind, A., Benedict, M., Lakshminarayan, V, Jones, A., and Chopra, I., "Experimental and Computational Flow Field Studies of a MAV-scale Cycloidal rotor in Forward Flight," Presented at the 69th Annual Forum of the American Helicopter Society, Phoenix, AZ May 21–23, 2013.

[59] Migliore, P.G., Wolfe, W.P., and Fanuccif, J.B.,"Flow Curvature Effects on Darrieus Turbine Blade Aerodynamics," *Journal of Energy*, Vol. 4, (2), 1980, pp. 49–55.

[60] White, F. M., Viscous Fluid Flow. 3rd ed. McGraw-Hill International Edition, 2006.

[61] Benedict, M., Jarugumilli, T., Lakshminarayan, V., and Chopra, I., "Experimental and Computational Studies to Understand the Role of Flow Curvature Effects on the Aerodynamic Performance of a MAV-Scale Cycloidal Rotor in Forward Flight," Proceedings of the 53^{rd} AIAA Structures, Structural Dynamics and Materials Conference, Honolulu, Hawaii, April 23–26, 2012.